Prediction of the moments in advection-diffusion lattice Boltzmann method. II. Attenuation of the boundary layers via double-Λ bounce-back flux scheme

Irina Ginzburg*
Irstea, Antony Regional Centre, HBAN, 1 rue Pierre-Gilles de Gennes CS 10030, 92761 Antony cedex, France
(Received 9 September 2016; published 17 January 2017)

Impact of the unphysical tangential advective-diffusion constraint of the bounce-back (BB) reflection on the impermeable solid surface is examined for the first four moments of concentration. Despite the number of recent improvements for the Neumann condition in the lattice Boltzmann method–advection-diffusion equation, the BB rule remains the only known local mass-conserving no-flux condition suitable for staircase porous geometry. We examine the closure relation of the BB rule in straight channel and cylindrical capillary analytically, and show that it excites the Knudsen-type boundary layers in the nonequilibrium solution for full-weight equilibrium stencil. Although the d2Q5 and d3Q7 coordinate schemes are sufficient for the modeling of isotropic diffusion, the full-weight stencils are appealing for their advanced stability, isotropy, anisotropy and anti-numerical-diffusion ability. The boundary layers are not covered by the Chapman-Enskog expansion around the expected equilibrium, but they accommodate the Chapman-Enskog expansion in the bulk with the closure relation of the bounce-back rule. We show that the induced boundary layers introduce first-order errors in two primary transport properties, namely, mean velocity (first moment) and molecular diffusion coefficient (second moment). As a side effect, the Taylor-dispersion coefficient (second moment), skewness (third moment), and kurtosis (fourth moment) deviate from their physical values and predictions of the fourth-order Chapman-Enskog analysis, even though the kurtosis error in pure diffusion does not depend on grid resolution. In two- and three-dimensional grid-aligned channels and open-tubular conduits, the errors of velocity and diffusion are proportional to the diagonal weight values of the corresponding equilibrium terms. The d2Q5 and d3Q7 schemes do not suffer from this deficiency in grid-aligned geometries but they cannot avoid it if the boundaries are not parallel to the coordinate lines. In order to vanish or attenuate the disparity of the modeled transport coefficients with the equilibrium weights without any modification of the BB rule, we propose to use the two-relaxation-times collision operator with free-tunable product of two eigenfunctions Λ. Two different values Λ_v and Λ_b are assigned for bulk and boundary nodes, respectively. The rationale behind this is that Λ_v is adjustable for stability, accuracy, or other purposes, while the corresponding $\Lambda_b(\Lambda_v)$ controls the primary accommodation effects. Two distinguished but similar functional relations $\Lambda_b(\Lambda_v)$ are constructed analytically: they preserve advection velocity in parabolic profile, exactly in the two-dimensional channel and very accurately in a three-dimensional cylindrical capillary. For any velocity-weight stencil, the (local) double-Λ BB scheme produces quasi-identical solutions with the (nonlocal) specular-forward reflection for first four moments in a channel. In a capillary, this strategy allows for the accurate modeling of the Taylor-dispersion and non-Gaussian effects. As illustrative example, it is shown that in the flow around a circular obstacle, the double-Λ scheme may also vanish the dependency of mean velocity on the velocity weight; the required value for $\Lambda_b(\Lambda_v)$ can be identified in a few bisection iterations in given geometry. A positive solution for $\Lambda_b(\Lambda_v)$ may not exist in pure diffusion, but a sufficiently small value of Λ_b significantly reduces the disparity in diffusion coefficient with the mass weight in ducts and in the presence of rectangular obstacles. Although Λ_b also controls the effective position of straight or curved boundaries, the double-Λ scheme deals with the lower-order effects. Its idea and construction may help understanding and amelioration of the anomalous, zero- and first-order behavior of the macroscopic solution in the presence of the bulk and boundary or interface discontinuities, commonly found in multiphase flow and heterogeneous transport.

DOI: 10.1103/PhysRevE.95.013305

I. INTRODUCTION

Among the broad scope of the advection-diffusion equation (ADE) problems modeled by the lattice Boltzmann method (LBM-ADE) the mesoscale solute transport through heterogeneous porous media is one of the most motivating [1–12] because of the complex boundaries and implicit interface shape. As an alternative to the finite difference, boundary-element and finite-element methods [13], the pioneering work [14] computes the effective diffusivity through a media composed of the overlapping randomly distributed grid-aligned rectangular obstacles, combining the d2Q5 discrete-velocity set with the discontinuous single-relaxation rate for heterogeneity, and bounce-back reflection for impermeable boundary. While originally the hydrodynamic velocity sets were adopted for isotropic soil [15–17], their coordinate subclasses, or the minimal d2Q5 and d3Q7 models [1,14,18], gain popularity for their efficiency, e.g., [3,7,8,10,12,19]. Already early work [1] reports an agreement within 0.2% between the three-dimensional 6 and 19 discrete-velocity sets for tracer dispersion in a nontrivial geometry. Recall that there exists an infinite number of suitable mass- and velocity-weight stencils, ranging from the minimal models to their rotated (diagonal) counterparts [20–22]. These two weight families independently determine the underlying discretization for diffusion and advection terms, respectively. In this work, we analytically and numerically examine their role on the first four moments of the averaged solute

*irina.ginzburg@irstea.fr

distributions. The moments of our interest are first moment characterizing the effective velocity ($\mathcal{U}$), second moment related to effective diffusivity of the porous structure [13,14,23] and Taylor dispersion [24–26], third and fourth moments quantified by their normalized values skewness and kurtosis, respectively. The results of the LBM schemes for their description are promising. The work [7] matches the experimental, highly "asymmetric" probability distributions for molecular displacement in rock cores with increasing degree of heterogeneity by the d3Q7 multiple-relaxation-time (MRT-ADE) isotropic-diffusion scheme [27,28]. The two-relaxation-times (TRT-ADE) d2Q5 scheme [29] agrees well with the reference solutions for resident-time and average-concentration distributions in bimodal stratified systems in heterogeneous porosity.

However, the numerical moments, rather than solute distributions, were found [29,30] much more sensitive to truncation and interface accuracy of the numerical scheme. It has been understood [31] that the truncation corrections in ADE schemes impact the measured Taylor-dispersion coefficient even in straight Poiseuille flow. Our conjoined investigation [30] extends the *extended method of moments* (EMM) approach [29] to prediction of the truncation contributions to the first four moments. The methodology [30] is worked out with the fourth-order-accurate mass-conservation equation of the TRT-ADE scheme [20,31] and illustrated for plug and Poiseuille profiles in straight channel and for Poiseuille profiles in cylindrical capillary. In a fully developed Taylor regime, the physical values [29,30] of the nondimensional dispersion (k_T), skewness ($\mathrm{Sk}_\star$), and kurtosis ($\mathrm{Ku}_\star$) coefficients are all set by Péclet number (Pe). However, the results [30] reveal their dependency on the numerical parameters: (i) the equilibrium group, composed of the diffusion-coefficient scale factor (hereafter c_e) and weights, and (ii) two positive relaxation eigenfunctions $\Lambda^{\pm}$. The two groups are linked by molecular diffusion coefficient $D_0 = c_e\Lambda^-$, while the weight dispatching and Λ^+ are freely adjustable. It is shown [30,31] that the relative truncation corrections to dispersion, skewness, and kurtosis have second-order accuracy. As Pe increases, they become controlled by the weights and the relaxation product $\Lambda = \Lambda^-\Lambda^+$.

This latter feature is predicated by the Λ property, that is, $\Lambda^{\pm}$ enter the nondimensional spatial truncation correction only via their Λ product, either in hydrodynamic or transport TRT schemes with constant source terms [32–34]. This allows for the consistent measurement of the effective (geometrical) characteristics of the structure such as permeability [34–38], heat conductivity [39], or relative diffusivity [19]. Furthermore, the Λ property allows to reach the equivalent accuracy [22,27] and stability [21] for any value of the diffusion coefficient, accelerate the convergence to steady state [19,34–37], and it becomes crucial for boundary and interface accuracy with the discontinuous or spatially variable transport coefficients, e.g., high viscosity ratio multiphase flows [40–42], non-Newtonian fluids [43], unsaturated flow [4,44], heterogeneous and anisotropic soil [22,41,45], or thermal coefficients [39]. A very recent single-relaxation-time Bhathager-Gross-Krook (BGK) approach [12] mimics the soil porosity with the spatially variable partial bounce-back mechanism, and thus formally allows for a uniform diffusion collision rate. However, this scheme requires a relaxation-rate dependent equilibrium velocity. Its numerical diffusion and consistency have not been examined yet. The subtle point is that, even if a modified propagation algorithm is coupled with the TRT or MRT operators, the Λ property is not guaranteed [46].

In a bulk the "optimal" Λ value is dictated by the truncation accuracy [20,30,31] and stability [21,47], that is, $\Lambda \in [\frac{1}{12}, \frac{1}{4}]$. However, the boundary [48,49] and interface conditions [41] further complicate the choice of Λ. It becomes evident by the optimal (most accurate) choice of Λ for regular and random arrays of spheres [34] or high-ratio thermal conductivity benchmark problem with the rotated interface [39]. The TRT solution obtained in [39] depends on Λ much stronger than it depends on the d2Q4-d2Q9 stencil. It is appropriate to mention that (i) the d2Q4 and d3Q6 isotropic MRT-ADE schemes automatically reduce to TRT, (ii) the full and minimal MRT-ADE schemes [27,28,50] are mostly used in two-rate configuration for isotropic diffusion, e.g., [51,52], and (iii) the MRT needs to fix all even-odd two-rates Λ combinations with specific rules [34] for consistent control [32] of the nondimensional solutions by governing physical numbers.

Note that the Λ property holds in computations only if all involved boundary rules maintain it. This is the case of the (i) bounce-back (BB) rule, either for Dirichlet flow velocity or Neumann advection-diffusion flux, and (ii) the anti-bounce-back Dirichlet (ABB) rule, either for concentration [48,51] or pressure [49,53,54]. Recall, the outgoing population returns in the opposite direction with the BB, but it changes its sign with the ABB. The parametrization of their steady solutions by Λ is independent of the geometry, dimension, boundary values, and discrete-velocity set; rather, it is stipulated by the specific organization of the symmetric and antisymmetric components in the closure relations of these two reflection rules [32,49]. As has been demonstrated [32,34,35,49], the Λ property is not automatic and it is not preserved with the recently recommended [55] linear and parabolic Bouzidi-Firdaouss-Lallemand (BFL) rules [56]. However, the linear BFL rules may be improved for the Λ property with the help of a local post-collision correction or the alternative but adequate interpolation coefficients [32,34,49]. At the same time, Λ controls the effective location of the boundary with the BB, ABB, and the properly parametrized high-order schemes [48,57]. For the sake of completeness (in the "Background" section) we update the "third-order" accurate ABB Λ solution [41,48]: it locates the parabolic, homogeneous, or heterogeneous diffusion profile halfway in the grid in any discrete-velocity set and, for a particular choice of scale factor c_e, it comprises recent solutions [51]. Specifically, the d2Q4 MRT scheme [19,51], where the mean value of two relevant relaxation rates is 1, is indeed the TRT scheme with $\Lambda = \frac{1}{4}$: this fact explains the diffusion-coefficient-independent relative diffusivity [19] computed with the ABB and BB rules, opposed to their BGK results. In the aforementioned (parabolic) configuration, the ABB rule serves as an example of the "favorable" matching of the boundary to the bulk, valid for any equilibrium stencil. This situation is principally distinct from the Neumann bounce-back zero-flux condition.

On the one hand, one of our motivations for this work on the bounce-back zero-flux rule is to support the truncation moment analysis [30] in full weight space. On the other hand, keeping in mind highly heterogeneous transport in reconstructed porous images, we are interested in the staircase wall description. This

also explains our brief recursion to the ABB rule: while in some recent works the prescribed Dirichlet [58], Neumann [59], or Robin [60,61] conditions are used to interpolate the solution to an (artificial) staircase midgrid boundary, the ABB rule enforces the interpolated values. However, neither the ABB rule nor the high-order Dirichlet schemes [48,49,62] guarantee mass conservation. While mass conservation is not necessary for steady solutions [35], it is not so for an accurate transient modeling of distribution and moments. Although one can always compensate the deficit of mass through a correction to the incoming populations, it is shown [63] that the procedure degrades the tangential accuracy with the interesting, mirror-type curved boundary Neumann approach [63]. In turn, when the reference tangential flux is zero, the BB performs as well as the improved d3Q7 and d3Q19 mass-conserving Neumann schemes [63], and much better than the nonconserving schemes for time-dependent symmetric diffusion solution inside a sphere. In the future, it will be important to extend the benchmarking of different Neumann approaches on the moments of the modeled distributions. In this work, we start with the bounce-back rule for its locality, mass conservation in any geometry, and Λ property.

It was early recognized [64] that "the bounce-back rule diminishes the diffusive transport and consequently enlarges the longitudinal hydrodynamic dispersion." This statement [64] addresses the Taylor dispersion in a channel modeled with the d3Q19 scheme. It has been demonstrated [48] that the bounce back nonphysically constrains the tangential advective-diffusive flux on the flat wall, via the diagonal links. This is to be contrasted [48] with the specular-forward reflection [64,65]: it correctly mimics the free slip in flow and no flux in ADE but naturally applies only on the straight walls. In turn, according to [66], "hardly any thermal Neumann boundary condition in literature takes the tangential aspects of the flux into account"; in our opinion, this is only partially true: several approaches [22,48,62,67] try to preserve the tangential flux explicitly. For that purpose, the BB was complemented [48] with a *local* correction derived from the population solution: it removes the leading-order tangential constraint from the BB closure relation; this scheme was further validated [22] with the d3Q15 velocity set in cuboid box in the presence of highly anisotropic and heterogeneous mass-weight stencil. The scheme [22,48] is expected to keep mass conservation in grid-aligned ducts, but its accuracy may degrade on staircase obstacle where the effective normal and tangential directions are unknown. The mixed Dirichlet-Neumann nonlocal scheme [62] risks to encounter similar difficulties because it carefully reconstructs the tangential flux on the smooth surface. Besides, the interpolation schemes [62,68] have been only worked out with the d2Q5 scheme, where they reduce to the ABB and BB rules for the midgrid location of straight wall.

Only very recently the two aforementioned bounce-back deficiencies [64], also shared by *local* specular reflection [69], were shown [69] to act independently and their primary effects were predicted exactly in straight channel for the d2Q9 scheme. They are (i) decrease of the diffusion coefficient, and (ii) delay of the average advection velocity. In a straight channel, these two effects are proportional to diagonal mass and velocity weight, respectively, and they decay only linearly with the space resolution [69]. As the secondary effect, the boundary-layer transverse velocity gradient induces the Taylor-type longitudinal dispersion; its relative correction to the physical Taylor coefficient is almost Pe independent for $\mathrm{Pe} \gg 1$. The quantification of these spurious effects becomes possible [69] due to the construction of the nonequilibrium correction in the linkwise recurrence form [32], referred to as the "boundary-layer" component. It accommodates the mismatch between the bulk solution and the closure relation of the boundary rule.

It should be underlined that in the rarefied gas dynamics the boundary layers are a physical reality [70], while in our study they are unwanted numerical artifacts anticipated in early work [71]. The construction of the nonequilibrium boundary layers is based on the exact recurrence equations (RE) of the TRT scheme [32]. We point out that, unlike other approaches, namely, Chapman-Enskog expansion [27,72–74], Fourier series [75], Taylor-truncation expansion [76,77], equivalent partial differential equations [78], asymptotic analysis [28], or lattice kinetic approach [42,79], the nonequilibrium component in the RE is exact. It is given without any approximation in a compact form, as a linear combination of the central, spatial, and temporal finite differences applied to equilibrium and nonequilibrium components. If the (smooth) nonequilibrium solution can be represented as a series with respect to the equilibrium, the Taylor series of RE matches the Chapman-Enskog expansion [20,33]. Yet, the RE also exactly captures any nonequilibrium perturbation. It should be underlined that, since the developed Taylor-dispersion regime [24] is static in moving frame, the steady-state nonequilibrium framework [32] is sufficient, as confirmed by the exactness of the derived solutions [69] in a straight channel. Previously, the nonequilibrium layers were specified [53] in order to explain the no-slip exact accommodation of the predicted parabolic profile with the Navier-Stokes equilibrium in straight Poiseuille flow. The distinctive feature of the present tangential bounce-back deficiency is that it modifies all transport coefficients in comparison to their bulk predictions.

In this work, we first extend construction [69] of the nonequilibrium boundary layers to a cylindrical capillary. Since the variance of the numerical distribution consists of physical, truncation, boundary-layer diffusion and dispersion, this analysis enables us to single out the truncation error and obtain a numerical confirmation for its estimate [30]. In addition, we will reveal the effect of boundary layers on skewness and kurtosis. Our analysis is operated with the d3Q15 velocity set in the presence of all adjustable parameters and weights. The d3Q7 TRT scheme with $\Lambda = \frac{1}{4}$ was successfully employed for Taylor dispersion in shear thinning capillary flow [80], and it might be argued that the coordinate stencil presents the best choice for the isotropic diffusion with the BB rule because it is aligned with the staircase walls. However, it can be easily imagined that the rotated stencil holds the same property for diagonally oriented walls. Moreover, in a capillary the hydrodynamic mass weight is required for the isotropy of the fourth-order diffusion term and rigorous validity of the truncation estimate [30]. Although the higher-order isotropy might be regarded as a luxurious requirement for transport in porous media, the two weight families are responsible for stability in d2Q9, d3Q13, d3Q15, and d3Q19 schemes [20,21,47]: the identical specific full stencil for

mass and velocity terms vanishes very restrictive stability constraints of the minimal schemes and enhances efficiency at high Pe range. In fact, this advanced stability is due to the diagonal links enforcing the anti-numerical-diffusion tensor [21,45]; the diagonal links are also required for the same purpose with the alternative MRT approach [81].

In order to liberate the bounce-back results from the primary weight dependency, we propose the double-Λ bounce-back TRT scheme. It does not require any modification, either for bounce back or TRT. The double-Λ scheme operates with the two distinguished Λ values: Λ_b in grid boundary nodes and Λ_v in bulk nodes. The rationale behind this idea is that the presence of two very different Λ values may change the sign of the effect [69]. The construction of double Λ in straight channel and cylindrical capillary will be performed with the help of the generic steady-state interface conditions [41,82]. They close the system and prove their validity in the presence of the boundary layers in nonequilibrium component. On the constructed solution of the scheme, we look for the dependency $\Lambda_b\,(\Lambda_v)$ for any given Λ_v such that the bounce-back tangential effect vanishes for first moment. Therefore, in straight channel and cylindrical capillary, the derived solutions $\Lambda_b(\Lambda_v)$ preserve mean velocity in parabolic profile. In a channel, it makes the BB solutions quasi-identical to the specular reflection for dispersion, skewness, and kurtosis. In a capillary, the double-Λ scheme reduces the boundary-layer dispersion and enables validation of the truncation predictions [30] in the presence of diagonal-velocity weight. The $\Lambda_b(\Lambda_v)$ solutions are very similar in two geometries but distinct and resolution dependent. A simple procedure is proposed to locate the root $\Lambda_b(\Lambda_v)$ within few bisection iterations in any given geometry; it will be illustrated for two-dimensional flow around a circular cylinder where the effective mean velocity then remains the same for any velocity weight. The double-Λ scheme may not have a positive $\Lambda_b(\Lambda_v)$ root in pure diffusion. The possibility to reduce the mass-weight disparity in the effective diffusivity [19,83] using a small but positive Λ_b will be examined in simple porous configurations.

The rest of the paper is organized as follows. Section II provides (i) the TRT-ADE scheme, (ii) the closure relations of the anti-bounce-back and bounce-back rules together with their illustrative solutions, and (iii) the recurrence form of the nonequilibrium boundary layers. Section III predicts the bounce-back boundary-layer effects in straight channel and cylindrical capillary. In pure diffusion, they are worked out for (i) diffusion coefficient and (ii) kurtosis; in plug and Poiseuille flow, these effects are specified for (i) apparent velocity and (ii) longitudinal dispersion. Section IV is devoted to the symbolic construction of the double-Λ distributions in straight channel and cylindrical capillary. Section V examines their efficiency in reduction of the velocity-weight dependency in dispersion, skewness, and kurtosis. Section VI examines the double-Λ approach for effective diffusivity in periodic porous arrangements and develops an iterative procedure in advective flow around obstacle. Section VII concludes the work. The technical details for boundary-layer analysis are provided in the Appendix.

II. BACKGROUND

In Sec. II A, we recall the TRT-ADE d2Q9 and d3Q15 schemes along with their advanced free parameter combinations and discuss the exact, second-order-accurate, and averaged advection-diffusion equations, the truncation and numerical computation of the first four moments of the averaged solute distributions. The exact closure relations of the anti-bounce-back (Sec. II B 1) and bounce-back (Sec. II B 2) rules are discussed with respect to the Dirichlet (Sec. II B 1) and zero-flux Neumann (Sec. II B 2) boundary conditions. They are illustrated by solutions in a straight channel for pure diffusion with a constant mass source (Sec. II B 1) and advection diffusion (Sec. II B 2). This analysis questions the suitable definition of the macroscopic variables (Sec. II B 1) and the tangential-constraint dependency on the equilibrium weight (Sec. II B 2). Because of the incompatibility of the bulk solution with the bounce-back rule in full weight space, the concept and exact form of the accommodation nonequilibrium numerical layers is recalled (Sec. II C).

A. TRT-ADE scheme

The two-relaxation-times (TRT) model [20,27,41] assumes the d-dimensional velocity set consisting of zero-amplitude vector $\boldsymbol{c}_0$ and $Q_m = Q-1$ vectors $\boldsymbol{c}_q$ connecting cuboid-grid nodes $\boldsymbol{r}$; each vector $\boldsymbol{c}_q$ has the opposite one: $\boldsymbol{c}_{\bar{q}} = -\boldsymbol{c}_q$, $q = 1,\dots,Q_m/2$. Accordingly, the two populations per link $f_q(\boldsymbol{r},t)$ and $f_{\bar{q}}(\boldsymbol{r},t)$ are decomposed into their symmetric and antisymmetric components: $f_q^{\pm} = (f_q \pm f_{\bar{q}})/2$. The TRT scheme updates them with the help of the two relaxation rates $s^{\pm} \in]0,2[$:

$$\begin{aligned} f_q(\boldsymbol{r}+\boldsymbol{c}_q,t+1) &= f_q(\boldsymbol{r},t) + g_q^+ + g_q^-,\ g_q^{\pm} = -s^{\pm}(f_q^{\pm} - e_q^{\pm}),\ q = 0,\dots,\frac{Q_m}{2},\\ f_{\bar{q}}(\boldsymbol{r}-\boldsymbol{c}_q,t+1) &= f_{\bar{q}}(\boldsymbol{r},t) + g_q^+ - g_q^-,\ q = 1,\dots,\frac{Q_m}{2}. \end{aligned} \tag{1}$$

In this study, the common-form distribution $\{e_q^{\pm}(\boldsymbol{r},t),\ q = 0,\dots,Q_m/2\}$, suitable for d2Q9 in 2D and d3Q15 in 3D, is computed with the local mass value $C(\boldsymbol{r},t) = \sum_{q=0}^{Q_m} f_q$ and prescribed local velocity $\boldsymbol{U}(\boldsymbol{r},t)$:

$$e_q^+(\boldsymbol{r},t) = C\left[t_c^{(m)}c_e + t_c^{(u)}\bar{U}^2 + \frac{1}{2}\left(U_\alpha^2 - \bar{U}^2\right)\right],\ e_q^- = t_c^{(a)}CU_\alpha c_{q\alpha},\ \text{if } c_{q\alpha}\neq 0,\ c_{q\alpha}c_{q\beta}|_{\alpha\neq\beta} = 0 \tag{2a}$$

$$e_q^+(\boldsymbol{r},t) = C\left(t_d^{(m)}c_e + t_d^{(u)}\bar{U}^2 + \frac{1}{N_d}\sum_{\alpha\neq\beta}U_\alpha U_\beta c_{q\alpha}c_{q\beta}\right),\ e_q^- = t_d^{(a)}C\boldsymbol{U}\cdot\boldsymbol{c}_q,\ \text{if } c_{q\alpha}c_{q\beta}|_{\alpha\neq\beta}\neq 0 \tag{2b}$$

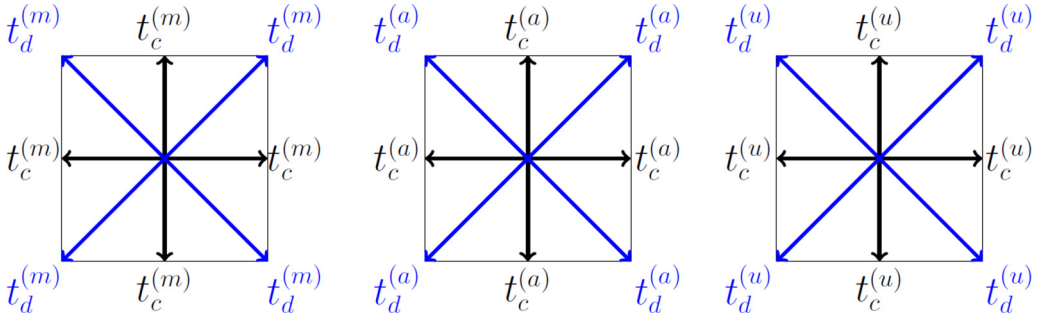

FIG. 1. This figure illustrates the coordinate and the diagonal equilibrium stencils of the d2Q9 scheme for, from the left to the right, the mass weight, the velocity weight, and the anti-diffusion weight in Eq. (2). The three families of weights are independent, but all of them satisfy the isotropic constraint $\sum_{q=1}^{Q_m} t_q^{(\cdot)} c_{q\alpha} c_{q\beta} = \delta_{\alpha\beta}$. The d3Q15 is composed from 6 coordinate discrete velocities $||\boldsymbol{c}_q||^2 = 1$ with the weight $t_c^{(\cdot)}$, and 8 diagonal velocities $||\boldsymbol{c}_q||^2 = 3$ with the weight $t_d^{(\cdot)}$. The d2Q5 and d3Q7 yield $t_c^{(\cdot)} = \frac{1}{2}$, $t_d^{(\cdot)} = 0$. The hydrodynamic choice is $t_c^{(m)} = t_c^{(a)} = \frac{1}{3}$, $t_d^{(m)} = t_d^{(a)} = \frac{1}{12}$ (d2Q9), and $t_d^{(m)} = t_d^{(a)} = \frac{1}{24}$ (d3Q15).

$$e_0^+(\boldsymbol{r},t) = C(\boldsymbol{r},t) - 2\sum_{q=1}^{\frac{Q_m}{2}} e_q^+(\boldsymbol{r},t),\ e_0^-(\boldsymbol{r},t) = 0,\ \text{with } \bar{U^2} = \frac{U^2}{d},\ U^2 = \sum_{\alpha=1}^{d} U_\alpha^2, \tag{2c}$$

$$t_d^{(m)} = \frac{1-2t_c^{(m)}}{N_d},\ t_d^{(a)} = \frac{1-2t_c^{(a)}}{N_d},\ t_d^{(u)} = \frac{1-2t_c^{(u)}}{N_d},\ t_c^{(\cdot)} \in \left[0,\frac{1}{2}\right],\ N_d = \sum_{q=1}^{Q_m} c_{q\alpha}^2 c_{q\beta}^2\ ,\ \alpha \neq \beta. \tag{2d}$$

This equilibrium form is extended for heterogeneous porous soil [29] and, including the d3Q13 and d3Q19 schemes, for anisotropic diffusion [20,21,45]. In these relations, Eq. (2a) applies on the subset of $2d$ "coordinate" discrete velocities, while Eq. (2b) addresses the N_d "diagonal" discrete velocities, with $N_d = 4$ in d2Q9 and $N_d = 8$ in d3Q15. The three independent, non-negative, isotropic weight families $t_q^{(\cdot)} = \{t_q^{(m)}, t_q^{(a)}, t_q^{(u)}\}$ obey the same constraint: $\sum_{q=1}^{Q_m} t_q^{(\cdot)} c_{q\alpha} c_{q\beta} = \delta_{\alpha\beta}$. They are illustrated in Fig. 1. The d2Q5 and d3Q7 coordinate (minimal) schemes lack the diagonal velocities, Eq. (2b) vanishes in them, and Eq. (2a) reads as $t_c^{(\cdot)} = \frac{1}{2}$, then $e_q^+ = \frac{1}{2}C(c_e + U_\alpha^2)$, $e_q^- = \frac{1}{2}CU_\alpha c_{q\alpha}$ for $c_{q\alpha} \neq 0$, $q = 1, \ldots, Q_m/2 = d$. The two-dimensional model composed of the diagonal links will be referred to as the "rotated" d2Q5 scheme [21,69]. The positive parameter c_e is free tunable: its stability range depends on the mass weight [20,21,47], with $c_e \in]0, \frac{1}{d}]$ in minimal schemes. In stability limit $c_e = \frac{1}{d}$, $t_q^{(u)} = 0$, the d2Q5 and d3Q7 reduce, respectively, to d2Q4 and d3Q6 diffusion schemes. Thus, Eq. (2) offers the three principal degrees of freedom: c_e, mass weight $\{t_c^{(m)}, t_d^{(m)}\}$, and velocity weight $\{t_c^{(a)}, t_d^{(a)}\}$. These three elements are often fixed to their hydrodynamic choice, with $c_e = c_s^2 = \frac{1}{3}$. The "hydrodynamic" weight, $t_c^{(\cdot)} = \frac{1}{3}$ in d2Q9 and d3Q15, satisfies the second constraint: $S_d(t_q^{(\cdot)}) = \sum_{q=1}^{Q_m} t_q^{(\cdot)} c_{q\alpha}^2 c_{q\beta}^2 = t_d^{(\cdot)} N_d = \frac{1}{3}$ when $\alpha \neq \beta$. The "hydrodynamic" mass weight improves the isotropy of the fourth-order linear pure-diffusion form [20,30]. The hydrodynamic velocity weight provides the isotropy of the third-order linear advection correction in d2Q9 scheme, at least [20]. The stable maximum velocity amplitude $|U|^{\max}(c_e, t_q^{(a)})$ is predicated by c_e and velocity weight, the most stable value is $t_c^{(a)} = \frac{1}{4}$ in d2Q9 and d3Q15 schemes: their necessary stability constraints in d-dimensional velocity field are derived [20,21] and resumed [30,45,47]. The stable velocity amplitude is conditioned [20,21] by the (negative) quantity of the second-order numerical diffusion. The anti-numerical-diffusion correction in Eq. (2) is controlled by the weight family $\{t_q^{(u)}\}$; this term completely removes the second-order numerical diffusion in plug [21,27,45] and streamwise-invariant [30,31] flow, at least. Within the second-order-accurate approximate, the solute concentration C then obeys advection-diffusion equation with the advective velocity $\boldsymbol{U}(\boldsymbol{r},t)$ and molecular diffusion coefficient D_0 (in lattice units):

$$\partial_t C + \boldsymbol{\nabla}\cdot(\boldsymbol{U}C) = \boldsymbol{\nabla}\cdot(D_0\boldsymbol{\nabla}C),\ D_0 = c_e\Lambda^-. \tag{3}$$

The two eigenfunctions $\Lambda^\pm = \frac{1}{s^\pm} - \frac{1}{2}$ are positive: while $\Lambda^- = D_0/c_e$ is fixed by c_e and D_0, Λ^+ is free. A special role in numerical assessment of the scheme is played by free-tunable product of two eigenfunctions: $\Lambda = \Lambda^-\Lambda^+$. When Λ is prescribed, the two relaxation parameters $s^\pm$ are interconnected:

$$s^+ = \frac{2(2-s^-)}{2-s^-+4s^-\Lambda} \text{ with } \Lambda = \Lambda^-\Lambda^+ = \left(\frac{1}{s^+}-\frac{1}{2}\right)\left(\frac{1}{s^-}-\frac{1}{2}\right). \tag{4}$$

It has been proved [32] that fixed value of Λ controls any nondimensional steady-state solution of the exact mass-conservation equation (with constant mass-source, at least) on top of the Péclet number $\mathrm{Pe} = \mathcal{U}\mathcal{L}/D_0$ (giving characteristic length $\mathcal{L}$ and velocity $\mathcal{U}$). Two particular values, such as $\Lambda = \frac{1}{12}$ and $\frac{1}{6}$, vanish the coefficients of the third- and fourth-order-accurate, respectively, spatial truncation corrections [20,30,31]. In combination with the particular choice $\Lambda^- = \sqrt{\frac{1}{12}}$, these two distinguished Λ values, respectively, vanish either advective or pure-diffusion transient truncation corrections to Eq. (3). The

most stable choice [21] is $\Lambda = \frac{1}{4}$, where the arithmetical-mean value of two eigenvalues (4) is equal to one:

$$\Lambda = \frac{1}{4} \; : \; s^+ = 2 - s^- \text{ or } \frac{s^+ + s^-}{2} = 1. \tag{5}$$

This choice makes the necessary stability conditions [20,21,47] sufficient for any Λ^-, either with the minimal schemes or suitable mass and velocity weight stencils. Hence, $\Lambda = \frac{1}{4}$ allows to reach high Pe with the largest possible velocity amplitude. When $\Lambda <\approx \frac{1}{6}$, the stable velocity amplitude drastically depends [20,47] upon Λ^- and c_e when $c_e\Lambda^- \to 0$. These theoretical predictions, derived in constant (plug) flow, are numerically confirmed [31] for $|U|^{\max}(c_e)$ in Poiseuille profile (focused on the d2Q5 scheme).

The advanced stability of $\Lambda = \frac{1}{4}$ is due to the specific form of the exact mass-conservation equation $\sum_{q=0}^{Q_m} g_q^+ = 0$, which reads as, after substitution of the recurrence solution [32] for the nonequilibrium components $\{g_q^\pm\}$,

$$\left[\bar{\Delta}_t \sum_{q=0}^{Q_m} e_q^+ + \sum_{q=1}^{Q_m} \bar{\Delta}_q e_q^-\right](\boldsymbol{r},t) = \left[\Lambda^- \left(\sum_{q=1}^{Q_m} \bar{\Delta}_q^2 e_q^+ - \sum_{q=0}^{Q_m} \bar{\Delta}_t^2 e_q^+\right) - \left(\Lambda - \frac{1}{4}\right) \sum_{q=1}^{Q_m} \bar{\Delta}_q^2 g_q^+\right](\boldsymbol{r},t). \tag{6}$$

Mass-conservation equation is expressed in terms of the central-time and linkwise-central spatial finite-difference operators (see [20,30,31] for details). This form, suitable for any mass-conserving, either isotropic or anisotropic, equilibrium provides the fourth-order-accurate truncation corrections to Eq. (3), e.g., in constant velocity field [20], heterogeneous soil [29], and streamwise-invariant flows [30,31]. With the second-order-accurate space averaging of Eq. (3), mean concentration $\bar{C}(x,t) = \langle C(\boldsymbol{r},t)\rangle$ obeys the advection-dispersion equation with mean velocity $\mathcal{U} = \langle U_x(\boldsymbol{r})\rangle$ and dispersion coefficient D:

$$\partial_t \bar{C} + \partial_x \mathcal{U}\bar{C} = D\partial_x^2 \bar{C}. \tag{7}$$

We assume that the mean seepage velocity $\mathcal{U}$ is space and time independent; it is directed along the x axis where $\langle \ldots \rangle = S^{-1}\int_S ds$ denotes the average value over the void (porous) part in cross section $S(x)$. Let $\mu_n(t) = \int_{-\infty}^{\infty}(x - x_0)^n \bar{C}(x,t)dx$ denote the nth raw moment of $\bar{C}$ for $n \geqslant 0$, and $\mu_n^\star(t)$ be its nth central moment: $\mu_n^\star(t) = \int_{-\infty}^{\infty}(x - x_0 - \mathcal{U}t)^n \bar{C}(x,t)dx$, for $n \geqslant 2$. The apparent solutions for $\mathcal{U}$, D, skewness $\mathrm{Sk}(t)$, and kurtosis $\mathrm{Ku}(t)$ are set by the first four spatial moments [assuming $\mu_0(t) \equiv 1$]:

$$\mathcal{U} = \frac{\mu_1}{t}, \quad D = \frac{\mu_2^\star}{2t}, \quad \mathrm{Sk}(t) = \frac{\mu_3^\star(t)}{[\mu_2^\star(t)]^{3/2}}, \quad \mathrm{Ku}(t) = \frac{\mu_4^\star(t)}{[\mu_2^\star(t)]^2} - 3. \tag{8}$$

We consider evolution of the Dirac delta function $C(\boldsymbol{r},t = 0) = \delta(x - x_0)$ in the fully developed Taylor regime [24,25]

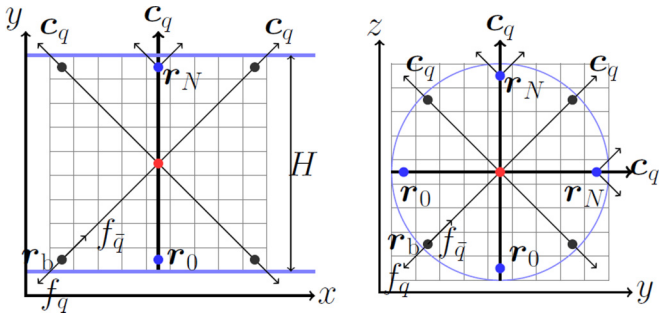

FIG. 2. This figure illustrates construction of the nonequilibrium boundary layers along the vertical axis in straight channel and along a coordinate axis in circular cross section. The grid nodes are those whose centers lie inside the bounded domain; the boundary nodes $\boldsymbol{r}_\mathrm{b} = \{\boldsymbol{r}_0, \boldsymbol{r}_N\}$ have two (d2Q9) and four (d3Q15) incoming diagonal populations with $c_{qx} = \pm 1$.

where the longitudinal dispersion, skewness, and kurtosis can be characterized by the dimensionless time-independent coefficients k_T, $\mathrm{Sk}_\star$, and $\mathrm{Ku}_\star$:

$$k_T = \frac{D}{D_0} - 1, \; \mathrm{Sk}_\star = \sqrt{\frac{\mathcal{U}t}{\mathcal{L}}}\mathrm{Sk}(t), \text{ and } \mathrm{Ku}_\star = \frac{\mathcal{U}t}{\mathcal{L}}\mathrm{Ku}(t). \tag{9}$$

The two well-known solutions for the dispersivity coefficient k_T in Poiseuille velocity profile are $k_T = \frac{\mathrm{Pe}^2}{210}$ (with $\mathrm{Pe} = \frac{\mathcal{U}H}{D_0}$ in straight channel of width H) and $k_T = \frac{\mathrm{Pe}^2}{192}$ (with $\mathrm{Pe} = \frac{2\mathcal{U}R}{D_0}$ in cylindrical capillary of radius R). Based on the Gaussian distribution as solution of Eq. (7) for initial Dirac plume distribution, $\mathrm{Sk}_\star$ and $\mathrm{Ku}_\star$ are both equal to zero in these two configurations. Yet, this second-order result neglects the third- and fourth-order corrections appearing in space averaging of Eq. (3). By accounting for them automatically with the EMM approach [29], the effective (physical) values of $\mathrm{Sk}_\star$ and $\mathrm{Ku}_\star$ can be found in [30] (they present the particular case of bimodal, stratified channel, and cylindrical capillary solutions [29]). Further, the truncation corrections of the TRT scheme in k_T, $\mathrm{Sk}_\star$, and $\mathrm{Ku}_\star$ are derived in these two configurations with the EMM approach [30] from Eq. (6). Unlike the physical coefficients k_T, $\mathrm{Sk}_\star$, and $\mathrm{Ku}_\star$, the truncation corrections are not set by Péclet number alone, but, in addition, they depend on c_e, Λ^-, Λ, and weights. Their dependency on velocity weight principally vanishes for $\Lambda = \frac{1}{12}$, while the mass-weight dependency in kurtosis vanishes for $\Lambda = \frac{1}{6}$ and asymptotically vanishes as Pe increases, $\forall\,\Lambda$. The relative truncation modification in all three transport coefficients decays with the second-order accuracy, as $\mathcal{L}^{-2}$.

B. Closure relations

At grid boundary node $\boldsymbol{r}_\mathrm{b}$, when $\boldsymbol{r}_\mathrm{b} + \boldsymbol{c}_q$ lies outside the computational domain, the system is closed by the boundary rule providing the incoming population $f_{\bar{q}}(\boldsymbol{r}_\mathrm{b}, t+1)$ with $\boldsymbol{c}_{\bar{q}} = -\boldsymbol{c}_q$ (see Fig. 2). Here, two situations can be distinguished. In the favorable situation, the boundary rule supports nonequilibrium solution $g_q^\pm = G_q^\pm$, where $G_q^\pm$ is given by

the second-order-accurate Chapman-Enskog expansion with respect to the equilibrium $e_q^{\pm}$: Eqs. (3) and (7) then keep their predicted form. We will illustrate this configuration for parabolic distributions modeled with the help of the anti-bounce-back (ABB) Dirichlet boundary rule [41,48]. In the unfavorable situation, the incoming population cannot match the nonequilibrium solution $G_q^{\pm}$: the system creates nonequilibrium accommodation corrections referred to as *boundary layers*. They are not described by the Chapman-Enskog expansion but they are covered by the recurrence (exact) nonequilibrium form [32]. This unfavorable situation happens with the bounce-back no-flux rule on straight walls in the presence of the diagonal weight [69].

1. Anti-bounce-back Dirichlet boundary rule

Let us complement (in this section only) the right-hand side in Eq. (3) with the external mass source quantity $\mathcal{S}(\boldsymbol{r},t)$ by adding, in Eq. (1), $S_q^+ = t_q^{(m)} c_e \mathcal{S}$ to g_q^+ and $\mathcal{S} - 2\sum_{q=1}^{Q_m} S_q^+$ to g_0^+. Assume the boundary value $\mathcal{C}_b$ for macroscopic concentration solution $\mathcal{C}(\boldsymbol{r}_b + \boldsymbol{c}_q)$ is enforced by the Dirichlet ABB rule. It reads as the TRT collision (1):

$$\text{ABB}: \ f_{\bar{q}}(\boldsymbol{r}_b,t+1) = -[f_q + g_q^+ + g_q^- + S_q^+](\boldsymbol{r}_b,t) + 2w_q,$$
$$w_q = e_q^+(\mathcal{C}_b). \tag{10}$$

Since, by definition in Eq. (1), $f_q = e_q^+ + e_q^- - \frac{g_q^+}{s^+} - \frac{g_q^-}{s^-}$ and $f_{\bar{q}} = e_q^+ - e_q^- - \frac{g_q^+}{s^+} + \frac{g_q^-}{s^-}$, the steady-state closure relation of the ABB rule (10) reads as for any (cut) link $\boldsymbol{c}_q$ intersecting the solid surface

$$\text{ABB}: \ e_q^+ + \tfrac{1}{2} g_q^- - \Lambda^+ g_q^+ + \tfrac{1}{2} S_q^+ = w_q. \tag{11}$$

Let us consider the pure-diffusion situation $e_q^+ = t_q^{(m)} c_e C$, $e_q^- \equiv 0$. The expected steady-state second-order-accurate bulk solution for $g_q^{\pm}$ is given by the Chapman-Enskog expansion $G_q^- = \partial_q e_q^+$ and $G_q^+ = -\partial_q \Lambda^- \partial_q e_q^+ - S_q^+$, with $\partial_q C = \nabla C \cdot \boldsymbol{c}_q$. After substitution of this solution into Eq. (11), the closure relation becomes

$$\text{ABB}: \ \left[\left(e_q^+ + \tfrac{1}{2} S_q^+\right) + \tfrac{1}{2}\partial_q e_q^+ + \partial_q \Lambda \partial_q e_q^+ + \Lambda^+ S_q^+\right](\boldsymbol{r}_b)$$
$$= e_q^+(\mathcal{C}_b). \tag{12}$$

When $S_q^+ = 0$, Eq. (12) fits the second-order-accurate linkwise-directional Taylor expansion from $\boldsymbol{r}_b$ to $\boldsymbol{r}_b + \frac{1}{2}\boldsymbol{c}_q$, provided that $\Lambda = \frac{1}{8}$. This solution has been originally presented by Eq. (43) in Ref. [27]; note that the notations [27] are different: $\Lambda^2 = 4/3\Lambda^+\Lambda^- = \frac{1}{6}$. That is, $\Lambda = \frac{1}{8}$ locates the prescribed boundary value midgrid for any e_q^+ in the absence of external mass source. The suitability of $\Lambda = \frac{1}{8}$ is extended [27] for time-dependent solution and nonzero (arbitrary) mass source with the help of the specific correction to w_q in Eq. (10): it directly removes the unsuitable terms from the ABB closure relation.

We note that by equating the set of closure relations of the given boundary scheme to the Taylor expansion, one avoids the tedious solving [51,84] of the entire population system or particular construction of the nonequilibrium solution [42], commonly restricted to the straight channel configuration. The approach of exact closure relations is quite general and it was employed in analysis and design of the high-order boundary and interface conditions in flow schemes [34,35,41,49] and ADE schemes [41,48], pressure Dirichlet schemes [49,53] recently adapted [54] for free-interface stress condition.

Let us consider now the particular case of the parabolic distribution $C(y)$ in a straight channel $y \in [-\frac{H}{2}, \frac{H}{2}]$ maintained by the constant mass source $\mathcal{S}$, then $-\mathcal{S} = c_e \Lambda^- \partial_y^2 C$, $S_q^+ = -t_q^{(m)} \Lambda^- c_e^2 \partial_y^2 C$, $\partial_q e_q^+ = t_q^{(m)} c_e \partial_y \mathcal{C} c_{qy}$, and $\partial_q \Lambda \partial_q e_q^+ = t_q^{(m)} c_e \Lambda \partial_y^2 C c_{qy}^2$. If the macroscopic solution $\mathcal{C}(y)$ is redefined with the half-mass quantity $\mathcal{C} = C + \frac{1}{2}\mathcal{S}$, the closure relation (12) becomes

$$\text{ABB}, \mathcal{S} = \text{const}: \ t_q^{(m)} c_e \left[\mathcal{C} + \tfrac{1}{2}\partial_y \mathcal{C} c_{qy} + \Lambda(1-c_e)\partial_y^2 \mathcal{C} c_{qy}^2\right]$$
$$(\boldsymbol{r}_b) = t_q^{(m)} c_e \mathcal{C}_b, \text{ if } c_{qy}^2 = 1. \tag{13}$$

This closure relation dictates the identical closure conditions for normal and diagonal cut links. It maintains the parabolic profile in straight channel of the width H_{eff} given by Eq. (14) for any Λ, and it assures the halfway location of two solid walls provided that Λ obeys Eq. (14):

$$\text{ABB}, \mathcal{S} = \text{const}: \ H_{\text{eff}}^2 = H^2 + 8(1-c_e)\Lambda - 1 \,\forall\, \Lambda,$$
$$H_{\text{eff}} = H \ \text{ if } \ \Lambda = \frac{1}{8(1-c_e)}, c_e \in]0, c_e^{(\max)}]. \tag{14}$$

Note that the derivation of Eq. (14) holds for any velocity set and that Eq. (14) also assures midgrid location of the flat interface in stratified parabolic configuration [41] with the bimodal (discontinuous) diffusion coefficients [see their Eq. (99) with $\Lambda_{eq} = \frac{1}{8(1-c_e)} + \frac{\Lambda^- c_e}{2(1-c_e)}$ in case when $\mathcal{C}$ is not redefined with $\mathcal{S}/2$]. The redefinition of the macroscopic variables with the half source quantity allows for the consistent parametrization of the steady-state solutions and the spatial truncation variation in transient solutions with the nondimensional numbers [32,49]. This property is supported by the ABB and BB boundary rules. It has been recognized [41] that when $\mathcal{C}$ is redefined with $\mathcal{S}/2$, the "optimal" Λ reduces to the bounce-back solution [35,57] for Poiseuille flow, which is $\Lambda = \frac{3}{16}$ in particular case $c_e = c_s^2 = \frac{1}{3}$ in Eq. (14). It can be shown by the symmetry argument $e_q^+ \to e_q^-$, $S_q^+ \to S_q^-$, $g_q^{\pm} \to g_q^{\mp}$ that the BB closure relation in force-driven Poiseuille flow and the ABB closure relation (11) are simply interchangeable. The Poiseuille flow solution $\Lambda = \frac{3}{16}$ is valid for any hydrodynamic discrete-velocity set [35], provided that the external force quantity is computed with the same (hydrodynamic) weight as for e_q^- in flow. Moreover, $\Lambda = \frac{3}{16}$ [or $s^- = \frac{8(s^+-2)}{s^+-8}$ in TRT and MRT flow schemes] is also suitable for straight two-phase Poiseuille flow with different viscosities [40,41] and halfway interface; in conventional flow schemes [40,41], it is equivalent to the recent solution [42].

Remark 1. Equation (14) comprises recent results [51] for parabolic concentration profile modeled with the d2Q4, d2Q5, and d2Q9 MRT schemes in combination with the ABB rule (called there "halfway bounce-back rule"). The d2Q4 and d2Q5 schemes [51] are particular cases of Eq. (2) with $t_c^{(m)} = t_c^{(a)} = \frac{1}{2}$, $c_e = \frac{1}{2}$, and $c_e = \frac{2}{5}$, respectively, while the d2Q9 scheme [51] fits Eq. (2) with $t_c^{(m)} = t_c^{(a)} = c_e = \frac{1}{3}$. In

the parabolic concentration profile, the only one relevant Λ product in schemes [51] is set by (diffusion) rate $s_D = s^-$ and (free) rate $s_2 = s^+$, then $\Lambda = (\frac{1}{s_D} - \frac{1}{2})(\frac{1}{s_2} - \frac{1}{2})$. Applying Eq. (14), $\Lambda = \{\frac{1}{4}, \frac{5}{24}, \frac{3}{16}\}$ in three configurations [51]. This corresponds, with the the help of Eqs. (4) and (5), to three individually derived solutions [51]: $s_2 = 2 - s_D$ (d2Q4), $s_2 = \frac{12(s_D-2)}{s_D-12}$ (d2Q5), and $s_2 = \frac{8(s_D-2)}{s_D-8}$ (d2Q9). The BGK model assures Eq. (14) with the specific value $\Lambda^- = \sqrt{\Lambda}$ but, in contrast with [51], the BGK is not restricted to one particular value D_0, rather to the interval $D_0 \in]0, c_e^{(\max)}\sqrt{\Lambda}]$ inside the velocity-set-dependent stability interval $c_e \in]0, c_e^{(\max)}]$.

Remark II. Identical weight distribution for Dirichlet variable in $e_q^{\pm}$ and source quantity $S_q^{\pm}$, like $t_q^{(m)} c_e$ in Eq. (13), makes the closure relation and the optimal Λ weight independent. If one applies $S_q^+ = t_q^{(m)} c_e{}^{(m)} \mathcal{S}$ with $c_e{}^{(m)} \neq c_e$, the optimal solution in Eq. (14) should be replaced by $\Lambda = \frac{1}{(1-c_e{}^{(m)})}[\frac{1}{8} + \Lambda^-(c_e{}^{(m)} - c_e)]$. The disadvantage of this weight choice is that it makes Λ depending on the diffusion eigenfunction Λ^- and, in general, it violates Λ property.

Finally, we note that the so-called *third-order-accurate* velocity [34,35,49] and scalar [48,49] Dirichlet schemes support exactly Λ-independent parabolic solutions in an arbitrarily oriented channel. They make any other macroscopic solution *almost* Λ independent [34,35] because their closure relations shift the Λ dependency to truncation third order. The key point is that, unlike the parabolic interpolations [52,56,62], the *third-order-accurate* schemes do not reduce to BB or ABB for the midgrid location.

2. *Bounce-back zero-flux Neumann boundary rule*

Assume that the normal component of the advective velocity vanishes on the solid surface; the impermeable condition for the advective-diffusive flux then reduces to the zero diffusive flux condition $-D_0 \partial_n C = 0$, or Neumann condition $\partial_n C = 0$. In this study, the no flux is modeled either with the nonlocal specular-forward mirror reflection (SNL) in 2D straight channel, or with the bounce-back reflection (BB rule) in any geometry, including flow around circular-shaped inclusion. The two schemes coincide with the d2Q5 scheme at straight walls. In three dimensions, we will operate with the d3Q15 scheme and bounce-back reflection (d3Q15 BB). All considered schemes conserve mass exactly. It has been demonstrated [48] that the SNL mimics the impermeable wall without any restriction of the tangential flux. This property is confirmed by results [30,31], where the SNL allows for quasi-exact validation of the bulk truncation analysis for the first four moments with any equilibrium weights. The situation is different with the BB rule [48,64]. With the TRT operator (1) the BB reads as

$$f_{\bar{q}}(\boldsymbol{r}_{\rm b}, t+1) = [f_q + g_q^+ + g_q^-](\boldsymbol{r}_{\rm b}, t). \tag{15}$$

Applying the same procedure as for Eq. (11), the bounce-back steady-state closure equation becomes

$$\text{BB} \ : \ \left[e_q^- + \tfrac{1}{2} g_q^+ - \Lambda^- g_q^-\right]\big|_{\boldsymbol{r}_{\rm b}} = 0. \tag{16}$$

The closure relation (16) attempts to vanish the linkwise projection of the advective-diffusion flux $(t_q^{(a)} \boldsymbol{U} - D_0 t_q^{(m)} \nabla C) \cdot \boldsymbol{c}_q$ [it is given by $e_q^- - \Lambda^- g_q^- = t_q^{(a)} \boldsymbol{U} \cdot \boldsymbol{c}_q - c_e \Lambda^- t_q^{(m)} \partial_q C$ with the help of the first-order-accurate Chapman-Enskog expansion and Eq. (2)]. For illustration assume the pure-diffusion spread of the initial condition $C(x_0, y) = \delta(x - x_0)$ in a straight channel $y \in [-H/2, H/2]$. The specular-forward reflection provides the same solution as the periodic conditions on the flat walls: $C(x, y)$ remains y independent. However, the bounce back makes the concentration y dependent [the actual solution $C(x, y)$ is derived in Sec. III B and illustrated in Fig. 7]. In this situation, $e_q^- \equiv 0$, and the expected y-independent Chapman-Enskog bulk solution is $G_q^- = t_q^{(m)} c_e \partial_x C c_{qx}$ and $G_q^+ = -t_q^{(m)} c_e \Lambda^- \partial_x^2 C c_{qx}^2$. All these components vanish on the vertical link and it supports the no-flux condition exactly. All schemes (2) without diagonal mass weight $t_d^{(m)} = 0$ share this property and, in particular, the d2Q5 and d3Q7 schemes. Further, when $t_d^{(m)} \neq 0$, the sum of the diagonal links (with $c_{qx} = \pm 1$) in closure relations (16) maintains the leading-order expansion because the term of $\partial_x C c_{qx}$ vanishes. At the same time, the half-difference of the diagonal-link closure relations (16) yields at the leading order

$$\text{BB} \ : \ t_q^{(m)} c_e \partial_x C \approx 0. \tag{17}$$

That is, the bounce back tries to vanish the tangential diffusive flux unless when $t_d^{(m)} = 0$. In order to accommodate the closure relation (17) to the bulk solution, the system develops the nonequilibrium corrections $\delta g_q^{\pm}$ to the Chapman-Enskog solution $G_q^{\pm}$, and the solution becomes $g_q^{\pm} = G_q^{\pm} + \delta g_q^{\pm}$. Their generic form is described in Sec. II C.

The specular-forward reflection is free from the constraint (17) because the outgoing diagonal-link term $g_q^+ = t_q^{(m)} c_e \partial_x C$ serves to continue $C(\boldsymbol{r}_{\rm b}, t)$ to $C(\boldsymbol{r}_{\rm b} + c_{qx}, t+1)$. However, the *local* specular reflection, when the diagonal population returns into the node of departure, shares similar deficiency with the bounce back [69]. Very similar situation to Eq. (17) takes place in the presence of the constant advection velocity [48] when the bounce back tries to vanish the nonzero tangential advection flux via the diagonal links, unless when $t_d^{(a)} = 0$ in Eq. (2). It is expected that the situation is reversed on the diagonally oriented flat wall: the bounce back then attempts to vanish the tangential advective-diffusive flux, unless when $t_c^{(m)} = 0$ and $t_c^{(a)} = 0$.

The bounce-back closure relation (16) becomes second-order correct for the halfway linkwise flux location if Eq. (16) is replaced by

$$f_{\bar{q}}(\boldsymbol{r}_{\rm b}, t+1) = [f_q + g_q^+ + g_q^-](\boldsymbol{r}_{\rm b}, t) - 2\boldsymbol{c}_q \cdot (t_q^{(a)} \boldsymbol{U} - D_0 t_q^{(m)} \nabla C)|_{(\boldsymbol{r}_{\rm b} + \boldsymbol{c}_q)}. \tag{18}$$

The subtle point is that the (unknown) tangential diffusive-flux boundary value is required for that, unless when the cut link $\boldsymbol{c}_q$ is normal with the surface. The tangential diffusive flux [22,48] is derived locally from the actual nonequilibrium solution at the boundary node [see Eq. (56) from [48] and Eqs. (44) and (47)–(49) from [22]; we note a typo in their Eqs. (48) and (49), i.e., they should read with the opposite sign]. This correction is mass conserving on the flat wall due to the symmetry ($c_{qx} = \pm 1$ in our example), and it has been verified with a fully anisotropic d3Q15 scheme. A more careful, but nonlocal, interpolation procedure [62] extends the

construction of the tangential flux to a curved boundary. The three-population-based Neumann scheme [62] is worked out with the d2Q5 scheme and it has been not examined yet, either for full-weight stencil or in three dimensions. The two approaches [22,62] require prescribed tangential and normal wall coordinates, which are not well defined on a staircase boundary.

Remark. On the staircase wall segment with normal $\mathbf{n}$, the bounce-back no-flux closure relation (16) reads as the following solution for $g_q^{\pm}$ in the pure-diffusion modeled with the minimal schemes:

$$g_q^- = \tfrac{1}{2}c_e\big[\bar{\nabla}_{\boldsymbol{n}}C + \big(\Lambda - \tfrac{1}{4}\big)\bar{\Delta}_n^2[\bar{\nabla}_{\boldsymbol{n}}C]\big]c_{qn},$$
$$g_q^+ = -\tfrac{1}{2}\Lambda^- c_e\big[\bar{\Delta}_n^2 C + \big(\Lambda - \tfrac{1}{4}\big)\bar{\Delta}_n^2\big[\bar{\Delta}_n^2 C\big]\big]c_{qn}^2, c_{qn}^2 = 1. \tag{19}$$

These relations are derived from the exact steady-state recurrence equations (20) and they are expressed via the exact central-difference operators along the normal direction. At the second order they reduce to the Chapman-Enskog solution employed above with $g_q^- = t_q^{(m)}c_e\partial_n C c_{qn}$ and $g_q^+ = -t_q^{(m)}c_e\Lambda^-\partial_n^2 C c_{qn}^2$. When $\Lambda = \frac{1}{4}$, the diffusive-flux condition (16) is set midgrid with Eqs. (19) *in the finite-difference sense*, as $\frac{1}{2}g_q^+ - \Lambda^- g_q^- = -D_0[\bar{\nabla}_{\boldsymbol{n}}C + \frac{1}{2}\bar{\Delta}_n^2 C]|\boldsymbol{r}_{\rm b} = 0$. Since $\Lambda = \frac{1}{4}$ also produces the finite-difference-type discretization of the mass-conservation equation [20,30], its solutions can be expected to match the finite-difference reference solutions best (we discuss this for effective diffusivity in Sec. VI A).

C. Nonequilibrium boundary-layer corrections

The numerical assessment [69] confirms the validity of the steady-state framework for construction of the boundary layers and their impact on the transport coefficients in Taylor-dispersion regime. At steady state, the two pairs of the recurrence equations [32] of the TRT scheme become

$$g_q^{\pm}(\boldsymbol{r}) = \big[\bar{\Delta}_q e_q^{\mp} - \Lambda^{\mp}\bar{\Delta}_q^2 e_q^{\pm} + \big(\Lambda - \tfrac{1}{4}\big)\bar{\Delta}_q^2 g_q^{\pm}\big](\boldsymbol{r}),$$
$$q = 0, \ldots Q_m \tag{20a}$$
$$\big[\bar{\Delta}_q^2 e_q^{\pm} - \Lambda^{\pm}\bar{\Delta}_q^2 g_q^{\pm} - \bar{\Delta}_q g_q^{\mp}\big](\boldsymbol{r}) = 0, q = 1, \ldots Q_m. \tag{20b}$$

These equations are expressed in terms of the linkwise-central spatial finite-difference operators. These equations remain satisfied if we disturb the set $\{g_q^{\pm}(\boldsymbol{r})\}$ by the *boundary-layer nonequilibrium correction* $\{\delta g_q^{\pm}(\boldsymbol{r})\}$ which obeys

$$\delta g_q^{\pm}(\boldsymbol{r}) = \big(\Lambda - \tfrac{1}{4}\big)\bar{\Delta}_q^2\delta g_q^{\pm}(\boldsymbol{r}), \tag{21a}$$
$$\big[\Lambda^{\pm}\bar{\Delta}_q^2\delta g_q^{\pm} + \bar{\Delta}_q\delta g_q^{\mp}\big](\boldsymbol{r}) = 0, q = 1, \ldots Q_m. \tag{21b}$$

Following [32,69], consider the grid nodes $\boldsymbol{r}_n = \boldsymbol{r}_0 + n\boldsymbol{c}_q$ along the lattice direction $\boldsymbol{c}_q$ from one boundary end at $\boldsymbol{r} = \boldsymbol{r}_0$ to another at $\boldsymbol{r}_N = \boldsymbol{r}_0 + N\boldsymbol{c}_q$ (see Fig. 2). When $\Lambda = \frac{1}{4}$, $\delta g_q^{\pm}(\boldsymbol{r}) \neq 0$ only in two boundary nodes $\boldsymbol{r}_{\rm b} = \{\boldsymbol{r}_0, \boldsymbol{r}_N\}$ because it vanishes in bulk according to Eq. (21a). When $\Lambda \neq \frac{1}{4}$, the solution of Eqs. (21) decays as $\delta g_q^{\pm}(\boldsymbol{r}_n) = a_q^{\pm}k_\sigma^n + b_q^{\pm}k_\sigma^{-n}$, where $\{a_q^{\pm}, b_q^{\pm}\}$ are linkwise constant and k_σ has two roots:

$$\Lambda \neq \frac{1}{4} : k_\sigma = \frac{2\sqrt{\Lambda} - \sigma}{2\sqrt{\Lambda} + \sigma}, \sigma = \pm 1, \sqrt{\Lambda^+}a_q^+ = \sigma\sqrt{\Lambda^-}a_q^-,$$
$$\sqrt{\Lambda^+}b_q^+ = -\sigma\sqrt{\Lambda^-}b_q^-, \tag{22a}$$
$$\Lambda = \frac{1}{4} : \delta g_q^{\mp}(\boldsymbol{r}_0) = \frac{\delta g_q^{\pm}(\boldsymbol{r}_0)}{2\Lambda^{\mp}},$$
$$\delta g_q^{\mp}(\boldsymbol{r}_N) = -\frac{\delta g_q^{\pm}(\boldsymbol{r}_N)}{2\Lambda^{\mp}}, \quad \text{with } 2\Lambda^{\mp} = \frac{1}{2\Lambda^{\pm}}. \tag{22b}$$

The relations (22b) between different parity components are obtained from Eq. (21b). If we assume that $k = k_1$ ($\sigma = 1$), then $|k| < 1$ and the solution of Eqs. (21) with (22a), satisfying the prescribed boundary values $\delta g_q^+(n = 0) = \delta g_q^+(\boldsymbol{r}_0)$ and $\delta g_q^+(n = N) = \delta g_q^+(\boldsymbol{r}_N)$, reads as

$$\delta g_q^+(\boldsymbol{r}_n) = p_N(n)\delta g_q^+(\boldsymbol{r}_N) + p_0(n)\delta g_q^+(\boldsymbol{r}_0),$$
$$p_N(n) = \frac{k^n - k^{-n}}{k^N - k^{-N}},$$
$$p_0(n) = \frac{k^{(N-n)} - k^{-(N-n)}}{k^N - k^{-N}}. \tag{23}$$

Let us assume the solution at the ends to be related by the symmetry argument, e.g., $[\boldsymbol{r}_0, \boldsymbol{r}_N]$ is perpendicular to the symmetry axis in straight channel or it goes through the center of the circle (see Fig. 2). Then, two possible situations can be considered. First, $\delta g_q^+(\boldsymbol{r}_N) = -\delta g_q^+(\boldsymbol{r}_0)$, $\delta g_q^-(\boldsymbol{r}_N) = \delta g_q^-(\boldsymbol{r}_0)$, and Eq. (23) becomes

$$\delta g_q^+(\boldsymbol{r}_n) = P(n)\delta g_q^+(\boldsymbol{r}_N),$$
$$P(n) = \frac{k^n - k^{(N-n)}}{k^N - 1}, P(N) = -P(0) = 1, \tag{24a}$$
$$\delta g_q^-(\boldsymbol{r}_n) = \frac{\sqrt{\Lambda}}{\Lambda^-}M(n)\delta g_q^+(\boldsymbol{r}_N),$$
$$M(n) = \frac{k^n + k^{(N-n)}}{k^N - 1}, M(N) = M(0) = \frac{k^N + 1}{k^N - 1}. \tag{24b}$$

Second, $\delta g_q^+(\boldsymbol{r}_N) = \delta g_q^+(\boldsymbol{r}_0)$, $\delta g_q^-(\boldsymbol{r}_N) = -\delta g_q^-(\boldsymbol{r}_0)$, and Eq. (23) becomes

$$\delta g_q^+(\boldsymbol{r}_n) = \mathcal{P}(n)\delta g_q^+(\boldsymbol{r}_N), \quad \mathcal{P}(n) = \frac{k^N - 1}{k^N + 1}M(n), \tag{25a}$$
$$\delta g_q^-(\boldsymbol{r}_n) = \frac{\sqrt{\Lambda}}{\Lambda^-}\mathcal{M}(n)\delta g_q^+(\boldsymbol{r}_N), \mathcal{M}(n) = \frac{k^N - 1}{k^N + 1}P(n). \tag{25b}$$

The functions $P(n)$, $M(n)$, and $\mathcal{P}(n)$, $\mathcal{M}(n)$ are plotted in Fig. 3: they monotonously decay towards the center when $\Lambda > \frac{1}{4}$ and they oscillate when $\Lambda < \frac{1}{4}$. When $\Lambda = \frac{1}{4}$, they are constrained to two boundary nodes.

In this study, the mismatch between the bulk component $\{G_q^{\pm}(\boldsymbol{r}, t)\}$ given by the Chapman-Enskog expansion and the effective solution $g_q^{\pm}$ of the scheme in straight channel and a cylindrical capillary is described in terms of the boundary-layer corrections $\{\delta g_q^{\pm}(\boldsymbol{r})\}$ given by Eqs. (24) and (25). In these

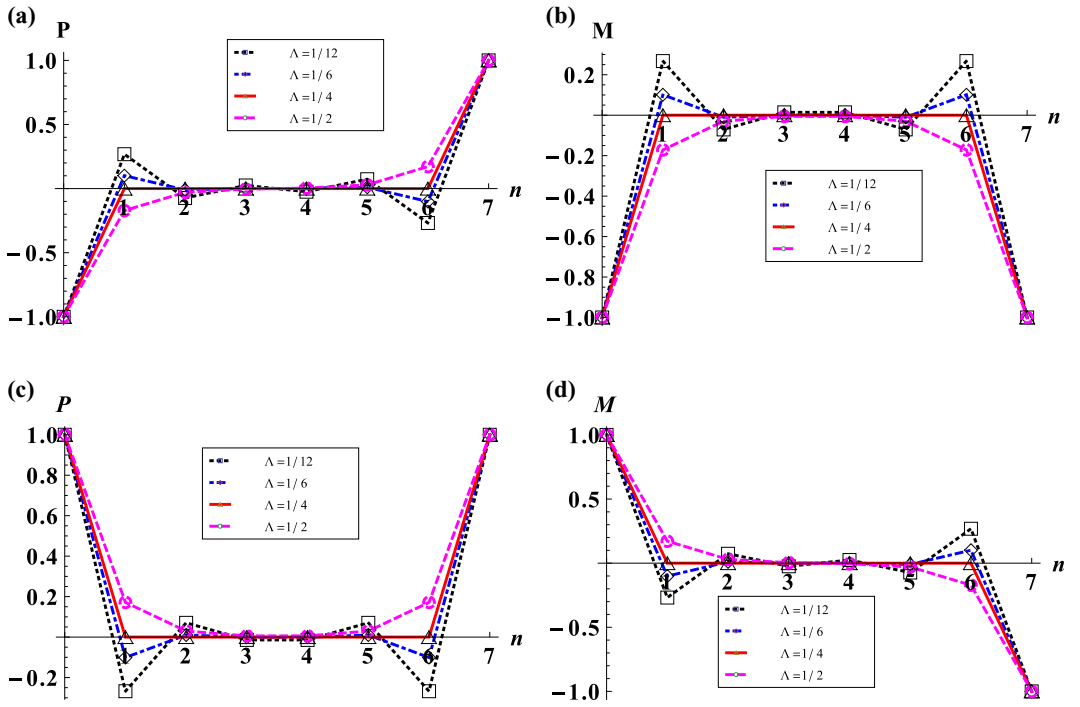

FIG. 3. This figure plots the functions (a) $P(n)$ and (b) $M(n)$ defined in Eq. (24), then (c) $\mathcal{P}(n)$ and (d) $\mathcal{M}(n)$ from Eq. (25), when $\Lambda = \frac{1}{12}$ (dotted line, "squares," black), $\Lambda = \frac{1}{6}$ (dotted-dashed line,"lozenges," blue), $\Lambda = \frac{1}{2}$ (dashed line, "circles," magenta). The $\Lambda = \frac{1}{4}$ (solid line, "triangles," red) is constrained to the boundary points. The two functions (a) and (b) produce (for $n = 0,1,\ldots,7$) the boundary-layer solution in straight channel of $H = 8$ displayed in Figs. 5 and 6.

corrections, the boundary values $\{\delta g_q^+(\boldsymbol{r}_N)\}$ will be derived from the closure relation of the bounce-back rule.

III. BOUNCE-BACK SPURIOUS EFFECTS

In this section, we will construct the nonequilibrium corrections $\{\delta g_q^{\pm}(\boldsymbol{r})\}$ due to the bounce-back unphysical tangential constraint. This derivation is illustrated for a cylindrical capillary by extending the channel solution [69]. We also extend it to the fourth order for pure diffusion in a straight channel where the transverse y dependency in concentration, induced by the bounce back, is analytically restored. The exact (channel) and approximate (capillary) solutions are built for spurious modifications of Eq. (7). They are (i) due to the diagonal mass weight in diffusion coefficient (Sec. III A) and kurtosis (Sec. III B); (ii) due to the anti-numerical-diffusion weight stencil in diffusion coefficient (Sec. III C); (iii) due to the diagonal velocity weight in apparent velocity (Sec. III D), for plug (Sec. III D 1) and parabolic (Sec. III D 2) profiles, and the associated dispersion coefficient (Sec. III E). In the presence of boundary corrections $\{\delta g_q^{\pm}(\boldsymbol{r})\}$, the closure relation (16) with $w_q = 0$ reads as

$$\text{BB}: \left[e_q^- + \tfrac{1}{2}(G_q^+ + \delta g_q^+) - \Lambda^-\left(G_q^- + \delta g_q^-\right)\right]\Big|_{\boldsymbol{r}_b} = 0,$$
$$g_q^{\pm}(\boldsymbol{r}) = G_q^{\pm}(\boldsymbol{r}) + \delta g_q^{\pm}(\boldsymbol{r}). \tag{26}$$

The present analysis will also apply if w_q in Eq. (15) is set equal to projection of the prescribed boundary advective-diffusive normal-flux value on velocity $\boldsymbol{c}_q$ (see [27]). The d2Q9 and d3Q15 schemes yield a very similar discretization in boundary nodes when the coordinate discrete-velocity links are normal with the staircase solid wall (see Fig. 2). Assuming the rotation invariance of the boundary-layer solution over the circular cross section, and thus partly neglecting the discretization effect, we apply the straight-channel methodology [69] along the coordinate axis in cylindrical capillary. On this basis, Eqs. (24) and (25) are applied uniformly, either for $n = 0,1,\ldots,N = H-1$ along the y axis in straight channel, or for $n = 0,1,\ldots,N = 2R-1$ along one of the coordinate axis $\{y,z\}$ in circle.

A. Bounce-back diffusion-coefficient correction $\text{err}_D^{(bb)}$

Assume first pure-diffusion simulation where we measure the apparent diffusion coefficient $D^{(\text{num})} = \frac{\mu_2^*(t+\delta_t)-\mu_2^*(t)}{2\delta_t}$ with the help of Eq. (8). In straight channel, the d2Q9 SNL produces exact solution $D^{(\text{num})} \equiv D_0$, for all mass weights [30,31,69]. This property is achieved by the d2Q9 BB only when $t_c^{(m)} = \frac{1}{2}$ and, in particular, with the d2Q5 BB. We first find by numerical computations that in cylindrical capillary, $D^{(\text{num})} \equiv D_0$ with the d3Q15 BB when $t_c^{(m)} = \frac{1}{2}$, and, in particular, with the d3Q7 BB. Thereby, in both geometries the minimal d2Q5 and d3Q7 schemes assure the diffusion coefficient exactly. Otherwise, since the diffusion flux is restricted to zero at flat solid boundary via Eq. (17) when $t_c^{(m)} \neq \frac{1}{2}$, $w_q = 0$, $D^{(\text{num})}$ is smaller than the predicted value $D_0 = c_e\Lambda^-$. This retardation of the diffusion spreading is demonstrated in Fig. 4 for relative correction $\text{err}_D^{(bb)} = \frac{D^{(\text{num})}}{D_0} - 1$. This correction is proportional to the diagonal mass-weight value $t_d^{(m)} = (1-2t_c^{(m)})/N_d$ and it depends on Λ and radius R. Thereby, we look for it in the

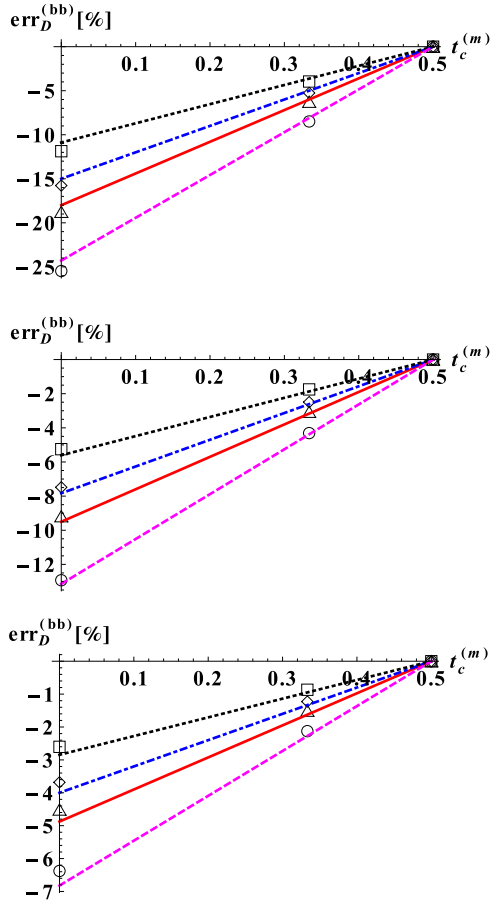

FIG. 4. This figure compares pure-diffusion numerical results (symbols) by d3Q15 bounce-back scheme for its relative error in diffusion coefficient to its theoretical prediction $\mathrm{err}_D^{(bb)} = \delta_m$ (straight lines) given by Eq. (27) with Eq. (35) for $k_T = 0$. From the top to the bottom: $R = \{5,10,20\}$. The results are plotted for $\Lambda = \{\frac{1}{12}, \frac{1}{6}, \frac{1}{4}, \frac{1}{2}\}$ with dotted line (black), dotted-dashed line (blue), solid line (red), dashed line (magenta).

form for characteristic length $\mathcal{L}$:

$$\mathrm{err}_D^{(bb)}\left(t_c^{(m)},\Lambda,\mathcal{L}\right) = \frac{\delta_m}{1+k_T}, \delta_m\left(t_c^{(m)},\Lambda,\mathcal{L}\right) = F^{(m)}(\Lambda,\mathcal{L})\left(1-2t_c^{(m)}\right). \quad (27)$$

In pure diffusion and plug flow, Eq. (27) reads as $k_T = 0$.

Nonequilibrium corrections. We look for the functional form of $F^{(m)}(\Lambda,\mathcal{L})$. Since the corrections $\{\delta g_q^{\pm}(\boldsymbol{r})\}$ should accommodate $t_q^{(m)} c_e \partial_x C(\boldsymbol{r}_b)$ [cf. Eq. (17)] in boundary nodes $\boldsymbol{r}_b = \{\boldsymbol{r}_0, \boldsymbol{r}_N\}$, we employ, on the symmetry argument, Eq. (24) in the following form:

$$\delta g_q^{+}(\boldsymbol{r}_n) = \mathcal{K}_1 P(n)\partial_x C(\boldsymbol{r}_N) c_{qx} c_{q\alpha}, \alpha = \{y,z\}$$
$$\delta g_q^{-}(\boldsymbol{r}_n) = \frac{\sqrt{\Lambda}}{\Lambda^-}\mathcal{K}_1 M(n)\partial_x C(\boldsymbol{r}_N) c_{qx} c_{q\alpha}^2, n = 0,1,\ldots,N. \quad (28)$$

It satisfies Eqs. (21) along the coordinate axis α, with $\bar{\Delta}_q = \bar{\Delta}_\alpha c_{q\alpha}$, $\bar{\Delta}_q^2 = \Delta_\alpha^2 c_{q\alpha}^2$, $\delta g_q^{+}(\boldsymbol{r}_N) = \mathcal{K}_1 \partial_x C(\boldsymbol{r}_N) c_{qx} c_{q\alpha}$. We look now for the coefficient $\mathcal{K}_1$. Let us decompose $C(x,\boldsymbol{r})$ into its averaged value $\bar{C}(x)$ and the fluctuation $C'(x,r)$:

$$C(x,r) = \bar{C}(x) + C'(x,r), \bar{C}(x) = \langle C\rangle, \langle C'(x,r)\rangle = 0. \quad (29)$$

The fourth-order analysis in Sec. III B will show that the difference between $\partial_x \bar{C}(x)$ and $\partial_x C(\boldsymbol{r}_N)$ behaves as $O(\partial_x^3 \bar{C})$, that is, the $\partial_x \bar{C}(x)$ in Eqs. (28) will produce the same second-order result as the $\partial_x C(\boldsymbol{r}_N)$. This approximation was adopted for channel [69]. We now consider the closure relation (26) where the second-order steady-state expansion for $G_q^{\pm}(\boldsymbol{r})$ reads as

$$G_q^{-}(\boldsymbol{r}) = t_q^{(m)} c_e \left[\sum_{\alpha=1}^{d} \partial_\alpha c_{q\alpha}\right] C(\boldsymbol{r}), G_q^{+}(\boldsymbol{r}) = -\Lambda^- t_q^{(m)} c_e \left[\sum_{\alpha=1}^{d} \partial_\alpha c_{q\alpha}\right]^2 C(\boldsymbol{r}). \quad (30)$$

Assume $\alpha = y$, then the populations outgoing at $\boldsymbol{r}_N$ have the same component c_{qy}. In d3Q15, we first sum the closure relations (26) for the outgoing populations with $c_{qz} = \pm 1$, then the terms like $t_q^{(m)} c_e \partial_z C(\boldsymbol{r}_N) c_{qz}$ and $-\Lambda^- t_q^{(m)} c_e \partial_\beta \partial_z C(\boldsymbol{r}_N) c_{q\beta} c_{qz}$, $\beta = \{x,y\}$ vanish from those sums. The difference of the obtained diagonal closure relations with $c_{qx} = \pm 1$ is now addressed. The term $t_q^{(m)} c_e \partial_y \bar{C}(\boldsymbol{r}_N) c_{qy}$ vanishes from it, as well as the remaining terms from G_q^{+} [except the term $-\Lambda^- t_q^{(m)} c_e \partial_x \partial_y \bar{C}(\boldsymbol{r}_N) c_{qx} c_{qy}$ which is of higher order]. Thereby, by substituting Eq. (28) and employing $\partial_x C(\boldsymbol{r}_N) \approx \partial_x \bar{C}(x)$, the *first-order-accurate* linear combination of the closure relations reads as

$$\frac{1}{2}\left\{\mathcal{K}_1 P(N) - 2\Lambda^-\left[t_d^{(m)} c_e + \mathcal{K}_1 \frac{\sqrt{\Lambda}}{\Lambda^-} M(N)\right]\right\}\partial_x \bar{C}(x) = 0,$$
$$\text{then} \quad \mathcal{K}_1 = \frac{2c_e \Lambda^- t_d^{(m)}}{1 - 2\sqrt{\Lambda} M(N)}. \quad (31)$$

Solution (31) for the coefficient $\mathcal{K}_1$ in the nonequilibrium correction (28) has the same form in straight channel and cylindrical capillary.

Numerical validation. Figures 5 and 6 compare theoretical prediction for $\{\delta g_q^{\pm}(x,y)\}$ given by Eqs. (28) and (31) to numerical results, when $\Lambda = \frac{1}{12}$ and $\frac{1}{4}$, respectively. Pure-diffusion simulations are run in a straight channel for $H = 8$ and 40. The numerical values of the nonequilibrium components $g_q^{-}(x_c,y) = G_q^{-} + \delta g_q^{-}$ and $g_q^{+}(x_c,y) = G_q^{+} + \delta g_q^{+}$ are monitored at $x = x_c$ and projected on the relevant basis vectors, such as $\mathbf{c}_x = \{c_{qx}\}$, $\mathbf{q}_x = \{c_{qx}(3c_{qy}^2 - 2)\}$, and $\mathbf{v}_{xy} = \{c_{qx}c_{qy}\}$. The bulk components $G_q^{-}(x_c,y) = t_q^{(m)} c_e \partial_x \bar{C}(x_c) c_{qx}$ and $G_q^{+}(x_c,y) = -2\Lambda^- t_q^{(m)} c_e \partial_x \partial_y C(x_c,y) c_{qx} c_{qy}$ are approximated with the help of the central finite differences. Equations (28) are computed by replacing $\partial_x C(\boldsymbol{r}_N)$ by $\partial_x \bar{C}(x_c)$. The predictions and numerical results are projected on the relevant basis vectors of the d2Q9 scheme.

The numerical results validate the constructed solution and manifest the expected properties of the boundary-layer components: while for $\Lambda = \frac{1}{4}$ (Fig. 6) they are constrained to the two boundary nodes, they oscillate for $\Lambda = \frac{1}{12}$ (Fig. 5) in bulk and exponentially decay towards the center. As the space resolution increases, the boundary-layer nonequilibrium

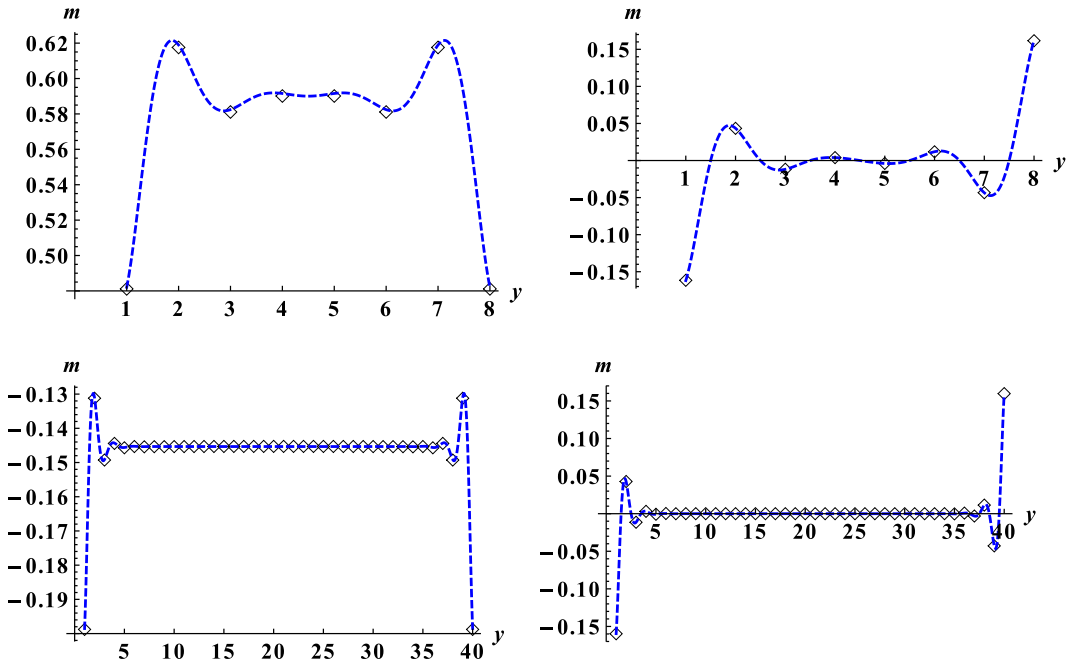

FIG. 5. The pure diffusion in straight channel is modeled by d2Q9 BB with $\Lambda = \frac{1}{12}$, $t_c^{(m)} = \frac{1}{4}$. The two first diagrams compare, respectively, the predicted projections (lines) for (i) $m = \frac{[g_q^-(x_c,y)\cdot \mathbf{c}_x]}{||\mathbf{c}_x||^2}$, $\mathbf{c}_x = \{c_{qx}\}$, and (ii) $m = \frac{[g_q^+(x_c,y)\cdot \mathbf{v}_{xy}]}{||\mathbf{c}_x||^2}$, $\mathbf{v}_{xy} = \{c_{qx}c_{qy}\}$, to their numerical values (symbols) at grid points $y = 1,2,\ldots,H = 8$. The two last diagrams display results for $H = 40$, with $m = \frac{[g_q^-(x_c,y)\cdot \mathbf{q}_x]}{||\mathbf{q}_x||^2}$, $\mathbf{q}_x = c_{qx}(3c_{qy}^2 - 2)$, and $m = \frac{[g_q^+(x_c,y)\cdot \mathbf{v}_{xy}]}{||\mathbf{v}_{xy}||^2}$. The nonequilibrium solution $g_q^{\pm} = G_q^{\pm} + \delta g_q^{\pm}$ is predicted by Eqs. (28) and (30); it is monitored at grid node $x_c = x_0 - 1$ at some time t and normalized by $\max_x \partial_t \bar{C}(x,t)$.

corrections with $\Lambda = \frac{1}{12}$ confine to two to three boundary-node neighbors (see two last diagrams in Fig. 5).

Diffusion-coefficient correction. According to the Chapman-Enskog analysis and recurrence equations [30,31], the diffusion form in the right-hand side of the averaged mass-conservation equation (7) is created by the term $\Lambda^-\langle\sum_{q=1}^{Q_m} \bar{\Delta}_x G_q^- c_{qx}\rangle$. Let us apply similar argument to $\{\delta g_q^-\}$. The correction $\Lambda^-\langle\sum_{q=1}^{Q_m} \bar{\Delta}_x \delta g_q^- c_{qx}\rangle$ [Eqs. (28) and (31)] then modifies the diffusion coefficient D_0 by the

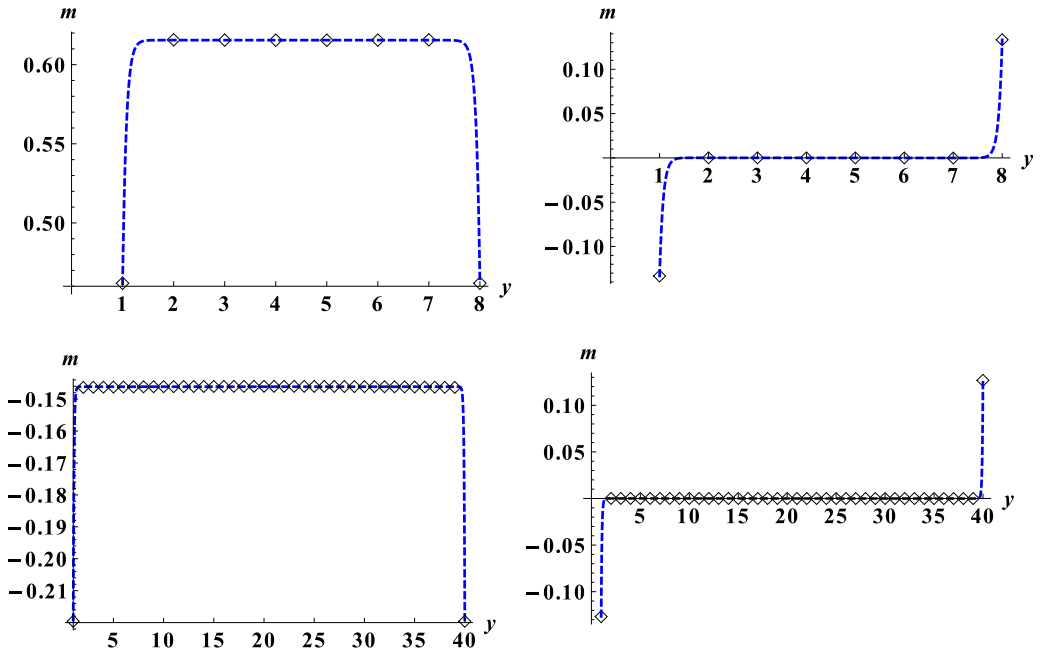

FIG. 6. Similarly as in Fig. 5 but for $\Lambda = \frac{1}{4}$.

quantity $\delta_m c_e \Lambda^-$ and the apparent second-order-accurate diffusion equation becomes [cf. Eq. (2)]

$$\partial_t \bar{C} = c_e \Lambda^- (1+\delta_m)\partial_x^2 \bar{C}, \text{ with } \delta_m = \langle \delta_m(n) \rangle \tag{32}$$

$$\delta_m(n) = \Lambda^- \frac{\mathcal{K}_1}{c_e \Lambda^-} \frac{\sqrt{\Lambda}}{\Lambda^-} M(n) t_d^{(m)} N_d$$

$$= \frac{2\sqrt{\Lambda} M(n)}{1 - 2\sqrt{\Lambda} M(N)} \left(1 - 2t_c^{(m)}\right). \tag{33}$$

In straight channel, the average values are computed via the arithmetical mean of the grid-node solution. In a circle, we apply the following approximation:

$$\langle \delta_m(r) \rangle = \frac{2\pi}{\pi R^2} \int_0^R r \delta_m(r) dr \approx \frac{2\pi}{\pi R^2} \sum_{n=0}^{R-1} r(n) \delta_m(n),$$

$$r(n) = R - n - \frac{1}{2}, n = 0,1, \ldots R-1. \tag{34}$$

In that we express $\langle M(n) \rangle$ via the function $\Psi(\Lambda, \mathcal{L})$ given by Eq. (A1) in straight channel and Eqs. (A2) and (A3) in cylindrical capillary. The relative diffusion-coefficient correction δ_m obtains the closed-form expression

$$\delta_m = F^{(m)}(\Lambda, \mathcal{L}) \left(1 - 2t_c^{(m)}\right),$$

$$F^{(m)}(\Lambda, \mathcal{L}) = -\frac{2\sqrt{\Lambda}}{l} \Psi(\Lambda, \mathcal{L}), \tag{35a}$$

$$\delta_m \left(\Lambda = \frac{1}{4}\right) = -\frac{\left(1 - 2t_c^{(m)}\right)}{l}, \tag{35b}$$

$$\delta_m|_{\mathcal{L} \to \infty} = -\frac{2\sqrt{\Lambda}}{l} \left(1 - 2t_c^{(m)}\right), \ \forall \Lambda \tag{35c}$$

with

$$\text{Channel}: l = \mathcal{L} = H,$$

$$\Psi(\Lambda, \mathcal{L}) = \Psi^{(s)}(\Lambda, H), \phi(\Lambda, \mathcal{L}) = \phi^{(s)}(\Lambda, H), \tag{36a}$$

$$\text{Circle}: l = \frac{2R^2}{2R-1}, \quad \mathcal{L} = R,$$

$$\Psi(\Lambda, \mathcal{L}) = \Psi^{(c)}(\Lambda, R), \phi(\Lambda, \mathcal{L}) = \phi^{(c)}(\Lambda, R). \tag{36b}$$

According to Eqs. (35), δ_m is nonpositive and it decays towards zero as Λ decreases; δ_m vanishes for $t_c^{(m)} = \frac{1}{2}$; its amplitude linearly increases with the diagonal weight value $t_d^{(m)}$, $\forall \Lambda$. In straight channel [69], Eq. (35) with Eq. (36a) predicts δ_m *exactly*.

Numerical validation. Figure 4 compares the numerical results and analytical prediction for δ_m in the capillary of radius $R = \{5,10,20\}$. The principal dependency $F^{(m)}(\Lambda, \mathcal{L})$ over Λ and R is captured well but, unlike in straight channel, the result (35) is not exact in circular shape because of the discretization effect, partly neglected by this construction. The agreement is even better for $R = 10$ than for $R = 20$: we relate this to the smaller discretization error for $R = 10$ (this is observable in Table I). Further, numerical computations confirm that $\text{err}_D^{(bb)}$ takes the same value in constant (plug) flow (when the velocity weight $t_c^{(a)} = \frac{1}{2}$ and boundary-layer dispersion effect is absent).

Summary. The relative diffusion boundary-layer effect of $\text{err}_D^{(bb)}$ is independent of the velocity amplitude. Asymptotically, as mesh-resolution prefactor l increases, the relative correction to diffusion coefficient δ_m behaves as $-2\sqrt{\Lambda}(1 - 2t_c^{(m)})/l$; $\Lambda = \frac{1}{4}$ yields this behavior for any l. It is shown [69] that the scale factor $\sqrt{\Lambda}$ is reached very rapidly. In duct flow, δ_m can be measured from the pure-diffusion simulation for any D_0.

The actual value $\delta_m D_0$ should be then subtracted from the obtained value $D^{(\text{num})}$ in order to obtain the effective bulk solution of the scheme, e.g., the effective Taylor-dispersion coefficient. This procedure is applied [30] in order to verify the truncation dispersion analysis for Poiseuille flow in a capillary. It should be noted that in duct flows, $\text{err}_D^{(bb)}$ in Eq. (27) asymptotically decreases to zero as k_T increases with Pe. It follows that the first-order boundary-layer diffusion effect is most relevant in pure diffusion, plug-type flow, and for small Pe. In the presence of the solid obstacles, the effective diffusion coefficient D_{eff} in Eq. (7) is different from D_0 and it is unknown in general. The dependency of D_{eff} on the mass weight in pure diffusion spread around rectangular and circle obstacles is preliminarily examined in Sec. VI A.

B. Boundary-layer effect in kurtosis

Truncation predictions. In this section, we quantify the modification in kurtosis due to the bounce-back restriction of the tangential flux in the pure-diffusion simulations in straight channel. The fourth-order-accurate diffusion equation [20,30,31] reads as

$$\partial_t C = D_0 \partial_x^2 C + A_3 \partial_x^4 C, D_0 = c_e \Lambda^-,$$

$$A_3(c_e, \Lambda^-, \Lambda) = c_e \Lambda^- \left(\Lambda - \tfrac{1}{6}\right) - c_e^2 \Lambda^- \left[(\Lambda^-)^2 + \Lambda - \tfrac{1}{4}\right]. \tag{37}$$

In the absence of the truncation correction ($A_3 = 0$), one expects the initial Dirac δ function $C(\boldsymbol{r}, t=0) = \delta(x - x_0)$ to spread with the Gaussian distribution where kurtosis is zero in Eqs. (8) and (9): $\text{Ku}(t) = 0$, $\text{Ku}_\star \equiv 0$. However, because of truncation correction, $\text{Ku}_\star^{(\text{tr})}$ gets the solution [30]

$$\text{Ku}_\star^{(\text{tr})} = \text{Ku}(t) t = \frac{6A_3}{D_0^2}, \text{Ku}_\star^{(\text{tr})} = 0 \text{ if } \Lambda = \frac{1}{6}, (\Lambda^-)^2 = \frac{1}{12}. \tag{38}$$

The $\text{Ku}_\star^{(\text{tr})}$ is nonzero except for "optimal-diffusion" choice [20]: $\Lambda = \frac{1}{6}$, $(\Lambda^-)^2 = \frac{1}{12}$ where $A_3 = 0$. Since A_3 is mass weight independent, $\text{Ku}_\star^{(\text{tr})}$ is $\{t_q^{(m)}\}$ independent in pure diffusion in straight channel. Furthermore, $\text{Ku}_\star^{(\text{tr})}$ is independent of the space resolution and it is set by c_e, Λ^-, and Λ. The simulations [30] for diffusion spread of the Dirac plume are conducted in straight channel of width $H = \{2,4,8,20,40\}$ applying the d2Q9 SNL scheme. The $\text{Ku}_\star^{(\text{num})}$ is derived from the fourth-order moment with Eqs. (8) and (9). It is verified [30] that the predicted solution (38) is quasi-exact on the numerical measurements of $\text{Ku}_\star^{(\text{num})}$. Since $\text{Ku}_\star$ is $t_q^{(m)}$ independent, this result is the same with the d2Q5 BB and d2Q9 BB when $t_c^{(m)} = \frac{1}{2}$.

Numerical results with the BB rule. The two first diagrams in Fig. 7 compare Eq. (38) for $\text{Ku}_\star^{(\text{tr})}$ to the numerical results of

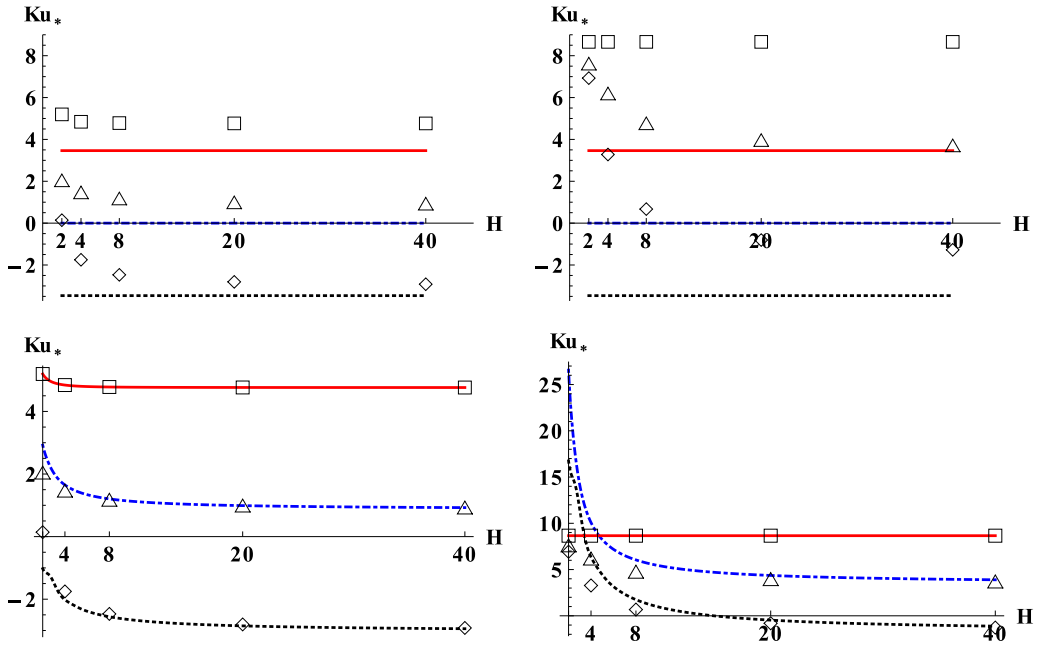

FIG. 7. Pure diffusion in straight channel. In two first diagrams, the (horizontal) lines plot $t_c^{(m)}$- and H-independent truncation prediction (38) for $\mathrm{Ku}_\star^{(\mathrm{tr})}$ when $\{c_e,\Lambda^-\}=\{\frac{1}{3},\sqrt{\frac{1}{12}}\}$ and $\Lambda=\{\frac{1}{12},\frac{1}{6},\frac{1}{4}\}$ [solid line (red), dotted-dashed line (blue), dotted line (black)]. In two last diagrams, the lines plot $t_c^{(m)}$- and H-dependent bounce-back prediction (46). The numerical results of the d2Q9 BB ("empty" symbols) are computed with $t_c^{(m)}=\frac{1}{4}$ in the first (third) diagrams and with $t_c^{(m)}=0$ in the second (fourth) diagrams.

the d2Q9 BB scheme with nonzero mass-weight values, when $\{t_c^{(m)}=\frac{1}{4},t_d^{(m)}=\frac{1}{8}\}$ and $\{t_c^{(m)}=0,t_d^{(m)}=\frac{1}{4}\}$, respectively. In these simulations, similarly to what has been reported [69], Eq. (35) is exact and $D^{(\mathrm{num})}\equiv D_0[1+\delta_m(t_c^{(m)},\Lambda,H)]$. Further, we observe that, unlike with the d2Q9 SNL, $\mathrm{Ku}_\star^{(\mathrm{num})}$ deviates from Eq. (38). The deviation depends on the mass weight $t_c^{(m)}$, channel width H, and Λ. Namely, the discrepancy with Eq. (38) clearly increases with $t_d^{(m)}$. The surprising result is that $\mathrm{Ku}_\star^{(\mathrm{num})}$ does not converge to Eq. (38) when H increases. This is evidenced for $\Lambda=\frac{1}{4}$ in the second and fourth diagrams where $t_c^{(m)}=0$: $\mathrm{Ku}_\star^{(\mathrm{num})}$ is H independent but its value is different from $\mathrm{Ku}_\star^{(\mathrm{tr})}$ in Eq. (38). This result cannot be explained by the diffusion-coefficient correction δ_m alone because δ_m converges to zero as H^{-1}. In order to explain this result, we extend the analysis of the diffusion boundary-layer effect to the fourth order.

The fourth-order boundary-layer effect. The second-order analysis derives the relative diffusion-coefficient correction δ_m given by Eq. (35). This correction is due to the boundary-layer nonequilibrium component (28). We look for its modification in the truncation coefficient in Eq. (37): $A_3\to A_3^{bb}$ and then $\mathrm{Ku}_\star\to\mathrm{Ku}_\star^{bb}$. The fourth-order-accurate diffusion equation for the averaged concentration $\bar{C}(x,t)$ is then looked for as

$$\partial_t\bar{C}(x,t)=c_e\Lambda^-(1+\delta_m)\partial_x^2\bar{C}+A_3^{bb}\partial_x^4\bar{C}+O(\epsilon^6),$$
$$\mathrm{Ku}_\star^{bb}=\frac{6A_3^{bb}}{[c_e\Lambda^-(1+\delta_m)]^2}. \tag{39}$$

The key point is that, because of the bounce back, the concentration solution becomes y dependent: $C(x,y)=\bar{C}(x)+C'(x,y)$ [cf. Eq. (29)]. Recall that Eq. (31) has been derived under assumption that $\partial_x C(x,y_b)=\partial_x\bar{C}(x)+\partial_x C'(x,y_b)\approx\partial_x\bar{C}(x)+O(\epsilon^3)$, here $\boldsymbol{r}_N=(x,y_b)$. A preliminary inspection suggests that the asymptotically constant modification in $\mathrm{Ku}_\star$ may originate from the omitted term $\bar{\Delta}_x^2C'(x,y_b)$. Assume the fourth-order polynomial solution for $C'(x,y)$:

$$C'(x,y)=a_0(x)y^4+a_2(x)y^2+a_3(x),\quad \langle C'(x,y)\rangle=0,$$
$$y\in[-H/2,H/2], \tag{40}$$

where, for convenience, $a_2(x)$ is written as (with some coefficients s and p to be found)

$$a_2(x)=\tfrac{1}{2}\big[s\bar{\Delta}_x^2\bar{C}(x)+\tfrac{1}{12}p\partial_x^4\bar{C}(x)\big]$$
$$=\tfrac{1}{2}\big[s\partial_x^2\bar{C}(x)+\tfrac{1}{12}(s+p)\partial_x^4\bar{C}(x)\big]. \tag{41}$$

Effective profile when $\Lambda=\frac{1}{4}$. When $\Lambda=\frac{1}{4}$, the last component in Eq. (6) vanishes. It follows that the correction $\delta_m\partial_x^2\bar{C}$ in Eq. (39) is produced by the term $\langle\partial_y^2C'(x,y)\rangle$, that is, with making use of $\delta_m(\Lambda=\frac{1}{4})$ in Eq. (35):

$$\Lambda=\frac{1}{4}:\ s=\delta_m,\ \bar{\Delta}_y^2C'=\delta_m\bar{\Delta}_x^2\bar{C},\ \text{with}\ \delta_m=-\frac{4t_d^{(m)}}{H}. \tag{42}$$

Figure 8 illustrates (in the first diagram) the numerical distribution $C'(x,y)$ versus y for several points along the x axis. The second diagram confirms that the parabolic fitting for $C'(x,y)$ has the curvature prescribed by Eq. (42), with $\partial_y^2C'(x,y)\approx\delta_m\partial_x^2\bar{C}(x)$ along the x axis.

The boundary-layer effect in kurtosis. Thereby, numerical simulations confirm Eq. (42) and we employ it to restore the fourth-order correction $\bar{\Delta}_x^2C'(x,y_b)$ on the profile (40) and(41) where

$$C'(x,y_b)=\tfrac{1}{12}\gamma s\partial_x^2\bar{C}(x)+O\big(\partial_x^4\bar{C}\big),\ \gamma=(H-2)(H-1). \tag{43}$$

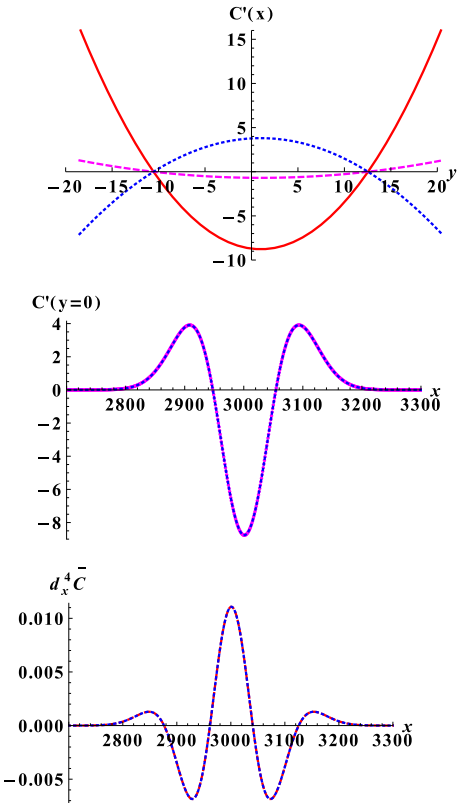

FIG. 8. Pure diffusion in straight channel is modeled with the d2Q9 BB scheme for $\Lambda = \frac{1}{4}$ and $t_c^{(m)} = \frac{1}{4}$. The first diagram displays the dependency $C'(x,y)$ in three points from center x_0, $x = \{x_0, x_0 - 50, x_0 - 100\}$ (red, magenta, blue), versus $y \in [-H/2, H/2]$, $H = 40$. The second diagram plots together numerical solution $C'(x, y = 0)$ (blue) and its predicted parabolic approximation (magenta) $C'(x, y = 0) \approx \frac{\delta_m}{24}(1 + 2H^2)\partial_x^2\bar{C}(x)$. The third diagram plots together $\partial_x^4\bar{C}(x)$ and the fourth-order correction $\partial_t\bar{C} - \Lambda^-(1 + \delta_m)\partial_x^2\bar{C}$, divided by A_3^{bb} from Eq. (39). The $C'(x,y)$ is normalized with $\max_x \partial_t\bar{C}(x,t)$ in all diagrams.

By using Eq. (43) to express $\partial_x C'(x, y_b)$ in Eq. (28), the term $\Lambda^-\langle\sum_{q=1}^{Q_m}\bar{\Delta}_x\delta g_q^- c_{qx}\rangle$ produces the fourth-order correction $\frac{1}{12}c_e\Lambda^-\gamma\delta_m s$ in the right-hand side of pure-diffusion equation, with $s = \delta_m$ according to Eq. (42). Further, following [31] but accounting for the modified second-order equation (32) in the derivation of the fourth-order correction, the A_3^{bb} in Eq. (39) obtains two additional terms. It reads as [see Eqs. (A4)–(A7) for further details]

$$\Lambda = \frac{1}{4} : A_3^{bb} = \frac{c_e\Lambda^-}{12}\gamma\delta_m^2 - \Lambda^{-3}c_e^2(1+\delta_m)^2 + \frac{c_e\Lambda^-}{12}(1+\delta_m),$$
$$\gamma\delta_m^2 = \left(1 - \frac{3}{H} + \frac{2}{H^2}\right)\left(4t_d^{(m)}\right)^2. \tag{44}$$

The third diagram in Fig. 8 confirms that the fourth-order correction, numerically estimated as $\partial_t\bar{C} - D_0(1 + \delta_m)\bar{\Delta}_x^2\bar{C}$, is in very good accordance with $A_3^{bb}\partial_x^4\bar{C}(x)$ [Eq. (44)]. The first term in Eq. (44) explains the asymptotic modification in kurtosis because it does not vanish as H increases. This result allows us to predict the absolute correction $\tilde{\mathrm{Ku}}_\star$ to truncation result $\mathrm{Ku}_\star^{(\mathrm{tr})}$ in Eq. (39):

$$\Lambda = \frac{1}{4} : \tilde{\mathrm{Ku}}_\star = \mathrm{Ku}_\star^{bb} - \mathrm{Ku}_\star^{(\mathrm{tr})},$$
$$\tilde{\mathrm{Ku}}_\star = \frac{2t_d^{(m)}\{H^{-1} - \delta_m[H^{-1} + (H-3)]\}}{c_e\Lambda^-(1+\delta_m)^2},$$
$$\tilde{\mathrm{Ku}}_\star|_{H\to\infty} = \frac{\left(4t_d^{(m)}\right)^2}{2c_e\Lambda^-}. \tag{45}$$

The result (45) tells us that $\tilde{\mathrm{Ku}}_\star$ vanishes when $t_d^{(m)} = 0$; otherwise, it remains asymptotically constant. Unlike the $\mathrm{Ku}_\star$, the $\mathrm{Ku}_\star^{bb}$ is H dependent, unless with the "rotated" mass stencil $\{t_c^{(m)} = 0, t_d^{(m)} = \frac{1}{4}\}$, where $\delta_m = -\frac{1}{H}$ and $\tilde{\mathrm{Ku}}_\star = \frac{1}{2}(c_e\Lambda^-)^{-1}$, $\forall H$. The two last diagrams in Fig. 7 demonstrate that Eq. (45) exactly (or quasi-exactly) agrees with $\mathrm{Ku}_\star^{(\mathrm{num})}$ for $H \geqslant 2$. Finally, we note that the parabolic approximation $C'(x,y)$ was sufficient to derive Eq. (45). However, for the sake of completeness, Eq. (A9) provides the coefficient p for the fourth-order polynomial distribution in Eqs. (40) and (41).

Case $\Lambda \neq \frac{1}{4}$. In this case, both the truncation and boundary-layer corrections from the last term $-(\Lambda - \frac{1}{4})\langle\sum_{q=1}^{Q_m}\bar{\Delta}_q^2 g_q^+\rangle$ in Eq. (6) should be accounted for. We are not yet aware of its exact solution and suggest the following approximate:

$$A_3^{bb} = \frac{c_e\Lambda^-}{12}\gamma s\delta_m - \Lambda^{-3}c_e^2(1+\delta_m)^2 + \frac{\Lambda^- c_e}{12}(1+\delta_m)$$
$$-\left(\Lambda - \frac{1}{4}\right)\Lambda^- c_e^2(1+\delta_m)^2$$
$$+\left(\Lambda - \frac{1}{4}\right)\frac{c_e\Lambda^-}{12}\left[1 + 6S_d\left(t_q^{(m)}\right)s + s^2\right], \tag{46}$$
$$\tilde{\mathrm{Ku}}_\star|_{H\to\infty} = \frac{\gamma s\delta_m}{2c_e\Lambda^-} = \frac{2\Lambda\left(4t_d^{(m)}\right)^2}{c_e\Lambda^-},$$
$$\text{with } s|_{H\to\infty} \approx \delta_m,\ \delta_m|_{H\to\infty} = -\frac{8\sqrt{\Lambda}t_d^{(m)}}{H}. \tag{47}$$

In this approximation, the first line is similar to the case where $\Lambda = \frac{1}{4}$ in Eq. (44), but the actual curvature in Eq. (41) is only approximate: $s \approx \delta_m$ when H is sufficiently large (in agreement with the numerical measurements when $H = 40$). The term of $(\Lambda - \frac{1}{4})$ in Eq. (47) is produced via the averaging of truncation component for Eq. (40), with $\partial_y^2 C' \approx s\partial_x^2\bar{C}$, $\partial_y^4 C' \approx s^2\partial_x^2\bar{C}$, and $\partial_x^2\partial_y^2 C' \approx s\partial_x^4\bar{C}$. The two last diagrams in Fig. 7 confirm a good asymptotic agreement between the numerical results and $\mathrm{Ku}_\star^{bb}$ [Eq. (39) with Eqs. (46) and (47)]. However, the discrepancy with this prediction is quite noticeable in the limit case $t_c^{(m)} = 0$ (last diagram) when $H < 8$ and $\Lambda \neq \frac{1}{4}$. Further work is required to understand how exactly to account for the fourth-order boundary-layer truncation correction when $\Lambda \neq \frac{1}{4}$.

Summary. The interesting result is that, unlike with $\delta_m D_0$, the absolute deviation $\tilde{\mathrm{Ku}}_\star$ from the (H-independent) truncation correction $\mathrm{Ku}_\star^{(\mathrm{tr})}$ does not converge to zero with H. Whereas $|\delta_m|$ increases linearly with $\sqrt{\Lambda}t_d^{(m)}/H$, the $\tilde{\mathrm{Ku}}_\star$ grows as $\Lambda(t_d^{(m)})^2$. The presented analysis provides the (quasi-) exact solution (45) for $\tilde{\mathrm{Ku}}_\star$ when $\Lambda = \frac{1}{4}$, $\forall H \geqslant 2$, and only asymptotic solutions (46) and (47) when $\Lambda \neq \frac{1}{4}$. The two

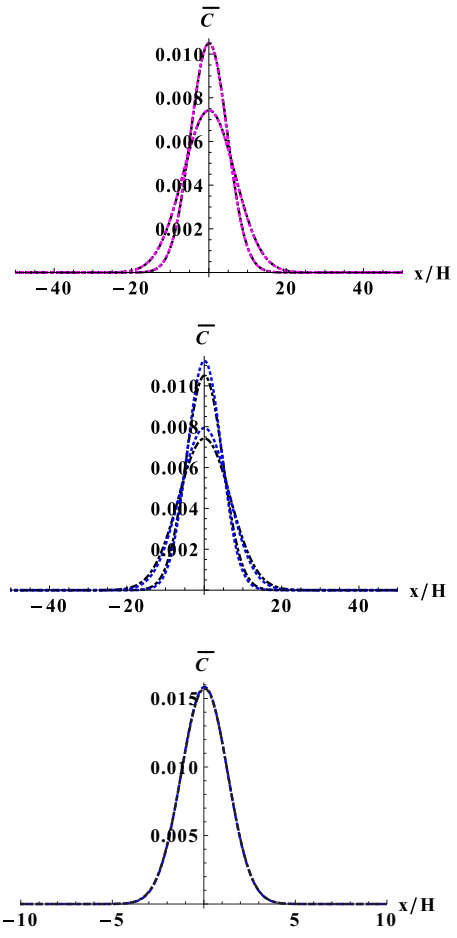

FIG. 9. The first diagram compares two pure-diffusion solutions by d2Q5 with $\mathrm{err}_D = 0$ (dotted-dashed line, black) to Gaussian distribution (dotted line, magenta) in straight channel at $t' = t/T = \{\frac{625\sqrt{3}}{96}, \frac{625\sqrt{3}}{48}\}$, $T = H^2/c_e\Lambda^-$, $c_e\Lambda^- = \frac{1}{3}\sqrt{\frac{1}{12}}$, $H = 8$. The second diagram compares profiles by d2Q5 (dotted-dashed line, black) and "rotated" d2Q9 scheme $\{t_c^{(m)} = 0, t_d^{(m)} = \frac{1}{4}\}$ (dotted line, blue) where $\mathrm{err}_D = \delta_m = -1/H$ (or -12.5%) according to Eq. (35a) for $\Lambda = \frac{1}{4}$. The last diagram compares the centered profiles of these two schemes in parabolic flow $\mathrm{Pe} \approx 9.5$. They correspond to the largest discrepancy in moments displayed in Fig. 18 (bottom row), when err_D, err(Sk), and err(Ku) differ in two schemes by about -3.5%, -130%, and 50% for $H = 20$.

first diagrams in Fig. 9 illustrate the pure-diffusion solutions with $\Lambda = \frac{1}{4}$ in straight channel of $H = 8$. In this figure, the d2Q5 BB yields $\mathrm{err}_D = 0$ and $\mathrm{Ku}_\star^{(\mathrm{tr})}[c_e = \frac{1}{3}, (\Lambda^-)^2 = \frac{1}{12}] = 2\sqrt{3}$ [Eq. (38)]. The "rotated" d2Q5 BB scheme yields $\mathrm{err}_D = \mathrm{err}_D^{(bb)} = -1/H$ and $\mathrm{err(Ku)} = \mathrm{Ku}_\star^{bb}/\mathrm{Ku}_\star^{(\mathrm{tr})} - 1 = \frac{3}{2}$ [Eq. (45)]. The (relatively small) boundary-layer decrease of the diffusion coefficient is clearly observable. At the same time, the (relatively large) increase in $\mathrm{Ku}_\star$ is not evident by visual inspection. We further address this point in the presence of the advection velocity in Sec. V A.

C. Diffusion-coefficient correction due to weight family $\{t_q^{(u)}\}$

The term of the $\{t_q^{(u)}\}$ weight family removes the second-order numerical diffusion of the scheme, entirely in pipe flows at least [31]. When its free-tunable coordinate value is $t_c^{(u)} \neq \frac{1}{2}$, the bounce back further modifies the apparent diffusion coefficient in Eq. (7) because of the diagonal-link equilibrium value $\frac{1}{d}t_d^{(u)}U_x^2C$ in Eq. (2). In plug flow, this term is a linkwise constant and its correction to diffusion coefficient can be obtained similarly as for the mass term $t_d^{(m)}c_eC$ in Eq. (27):

$$U_x = \mathrm{const}: \ \mathrm{err}_D^{(bb,u^2)}\big(t_c^{(u)}, \Lambda, \mathcal{L}\big) = \frac{U_x^2}{dc_e(1+k_T)}\big(1 - 2t_c^{(u)}\big)F^{(m)}(\Lambda, \mathcal{L}). \tag{48}$$

In variable velocity field, the U_x^2 term varies along the link and one may expect to get the functional form $F^{(m)}(\Lambda, \mathcal{L})$ of the diffusion term only for $\Lambda = \frac{1}{4}$, replacing U_x^2 by *the boundary value* $U_x^2(\boldsymbol{r}_\mathrm{b})$. This result was confirmed in straight channel [69]. Since the stable velocity amplitude $U^{2\max}$ is usually smaller than dc_e (with the necessary stability condition [21] $U^{2\max} < \frac{d}{d-1}c_e$ on the coordinate velocity stencil), and since $U_x^2(\boldsymbol{r}_\mathrm{b}) \ll U^{2\max}$, the $\mathrm{err}_D^{(bb,u^2)}$ is small against the first-order diffusion-coefficient correction $\mathrm{err}_D^{(bb)}$. In all computations below, $t_c^{(u)} = \frac{1}{2}$ so that $\mathrm{err}_D^{(bb)}(t_c^{(u)})$ vanishes.

D. Bounce-back velocity correction $\mathrm{err}_U^{(bb)}$

We examine the apparent velocity in Eq. (7). Its effective value $\mathcal{U}^{(\mathrm{num})} = \frac{\mu_1(t+\delta_t) - \mu_1(t)}{\delta_t}$ is derived from the first raw moment and compared to the prescribed mean velocity $\mathcal{U}$. The computations in straight channel and cylindrical capillary are run with the plug flow $U_x = \mathcal{U}$ (c field) and Poiseuille profile (p field). We first observe that $\mathcal{U}^{(\mathrm{num})}$ is equal to the arithmetical-mean value $\mathcal{U}^{(\mathrm{sum})} = \langle U_x \rangle$ in these four configurations when the coordinate-velocity weight is $t_c^{(a)} = \frac{1}{2}$:

$$t_c^{(a)} = \tfrac{1}{2} : \mathcal{U}^{(\mathrm{num})} = \mathcal{U}^{(\mathrm{sum})}. \tag{49}$$

In particular, this result is valid with the d2Q5 and d3Q7 schemes. This property takes also place with the d2Q9 SNL in straight channel, for any velocity weight. In plug flow $\mathcal{U}^{(\mathrm{sum})} \equiv \mathcal{U}$. In straight Poiseuille flow $\mathcal{U}^{(\mathrm{sum})} = \mathcal{U}[1 + 1/(2H^2)]$. The relative velocity error $\mathrm{err}_U^{(\mathrm{sum})} = \mathcal{U}^{(\mathrm{sum})}/\mathcal{U} - 1$ is tabulated in Table I for the parabolic profile imposed in cylindrical capillary. It is interesting that its decay is not monotonous with the increase of radius R. When $t_c^{(a)} \neq \frac{1}{2}$, Fig. 10 demonstrates

TABLE I. This table provides relative summation correction $\mathrm{err}_U^{(\mathrm{sum})}(R) = \mathcal{U}^{(\mathrm{sum})}/\mathcal{U} - 1$ computed on the parabolic velocity profile imposed in the discretized circular shape. The data are in percents.

R	5	10	20	40	80	160
$\mathrm{err}_U^{(\mathrm{sum})}(\%)$	-1.6	-0.54	-0.58	5.3×10^{-2}	-8.9×10^{-3}	-3.4×10^{-2}

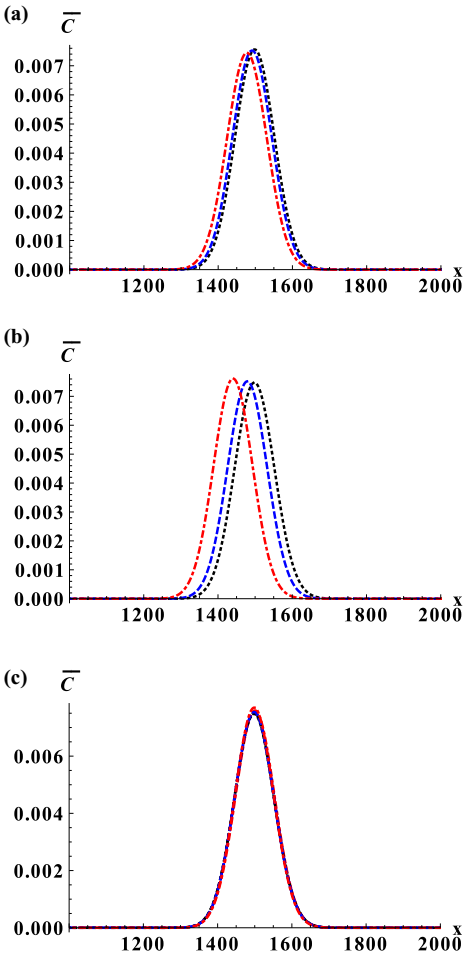

FIG. 10. The two first diagrams (a) $\Lambda = \frac{1}{12}$ and (b) $\Lambda = \frac{1}{4}$ illustrate the bounce-back retardation effect in cylindrical capillary of $R = 5$ due to velocity weight, when $t_c^{(a)} = \{\frac{1}{2}, \frac{1}{3}, 0\}$ [dotted line (black), dashed line (blue), dotted-dashed line (red)]. The third diagram (c) displays together for $\Lambda = \frac{1}{12}$ and $\frac{1}{4}$, and for three weights, the profiles obtained with the double-Λ BB scheme. The simulations are run at Pe ≈ 9.5 starting from the uniform plume $C(x = x_0, r) = 1$ and output after 10^4 time steps; the mass weight $t_c^{(m)} = \frac{1}{3}$.

that the advection front progressively slows in a pipe of $R = 5$ from $t_c^{(a)} = \frac{1}{2}$ to $t_c^{(a)} = \{\frac{1}{3}, 0\}$. This effect is much more pronounced for $\Lambda = \frac{1}{4}$ (second diagram) than for $\Lambda = \frac{1}{12}$ (first diagram). This retardation effect due to velocity weight is dramatic in plug flow, as illustrated for channel [69] and explained below. Thereby, the entire relative-velocity error becomes composed of the two components (i) summation $\mathrm{err}_U^{(\mathrm{sum})}$ and (ii) boundary layer $\mathrm{err}_U^{(bb)}$:

$$\mathrm{err}_U = \frac{\mathcal{U}^{(\mathrm{num})}}{\mathcal{U}} - 1 = \mathrm{err}_U^{(\mathrm{sum})} + \mathrm{err}_U^{(bb)}. \tag{50}$$

In both c field and p field, $\mathrm{err}_U^{(bb)}$ is independent of the velocity amplitude, c_e and Λ^-, and hence $\mathrm{err}_U^{(bb)}$ is Pe independent. Also, the choice of the two other weight families does not impact $\mathrm{err}_U^{(bb)}$ but $|\mathrm{err}_U^{(bb)}|$ increases linearly with the diagonal velocity weight $t_d^{(a)}$. This is illustrated in the two first diagrams in Fig. 11. Similar as for diffusion coefficient in Eq. (35a), we

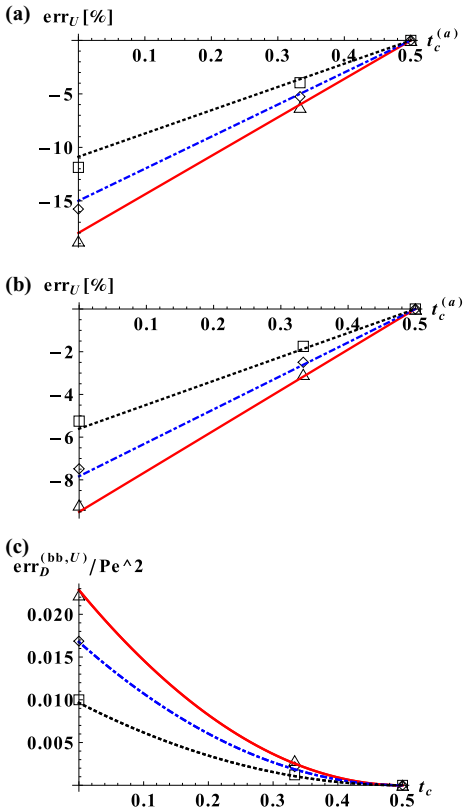

FIG. 11. The two first diagrams (a) $R = 5$ and (b) $R = 10$ compare numerical results (symbols) for the relative mean-velocity error err_U in plug flow prescribed in cylindrical capillary to its theoretical prediction $\mathrm{err}_U^{(bb)}(t_c^{(a)}, \Lambda, R)$ (straight lines) given by Eq. (55), with $\mathrm{err}_U(t_c^{(a)} = \frac{1}{2}) = 0$. The last diagram (c) compares numerical results for $\mathrm{err}_D/\mathrm{Pe}^2$ (symbols) to theoretical prediction $\mathrm{err}_D^{(bb,U)}(t_c^{(a)}, \Lambda, R)/\mathrm{Pe}^2$ (lines) for boundary-layer relative dispersion correction given by Eq. (60) when $R = 10$ (data are in percents, $t_c = t_c^{(a)}$). The results are plotted for uniform distribution $\Lambda = \{\frac{1}{12}, \frac{1}{6}, \frac{1}{4}\}$ [dotted line (black), dotted-dashed line (blue), solid line (red)].

look for $\mathrm{err}_U^{(bb)}$ in the form

$$\mathrm{err}_U^{(bb)}\big(t_c^{(a)}, \Lambda, \mathcal{L}\big) = \langle \delta U(r) \rangle = \delta_a,$$
$$\delta_a\big(t_c^{(a)}, \Lambda, \mathcal{L}\big) = F^{(a)}(\Lambda, \mathcal{L})\big(1 - 2t_c^{(a)}\big). \tag{51}$$

In this relation, $\delta U(r)\mathcal{U}$ is the boundary-layer velocity profile; it is superposed with the advection profile. We construct $\delta U(r)$ in plug and parabolic profiles and derive dependency $F^{(a)}(\Lambda, \mathcal{L})$. This will tell us that in c field, the dependency $F^{(a)}(\Lambda, \mathcal{L})$ is the same as $F^{(m)}(\Lambda, \mathcal{L})$ in Eq. (27) but it is different in p field.

1. Constant velocity field

When the diagonal velocity weight $t_d^{(a)} \neq 0$, the diagonal links in Eq. (2b) obtain nonzero components $e_q^-(x,t) = t_d^{(a)} U_x C(x,t) c_{qx}$. In plug flow, this situation is very similar to the restriction of the tangential diffusion flux in Sec. III A because the bounce-back closure relation (26) tries to enforce the advective flux to zero. We suggest that the boundary-layer correction $\{\delta g_q^{\pm}\}$ accommodates this deficiency via the advective-flux correction $\delta U(r)\mathcal{U}\partial_x \bar{C}(x,t)$. The leading-order nonequilibrium boundary-layer correction is looked for in the

TABLE II. This table gives parameters for four numerical experiments with the parabolic profile imposed in cylindrical capillary of radius $R = 5 \times 2^n$, $n = 0,1,2$. The molecular diffusion coefficient is $D_0 = c_e\Lambda^-$, $\mathrm{Pe} = \frac{2R|\mathcal{U}}{D_0}$. The mean velocity $\mathcal{U} = |U|^{\max}/2$ is set with $|U|^{\max}(n=0) = \sqrt{c_e}|_{c_e=1/30} = 2 \times 0.091287$. The $\mathrm{Sk}_\star$ and $\mathrm{Ku}_\star$ apply their solutions [30]. These two coefficients are equal to zero in Gaussian distribution.

Expt.	$\mathrm{Pe} = \frac{2R\mathcal{U}}{c_e\Lambda^-}$	$\mathcal{U}$	c_e	$(\Lambda^-)^2$	$k_T^{(c)} = \frac{\mathrm{Pe}^2}{192}$	$\mathrm{Sk}_\star = \mathrm{Sk} \times \sqrt{t\mathcal{U}/R}$	$\mathrm{Ku}_\star = \mathrm{Ku} \times t\mathcal{U}/R$
I	2.47461	$0.091287/2^n$	$\frac{1}{3}$	$\sqrt{\frac{3}{2}}$	3.19×10^{-2}	1.48×10^{-3}	-2.6×10^{-4}
II	9.48682	$0.091287/2^n$	$\frac{1}{3}$	$\frac{1}{12}$	4.687×10^{-1}	9.62×10^{-2}	-1.06×10^{-1}
III	24.74612	$0.091287/2^n$	$\frac{1}{30}$	$\sqrt{\frac{3}{2}}$	3.19	5.72×10^{-1}	-1.58
IV	94.8682	$0.091287/2^n$	$\frac{1}{30}$	$\frac{1}{12}$	46.87	1.63	-9.99

form [cf. Eq. (28)]

$$\delta g_q^+(\boldsymbol{r}_n) = \mathcal{K}_1 P(n)\bar{C}(x)c_{qx}c_{q\alpha},$$
$$\delta g_q^-(\boldsymbol{r}_n) = \frac{\sqrt{\Lambda}}{\Lambda^-}\mathcal{K}_1 M(n)\bar{C}(x)c_{qx}c_{q\alpha}^2,$$
$$\alpha = \{y,z\}, n = 0,\dots,N. \tag{52}$$

After substitution of $e_q^-(x,t) = t_d^{(a)}U_x C(x,t)c_{qx}$, $G_q^\pm = 0$, and Eq. (52) into Eq. (26), the suitable combination of the diagonal links gives closure condition in the form

$$U_x = \text{const} : \bar{C}(x,t)\left[2t_d^{(a)}U_x(\boldsymbol{r}_N) + \mathcal{K}_1(1-2\sqrt{\Lambda}M(N)\right] = 0,$$
$$\text{then } \mathcal{K}_1 = -\frac{2t_d^{(a)}U_x(\boldsymbol{r}_N)}{1-2\sqrt{\Lambda}M(N)}. \tag{53}$$

The term $-\Lambda^-\sum_{q=1}^{Q_m}\bar{\Delta}_x\delta g_q^- c_{qx}$ then modifies the convective flux in the left-hand side of the modeled advection-diffusion equation by the quantity $\delta U(n)\mathcal{U}\partial_x\bar{C}(x,t)$, where the relative velocity correction $\delta U(n)$ reads as

$$U_x = \text{const} : \delta U(n) = \frac{2\sqrt{\Lambda}\left(1-2t_c^{(a)}\right)M(n)}{1-2\sqrt{\Lambda}M(N)}\frac{U_x(\boldsymbol{r}_N)}{\mathcal{U}},$$
$$\text{with } U_x(\boldsymbol{r}_N) \equiv \mathcal{U}. \tag{54}$$

The mean velocity $\mathcal{U}$ obtains correction $\delta_a\mathcal{U}$ where δ_a reads as

$$\delta_a\left(t_c^{(a)},\Lambda,\mathcal{L}\right) = \langle\delta U(n)\rangle = F^{(a)}(\Lambda,\mathcal{L})\left(1-2t_c^{(a)}\right)\frac{U_x(\boldsymbol{r}_N)}{\mathcal{U}},$$
$$F^{(a)}(\Lambda,\mathcal{L}) = -\frac{2\sqrt{\Lambda}}{l}\Psi(\Lambda,\mathcal{L}), \tag{55a}$$

$$\delta_a\left(t_c^{(a)},\Lambda=\frac{1}{4},\mathcal{L}\right) = -\frac{\left(1-2t_c^{(a)}\right)}{l}\frac{U_x(\boldsymbol{r}_N)}{\mathcal{U}}, \tag{55b}$$
$$\delta_a|_{\mathcal{L}\to\infty} = -\frac{2\sqrt{\Lambda}\left(1-2t_c^{(a)}\right)}{l}\frac{U_x(\boldsymbol{r}_N)}{\mathcal{U}}, \forall\,\Lambda. \tag{55c}$$

In c field, $U_x(\boldsymbol{r}_N) = \mathcal{U}$ and the relative velocity and diffusion-coefficient corrections coincide: $\delta_a(t_c^{(a)}) = \delta_m(t_c^{(m)})$ [cf. Eqs. (35) and (55)]. They are set by resolution and Λ alone. In straight channel [69], $\Psi(\Lambda,\mathcal{L})$ is given by Eq. (36a) and $\delta_a\mathcal{U} = \mathcal{U}^{(\mathrm{num})} - \mathcal{U}$ exactly agrees with the numerical results. In cylindrical capillary, $\langle\delta U(n)\rangle$ is computed with Eq. (34) and $\Psi(\Lambda,\mathcal{L})$ is given by Eq. (36b). Figure 11 compares the numerical result $\mathrm{err}_U^{(\mathrm{num})}$ to the predicted value $\mathrm{err}_U^{(bb)}$ for plug flow imposed in cylindrical capillary of $R = 5$ and 10. These results are exactly the same as for the diffusion coefficient in Fig. 4 (replacing $t_c^{(m)}$ by $t_c^{(a)}$ and $\mathrm{err}_D^{(bb)}$ by $\mathrm{err}_U^{(bb)}$). The constructed dependency $\delta_a(\Lambda,R)$ is only approximate in a capillary. Its quality improves when the geometrical discretization error diminishes. Figure 4 is computed with the parameters of Expt. II from Table II but $\mathrm{err}_U(t_c^{(a)},\Lambda,R)$ takes the same value for any velocity amplitude and Péclet number.

2. *Parabolic velocity profile*

We extend the straight channel solution [69] to cylindrical capillary. In the parabolic profile $U_x(r)$, the first- and second-order velocity gradients should be taken into account. The velocity deviation $\mathcal{U}\delta U(n)$ is decomposed as the sum of two components with the help of Eqs. (24) and (25):

$$\mathcal{U}\delta U(n) = -N_d[\sqrt{\Lambda}\mathcal{K}_1 M(n) + \mathcal{K}_2\mathcal{P}(n)], \quad n = 0, \quad 1,\dots,R-1,$$
$$\text{with } \mathcal{K}_1 = -\frac{2t_d^{(a)}}{1-2\sqrt{\Lambda}M(N)}\left[U_x - \frac{1}{2}|\partial_r U_x(r)| + \Lambda\partial_r^2 U_x(r)\right]\Big|_{\boldsymbol{r}_b=\{\boldsymbol{r}_0,\boldsymbol{r}_N\}}, \tag{56}$$
$$\mathcal{K}_2 = \frac{2t_d^{(a)}\Lambda}{1-2\sqrt{\Lambda}\mathcal{M}(N)}\left[|\partial_r U_x(r)| - \frac{1}{2}\partial_r^2 U_x(r)\right]\Big|_{\boldsymbol{r}_b=\{\boldsymbol{r}_0,\boldsymbol{r}_N\}}.$$

In this relation, $\mathcal{K}_1$ is derived from the difference of suitable linear combinations of closure relations with $c_{qx} = \pm 1$, similarly to what has been described for constant velocity. With the symmetry argument, the $\mathcal{K}_2$ is derived from their sum. Further details can be found in Sec. IV B 3 (by restricting them to the space uniform Λ). When the velocity variation vanishes, Eq. (56) reduces to Eq. (54) in c field. The mean velocity $\mathcal{U}$ obtains correction $\delta_a\mathcal{U}$ where the relative correction $\delta_a = \langle\delta U(n)\rangle$ reads as in d3Q15

scheme

$$\delta_a\left(t_c^{(a)},\Lambda,\mathcal{L}\right)=-\frac{2\sqrt{\Lambda}\left(1-2t_c^{(a)}\right)}{\mathcal{U}l}\left[\left(U_x-\frac{1}{2}|\partial_r U_x|+\Lambda\partial_r^2 U_x\right)\Big|_{\boldsymbol{r}_\mathrm{b}}\Psi(\Lambda,\mathcal{L})+\sqrt{\Lambda}\left(|\partial_r U_x|-\frac{1}{2}\partial_r^2 U_x\right)\Big|_{\boldsymbol{r}_\mathrm{b}}\phi(\Lambda,\mathcal{L})\right], \tag{57a}$$

$$\delta_a\left(t_c^{(a)},\Lambda=\frac{1}{4},\mathcal{L}\right)=-\frac{\left(1-2t_c^{(a)}\right)}{l}\frac{U_x(\boldsymbol{r}_\mathrm{b})}{\mathcal{U}},\ \boldsymbol{r}_\mathrm{b}=\{\boldsymbol{r}_0,\boldsymbol{r}_N\}. \tag{57b}$$

These equations can be computed with the help of Eq. (36b). Since $\Psi(\Lambda,\mathcal{L})|_{\Lambda=\frac{1}{4}}=\phi(\Lambda,\mathcal{L})|_{\Lambda=\frac{1}{4}}=1$, the terms of velocity gradients vanish in Eq. (57a) for $\Lambda=\frac{1}{4}$ and the solution takes the same form as in Eq. (55b) but here $\frac{U_x(\boldsymbol{r}_\mathrm{b})}{\mathcal{U}}\ll 1$. The result (57) reduces to the straight channel solution [69] by replacing $\partial_r U_x(r)$ by $\partial_y U_x(y)$ and $\partial_r^2 U_x(r)$ by $\partial_y^2 U_x(y)$, together with Eq. (36a). This solution is demonstrated [69] to be exact for a straight channel. Figure 12 compares the numerical results for $\mathrm{err}_U^{(bb)}=\mathrm{err}_U-\mathrm{err}_U^{(\mathrm{sum})}$ to the theoretical estimate (57) in a capillary, with $\mathrm{err}_U^{(\mathrm{sum})}$ from Table I. The advection velocity slows down linearly when $t_d^{(a)}$ increases. This effect reduces with Λ in accord with the two first diagrams in Fig. 10. Again, the estimate given by Eq. (57) is only approximate in a capillary; its accuracy is better for $R=10$ than for $R=20$ where the discretization effect is larger (cf. Table I).

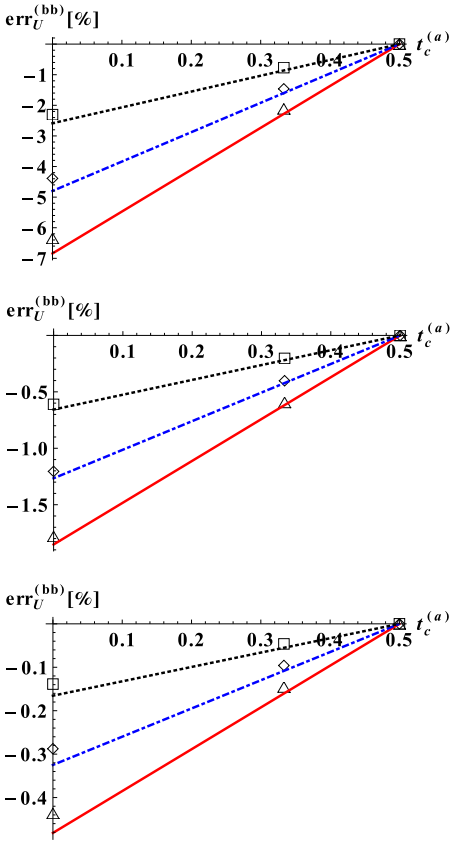

FIG. 12. This figure quantifies bounce-back retardation of the Poiseuille profile in cylindrical capillary of $R=\{5,10,20\}$ (from the top to the bottom). The numerical values $\mathrm{err}_U-\mathrm{err}_U^{(\mathrm{sum})}$ in Eq. (50) (symbols) are compared to its theoretical prediction $\mathrm{err}_U^{(bb)}(t_c^{(a)},\Lambda,R)$ from Eq. (57) (straight lines) The results are plotted for uniform distribution $\Lambda=\{\frac{1}{12},\frac{1}{6},\frac{1}{4}\}$ [dotted line (black), dotted-dashed line (blue), solid line (red)].

Finally, it should be said that the velocity retardation is less significant in parabolic flow than in plug flow (cf. two first diagrams in Figs. 11 and 12) because $\mathrm{err}_U^{(bb)}$ (approximately) scales in the proportion to $U_x(\boldsymbol{r}_\mathrm{b})/\mathcal{U}$. Whereas $U_x(\boldsymbol{r}_\mathrm{b})=\mathcal{U}$ in c field, $U_x(\boldsymbol{r}_\mathrm{b})$ is much smaller than $\mathcal{U}$ in p field. We underline that in the two cases, the relative velocity error is independent of the velocity amplitude and Pe.

E. Bounce-back dispersion correction $\mathrm{err}_D^{(bb,U)}$

In straight channel, the transverse gradient in the boundary-layer velocity component $\delta U(y)\mathcal{U}$ creates numerical dispersion, accurately predicted [69] with the help of the Taylor argument [24]. The predicted dispersion coefficient $k_T D_0$ in Eq. (7) becomes modified by the quantity $k_T^{(bb)}D_0$. Its relative contribution is quantified via $\mathrm{err}_D^{(bb,U)}(t_c^{(a)},\Lambda,\mathcal{L})$:

$$\mathrm{err}_D^{(bb,U)}\left(t_c^{(a)},\Lambda,\mathcal{L}\right)=\frac{k_T^{(bb)}\left(t_c^{(a)},\Lambda,\mathcal{L}\right)}{1+k_T}. \tag{58}$$

In straight channel [69], $k_T^{(bb)}$ is built in c field and p field, in good agreement with the numerical results.

In cylindrical capillary, we look for the correction $C'(x,r,t)$ to the mean concentration $\bar{C}(x,t)$ which obeys the Taylor ansatz [24] in the form

$$\begin{aligned}&D_0\Delta_r C'(x,r)\approx[U'(r)+\delta U'(r)]\partial_x\bar{C}(x,t),\\ &\text{where }\Delta_r C'(x,r)=\frac{1}{r}\partial_r(r\partial_r C'(x,r)),\\ &U'(r)=U_x(r)-\mathcal{U},\ \delta U'(r)=\mathcal{U}[\delta U(r)-\delta_a].\end{aligned} \tag{59}$$

In this equation, $U'(r)$ is the difference between the prescribed velocity profile and its mean value $\mathcal{U}$, while $\delta U'(r)$ is the deviation of the boundary-layer profile from its mean value $\delta_a\mathcal{U}$.

In c field, $U'(r)\equiv 0$ and $C'(x,r,t)=\frac{\gamma(r)}{D_0}\partial_x\bar{C}(x,t)$, where $\gamma(r)$ solves $\Delta_r\gamma(r)=\delta U'(r)$ subject to the normalization condition $\langle C'(x,r)\rangle=0$. The averaged-flux component $\langle\delta U'(r)\partial_x C'(x,r)\rangle$ then modifies the diffusion form by quantity $D_0 k_T^{(bb)}\partial_x^2\bar{C}$, with

$$U_x=\mathrm{const}:\ k_T^{(bb)}\approx-\frac{\langle\delta U'(r)\gamma(r)\rangle}{D_0^2},\ \Delta_r\gamma(r)=\delta U'(r). \tag{60}$$

In this relation, $\delta U'(r)=\mathcal{U}[\delta U(n)-\delta_a]$ is given by Eqs. (54) and (55a) and, hence, $\delta U'(r)\propto(1-2t_c^{(a)})\mathcal{U}/\mathcal{L}$. In

Eq. (58), since $k_T = 0$ in plug flow, $\mathrm{err}_D^{(bb,U)} = k_T^{(bb)} \propto (1 - 2t_c^{(a)})^2 \mathrm{Pe}^2/\mathcal{L}^2$. Since we are only aware of $\delta U'(r)$ along the coordinate α axis, $\alpha = \{y,z\}$, solution of $\Delta_r \gamma(r) = \delta U'(r)$ is built approximately, in the form $\gamma(n) = \gamma^{(1)}(n) + \gamma^{(2)}(n)$ with

$$\partial_\alpha^2 \gamma^{(1)}(n) = \delta U(n)\mathcal{U}, \quad \gamma^{(2)}(n) = -\frac{r^2}{4}\delta_a \mathcal{U},$$
$$r(n) = R - n - \frac{1}{2}, \quad n = 0,1,\dots R-1, \alpha = \{y,z\}. \tag{61}$$

Recall that $\delta U(n)$ in Eqs. (54) and (56) presents the linear combination of functions $k^{\pm n}$; hence, $\gamma^{(1)}(n)$ is built as the linear combination of functions $\gamma'(n) = \frac{k}{(k-1)^2}k^{\pm n}$: they solve $\partial_\alpha^2 \gamma'(n) = k^{\pm n}$. This function has the same form as the channel solution.

Figure 11 compares numerical results for $\mathrm{err}_D = D^{(\mathrm{num})}/D_0 - 1$ to predicted boundary-layer dispersion in Eq. (58) ($k_T = 0$), with the help of Eqs. (60) and (61). The simulations are run with the constant-velocity profile prescribed in the cylindrical capillary; the parameters correspond to Expt. III from Table II. The mass weight $t_c^{(m)}$ is set equal to $\frac{1}{2}$, hence, the boundary-layer diffusion-coefficient correction in Eq. (27) vanishes, $\mathrm{err}_D^{(bb)} = 0$. Then, in agreement with the predictions, $\mathrm{err}_D^{(\mathrm{num})} = 0$ for $t_c^{(a)} = \frac{1}{2}$. When $t_c^{(a)}$ decreases towards 0 and hence $t_d^{(a)}$ increases to $\frac{1}{4}$, the $\mathrm{err}_D^{(bb,U)}$ increases rapidly, as $t_d^{(a)2}$. The numerical results follow well the constructed dispersion estimate when the velocity estimate is accurate enough ($R = 10$ here).

In Poiseuille profile $U_x(r)$ in cylindrical capillary, the boundary-layer dispersion results from the superposition of $U_x(r)$ with the boundary-layer profile $\delta U(r)$. Let $\Delta_r \alpha(r) = U'(r)$, then $\langle U'(r)\alpha(r)\rangle$ produces Taylor-dispersion coefficient $k_T^{(c)}$ (see [24,31]). In turn, $k_T^{(bb)}$ is derived from the superposition of two velocity fields:

$$k_T^{(bb)} \approx -\frac{\langle [U'(r) + \delta U'(r)]\gamma(r)\rangle + \langle \delta U'(r)\alpha(r)\rangle}{D_0^2},$$
$$\alpha(r) = \frac{\mathcal{U}}{16}\left(r^2 - \frac{r^4}{2R^2}\right). \tag{62}$$

In this relation, $\gamma(r)$ is constructed similar to Eq. (61), with $\delta U'(r)$ being the difference between the boundary-layer velocity $\mathcal{U}\delta U(n)$ from Eq. (56) and its mean value $\delta_a \mathcal{U}$ from Eq. (55). In straight channel, the constructed boundary-layer dispersion estimate [69] is exemplified by closed-form result for $\Lambda = \frac{1}{4}$. The dispersion estimate [69] is employed for channel in Sec. V A; Eq. (62) produces boundary-layer dispersion estimate $\mathrm{err}_D^{(bb,U)}$ in Sec. V B. We note that the construction of the boundary-layer numerical dispersion with Eq. (62) can be easily extended from the parabolic to any other pipe flow.

In summary, we emphasize that $k_T^{(bb)}$ approximately scales as $(1 - 2t_c^{(a)})^2 \mathrm{Pe}^2/\mathcal{L}^2$ and its relative contribution $\mathrm{err}_D^{(bb,U)}$ becomes asymptotically constant as Pe increases in parabolic profile where $k_T \propto \mathrm{Pe}^2$, whereas it grows as Pe^2 in plug flow. In turn, the relative diffusion-coefficient correction $\mathrm{err}_D^{(bb)}(t_c^{(m)})$ becomes negligible against the $\mathrm{err}_D^{(bb,U)}(t_c^{(a)})$ as Pe increases since $\mathrm{err}_D^{(bb)}(t_c^{(m)})$ scales as Pe^{-2}. It follows that the largest impact from $\mathrm{err}_D^{(bb)}(t_c^{(m)})$ is expected in pure diffusion and for small Péclet numbers, while $\mathrm{err}_D^{(bb,U)}(t_c^{(a)})$ should be reduced in computations with high Pe. This is achieved with the double-Λ strategy considered in Sec. IV.

IV. DOUBLE-Λ BOUNCE-BACK SCHEME

The boundary-layer nonequilibrium corrections are excited by the BB closure relation (26) in boundary nodes. The idea is to apply the bounce-back rule (15) in combination with the TRT operator (1) where the two distinguished positive values are prescribed for free collision combination $\Lambda = \Lambda^-\Lambda^+$, with Λ_v in bulk nodes and Λ_b in boundary nodes. This situation is sketched in Fig. 13. The rationale behind this is that the amplitude of the bounce-back primary effects, such as the diffusion-coefficient relative correction $\mathrm{err}_D^{(bb)} = \delta_m(t_c^{(m)},\Lambda,\mathcal{L})$ [Eq. (27) with Eq. (35)], or the mean-velocity relative correction $\mathrm{err}_U^{(bb)} = \delta_a(t_c^{(a)},\Lambda,\mathcal{L})$ [Eq. (50) with Eqs. (55) and (57)], can be controlled by the couple $\{\Lambda_v,\Lambda_b\}$ in given geometry. The preliminary results [69] confirm that the spurious modifications in transport coefficients in Eq. (7) can be attenuated with the help of sufficiently small value Λ_b, e.g., $\Lambda_b \approx \frac{1}{4} \times 10^{-2}$ is employed [69]. Our purpose is to analytically construct the most efficient functional form $\Lambda_b(\Lambda_v,\mathcal{L})$ in straight channel and cylindrical capillary.

The starting point (Sec. IV A) is the generic (implicit) steady-state interface conditions of the TRT scheme. With their help, the bounce-back corrections are exactly constructed in a straight channel in the presence of the double-Λ distribution. This concerns the effective velocity in plug flow (Sec. IV B 1), the effective diffusion coefficient (Sec. IV B 2), and the mean velocity in parabolic profile (Sec. IV B 3). The specific dependencies $\Lambda_b(\Lambda_v,H)$ may vanish the bounce-back corrections but they should obey the positivity condition $\Lambda_b > 0$. The similar but the approximate analysis (Sec. IV C) is performed in a cylindrical capillary. The positive-valued dependencies are compared for the parabolic profiles in a channel and a capillary.

A. Interface

In Sec. III, the nonequilibrium boundary-layer correction $\{\delta g_q^\pm\}$ has been constructed from the closure relation of the bounce-back rule assuming that Λ is uniform. We aim to extend this solution to double-Λ (discontinuous) distribution. It has been demonstrated [41] that any steady-state population

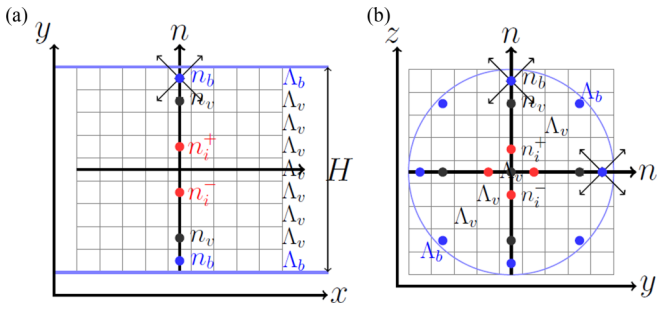

FIG. 13. This figure illustrates construction of the double-Λ BB scheme in (a) channel and (b) circular shape, where Λ_v is set in all bulk nodes while Λ_b is prescribed in all boundary nodes. The bounce-back closure conditions are set at $n = n_b$, the interface conditions are set for $n = \{n_b, n_v\}$, and the axis-symmetry condition is set for $n = \{n_i^+, n_i^-\}$.

solution of the TRT scheme implicitly obeys two generic interface conditions per link connecting any two grid neighbors $\boldsymbol{r}$ and $\boldsymbol{r}+\boldsymbol{c}_q$, with $\boldsymbol{c}_{\bar{q}}=-\boldsymbol{c}_q$:

$$S_q(\boldsymbol{r})=S_{\bar{q}}(\boldsymbol{r}+\boldsymbol{c}_q),\ S_q(\boldsymbol{r})=\left[e_q^+ +\tfrac{1}{2}g_q^- -\Lambda^+ g_q^+\right](\boldsymbol{r}),\forall\, e_q^+ \tag{63a}$$

$$V_q(\boldsymbol{r})=-V_{\bar{q}}(\boldsymbol{r}+\boldsymbol{c}_q),\ V_q(\boldsymbol{r})=\left[e_q^- +\tfrac{1}{2}g_q^+ -\Lambda^- g_q^-\right](\boldsymbol{r}),\forall\, e_q^-. \tag{63b}$$

These two closure conditions are simple linear combinations of Eq. (1): they apply the local relaxation eigenfunctions, as $\Lambda^{\pm}(\boldsymbol{r})$ and $\Lambda^{\pm}(\boldsymbol{r}+\boldsymbol{c}_q)$. The two relations are valid for either continuous or discontinuous distribution $\Lambda^{\pm}(\boldsymbol{r})$. Assume uniform distribution $c_e(\boldsymbol{r})\equiv c_e$ (this condition is required [29] for continuity of the concentration C). When the diffusion coefficient D_0 is homogeneous, $\Lambda^-(\boldsymbol{r})=D_0/c_e(\boldsymbol{r})$ is continuous. In double-Λ scheme, $\Lambda^+(\boldsymbol{r})$ takes the two separate values: $\Lambda_v^+=\Lambda_v/\Lambda^-$ in bulk and $\Lambda_b^+=\Lambda_b/\Lambda^-$ in boundary nodes. The interface conditions (63) have been applied in the presence of discontinuous collision components in stratified advection-diffusion [22,41] and hydrodynamic [41,82] configurations. The idea of this work is to apply Eqs. (63) to the perturbed nonequilibrium solution $\{g_q^{\pm}=G_q^{\pm}+\delta g_q^{\pm}\}$ because, by construction, Eqs. (63) should remain valid for any steady-state solution of the TRT scheme (see [41] for including of sources).

B. Straight channel

We consider plug flow $U_x\equiv\mathcal{U}$ (c field) and Poiseuille profile $U_x(y)$ (p field) in straight channel $y\in[-H/2,H/2]$. The bounce back produces the relative velocity correction $\delta_a(t_c^{(a)},\Lambda,H)=F^{(a)}(\Lambda,H)(1-2t_c^{(a)})$ given by Eq. (55) in c field and Eq. (57) in p field. We first extend these solutions to the double-Λ BB scheme with the help of Eqs. (63) and then examine whether it exists a specific dependency $\Lambda_b(\Lambda_v,H)$ where $\delta_a(t_c^{(a)},\Lambda_v,\Lambda_b,H)$ vanishes for any velocity weight $t_c^{(a)}$.

1. Constant velocity profile

Let the grid nodes along the normal y direction be numbered as $n=\{n_b=0,n_v=1,\ldots,n_i^-,n_i^+,\ldots,n_v=H-2,n_b=H-1\}$, with the symmetry axis located between n_i^- and n_i^+ (see Fig. 13). Hereafter, "v" and "b" denote bulk and boundary nodes, respectively. The double-Λ strategy presents the three-layered stratified configuration; it is composed of two equivalent (boundary) regions of unit width which are separated by the bulk region. The implicit interface conditions (63) take place between the (bottom) nodes $n_b=0$ and $n_v=1$, and between the (top) nodes $n_v=H-2$ and $n_b=H-1$. We look for the "stratified" correction $\{\delta g_q^{\pm}(n)\}$ in the form (52) with two constants per layer, say A and B:

$$\begin{aligned}
&\delta g_q^+(n)=(Ak^n+Bk^{-n})\bar{C}(x,t)c_{qx}c_{qy},\ q=1,\ldots,Q_m\\
&\delta g_q^-(n)=\frac{\sqrt{\Lambda}}{\Lambda^-}(Ak^n-Bk^{-n})\bar{C}(x,t)c_{qx}c_{qy}^2,\ n=0,1,\ldots,N=H-1,\ H\geqslant 3\\
&\text{with}\ \ A(n)=\{A_v,A_b\},\ B(n)=\{B_v,B_b\},\ k(n)=\{k_v(\Lambda_v),k_b(\Lambda_b)\},\ k(\Lambda)=\frac{2\sqrt{\Lambda}-1}{2\sqrt{\Lambda}+1}.
\end{aligned} \tag{64}$$

The half-system takes advantage of the symmetry on the channel axis. The four constants are then to be derived from the four following conditions: the two interface conditions (63), the bounce-back condition (26), and the axial-symmetry condition. Following uniform-Λ analysis in Sec. III D 1 for $\{g_q^{\pm}(n)=\delta g_q^{\pm}(n)\}$ and, as there, neglecting the variation of $\bar{C}(x)$ between the two interface nodes in leading-order analysis, the four closure conditions become

$$||S||=0,\quad \text{where}\ ||S||=\left(e_q^+ +\tfrac{1}{2}\delta g_q^- -\Lambda_v^+\delta g_q^+\right)\Big|_{n=n_v}-\left(e_q^+ -\tfrac{1}{2}\delta g_q^- -\Lambda_b^+\delta g_q^+\right)\Big|_{n=n_b},$$
$$\text{with}\ e_q^+|_{n=n_v}=e_q^+|_{n=n_b}=t_q^{(m)}c_e\bar{C}(x), \tag{65a}$$

$$||V||=0,\quad \text{with}\ ||V||=\left(e_q^- +\tfrac{1}{2}\delta g_q^+ -\Lambda^-\delta g_q^-\right)\Big|_{n=n_v}+\left(-e_q^- +\frac{1}{2}\delta g_q^+ +\Lambda^-\delta g_q^-\right)\Big|_{n=n_b}, \tag{65b}$$

$$\left(e_q^- +\tfrac{1}{2}\delta g_q^+ -\Lambda^-\delta g_q^-\right)\Big|_{n=n_b}=0,\quad \text{with}\ e_q^-(n_b)=t_q^{(a)}\bar{C}(x)U_x(n_b)c_{qx}, \tag{65c}$$

$$\delta g_q^+|_{n=n_i^+}=-\delta g_q^+|_{n=n_i^-}. \tag{65d}$$

Substituting Eqs. (64), we consider the respective differences of Eqs. (65) for two diagonal links with $c_{qx}=\pm1$, $c_{qy}^2=1$. Their common prefactor $\bar{C}(x)$ is factorized and the linear system takes the form

$$k_v^{(-1+N)}(1-2\sqrt{\Lambda_v})\sqrt{\Lambda_v}A_v-k_v^{(1-N)}(1+2\sqrt{\Lambda_v})\sqrt{\Lambda_v}B_v+k_b^N(2\sqrt{\Lambda_b}+1)\sqrt{\Lambda_b}A_b+k_b^{-N}(2\sqrt{\Lambda_b}-1)\sqrt{\Lambda_b}B_b=0, \tag{66a}$$

$$k_v^{(-1+N)}(1-2\sqrt{\Lambda_v})A_v+k_v^{(1-N)}(1+2\sqrt{\Lambda_v})B_v+k_b^N(1+2\sqrt{\Lambda_b})A_b+k_b^{-N}(1-2\sqrt{\Lambda_b})B_b=0, \tag{66b}$$

$$k_b^N(1-2\sqrt{\Lambda_b})A_b+k_b^{-N}(1+2\sqrt{\Lambda_b})B_b=-2t_d^{(a)}U_x(n_b) \tag{66c}$$

$$A_vk_v^N+B_v=0. \tag{66d}$$

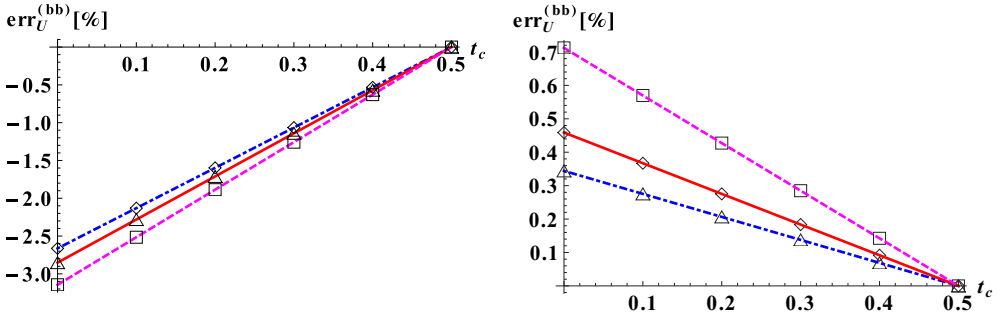

FIG. 14. Straight channel of $H = 12$ is modeled with the double-Λ BB scheme for (arbitrary) small value $\Lambda_b = \frac{1}{4} \times 10^{-2}$. The numerical results for relative velocity error $\mathrm{err}_U^{(bb)} = \mathrm{err}_U - \mathrm{err}_U^{(\mathrm{sum})}$ are displayed versus velocity-weight $t_c = t_c^{(a)}$, plug flow in the left diagram and parabolic flow in the right diagram. Their predicted respective solutions (69) and (77) are plotted by lines for $\Lambda = \{\frac{1}{6}, \frac{1}{4}, \frac{1}{2}\}$ [dashed-dotted line (blue, "lozenges"), solid line (red, "triangles"), dashed line (magenta, "squares")].

This system depends on the relaxation rates only via two Λ products: $\Lambda_v = \Lambda^- \Lambda_v^+$ and $\Lambda_b = \Lambda^- \Lambda_b^+$. The boundary-layer solution (64) is constructed by solving Eqs. (66) with respect to the four coefficients $\{A_v, B_v, A_b, B_b\}$. When $\Lambda_v = \Lambda_b = \Lambda$, $k(\Lambda) = \frac{2\sqrt{\Lambda}-1}{2\sqrt{\Lambda}+1}$, solution of Eqs. (66) reads as in c field with $U_x(n_b) = \mathcal{U}$

$$A = A_v = A_b = \frac{2t_d^{(a)}\mathcal{U}}{1 + 2\sqrt{\Lambda} + (1 + 2\sqrt{\Lambda})k^{1+N}}, \; B = B_v = B_b = -\frac{2t_d^{(a)}\mathcal{U}}{(1 + k^{-(1+N)})(2\sqrt{\Lambda} - 1)}. \tag{67}$$

With this solution, Eq. (64) is equivalent to the uniform-Λ solution given by Eqs. (52) and (53). Further procedure follows Sec. III D 1. The nonequilibrium correction (64) modifies the local advective flux by the quantity $\delta U(n)\mathcal{U}\partial_x \bar{C}(x,t) = -\Lambda^- \sum_{q=1}^{Q_m} \bar{\Delta}_x \delta g_q^-(n) c_{qx}$, with

$$\delta U(n) = -\frac{\sqrt{\Lambda} N_d}{\mathcal{U}}[A(n)k^n - B(n)k^{-n}]. \tag{68}$$

The averaged convective term in Eq. (7) is then modified by the quantity $\delta_a \mathcal{U}\partial_x \bar{C}(x,t)$, where the relative mean-velocity correction $\delta_a = \frac{1}{H}\sum_{n=0}^{H-1} \delta U(n)$ is computed via the arithmetical averaging of grid values:

$$\delta_a\left(t_c^{(a)}, \Lambda_v, \Lambda_b, H\right) = -\frac{N_d}{H\mathcal{U}}\left[2\sqrt{\Lambda_b}\left(A_b k_b^{H-1} - B_b k_b^{1-H}\right) + \sqrt{\Lambda_v}\sum_{n=1}^{H-2}\left(A_v k_v^n - B_v k_v^{-n}\right)\right]. \tag{69}$$

After substitution of the solution to Eq. (66), Eq. (69) gives

$$\delta_a\left(t_c^{(a)}, \Lambda_v, \Lambda_b, H\right) = \frac{2t_d^{(a)} N_d}{H} \frac{c_1[4\Lambda_b(\sqrt{\Lambda_v} - 1) + \sqrt{\Lambda_v}] - c_2[4\Lambda_b(\sqrt{\Lambda_v} + 1) + \sqrt{\Lambda_v}]}{c_1[1 + 4(\Lambda_b - \sqrt{\Lambda_v})] + c_2[1 + 4(\Lambda_b + \sqrt{\Lambda_v})]}, \text{ with}$$
$$c_1 = (1 + 2\sqrt{\Lambda_v})^2(-1 + 2\sqrt{\Lambda_v})^H, \; c_2 = (1 - 2\sqrt{\Lambda_v})^2(1 + 2\sqrt{\Lambda_v})^H. \tag{70}$$

This solution is valid when H is either even or odd number. It tells us that δ_a remains proportional to the diagonal velocity weight $t_d^{(a)}$ and it vanishes for $t_c^{(a)} = \frac{1}{2}$.

When $\Lambda_v = \Lambda_b = \Lambda$, Eq. (70) reduces to Eq. (55). The numerical configuration displayed in the left diagram in Fig. 14 is the same as used in Fig. 14 from [69], with $\Lambda_b = \frac{1}{4} \times 10^{-2}$ and $\Lambda_v = \{\frac{1}{6}, \frac{1}{4}, \frac{1}{2}\}$. Figure 14 illustrates that Eq. (70) describes exactly numerical solutions in double-Λ scheme when $\Lambda_v \neq \Lambda_b$, with $\mathrm{err}_U^{(bb)} = \mathcal{U}^{(\mathrm{num})}/\mathcal{U} - 1 = \delta_a(t_c^{(a)}, \Lambda_v, \Lambda_b, H)$. The straightforward idea is to try to vanish δ_a with the help of the specific dependency $\Lambda_b(\Lambda_v, H)$. By equating $\delta_a(t_c^{(a)}, \Lambda_v, \Lambda_b, H)$ from Eq. (70) to zero, solution for $\Lambda_b(\Lambda_v, H)$ reads as [with c_1 and c_2 from Eq. (70)]

$$\Lambda_b(\Lambda_v, H) = \frac{\sqrt{\Lambda_v}(c_2 - c_1)}{4[c_1(\sqrt{\Lambda_v} - 1) - c_2(\sqrt{\Lambda_v} + 1)]},$$
$$\lim \Lambda_b|_{\Lambda_v \to \infty} = \frac{2 - H}{4H}. \tag{71}$$

Yet, $\Lambda_b(\Lambda_v, H)$ is negative when $H \geqslant 2$. Figure 15 illustrates this situation in the left diagram. That means that there is no positive-valued required dependency $\Lambda_b(\Lambda_v, H)$ which is able to vanish δ_a in constant velocity field. However, small Λ_b will reduce the boundary-layer effect.

2. *Pure diffusion*

Recall that in the uniform-Λ BB scheme, the diffusion-coefficient correction $\delta_m(t_c^{(m)}, \Lambda, H)$ from Eq. (35) is exactly the same as the velocity correction in c field, $\delta_a(t_c^{(a)}, \Lambda, H)$ from Eq. (55). In agreement with the numerical simulations, the straightforward analysis shows that this feature remains valid in double-Λ BB scheme. That means that Eq. (70) exactly describes relative correction $\delta_m(t_c^{(m)}, \Lambda_v, \Lambda_b, H)$ to diffusion

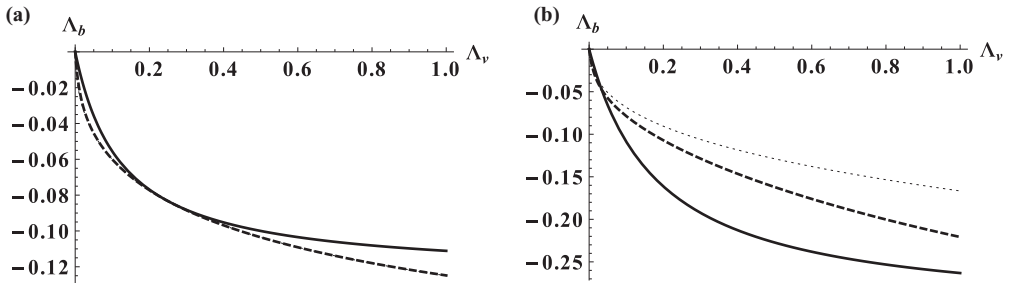

FIG. 15. The two diagrams show (a) exact solution $\Lambda_b(\Lambda_v,H)$ given by Eq. (71) for plug flow in straight channel, $H=\{4,8,16\}$ (solid, dashed, dotted lines) and (b) approximate solution $\Lambda_b(\Lambda_v,R)$ for plug flow in a capillary, $R=\{2,4,8\}$ (solid, dashed, dotted lines). The $\Lambda_b(\Lambda_v,\mathcal{L})$ is *negative* meaning that the desired solution *does not exist in plug flow*.

coefficient with double-Λ strategy: it reduces to Eq. (35) for uniform Λ. It follows from Eq. (71) that there is no suitable positive-valued dependency where δ_m vanishes in pure diffusion, but the small Λ_b is expected to reduce the delay and disparity with respect to the mass weight. In Sec. VI A we examine these predictions for the relative diffusivity of the simple porous structures.

3. *Parabolic velocity profile*

In Poseuille profile, the velocity correction $\mathcal{U}\delta U(n)$ in Eq. (56) is decomposed into two components with the coefficients $\mathcal{K}_1$ and $\mathcal{K}_2$. Based on the symmetry argument, the component of $\mathcal{K}_1$ is given by Eq. (24), while the component of $\mathcal{K}_2$ obeys Eq. (25). We extend this construction to three-layered double-Λ system and decompose $g_q^{\pm}$ into two components, say $g_q^{\pm}=g_q^{\pm(1)}+g_q^{\pm(2)}$, where $g_q^{\pm(i)}$ is further decomposed into bulk and boundary counterparts $g_q^{\pm(i)}(n)=G_q^{\pm(i)}(n)+\delta g_q^{\pm(i)}(n)$, $i=\{1,2\}$. The bulk component $G_q^{\pm}=G_q^{\pm(1)}+G_q^{\pm(2)}$ is built with the Chapman-Enskog expansion, where $G_q^{\pm(1)}(n)$ introduces the first- and second-order velocity gradients; and $\delta g_q^{\pm(1)}$ keeps its form (64)

$$
\begin{aligned}
G_q^{+(1)}(n)&=t_q^{(a)}\partial_y U_x(n)\bar{C}(x,t)c_{qx}c_{qy},\\
G_q^{-(1)}(n)&=-\Lambda^+(n)t_q^{(a)}\partial_y^2 U_x\bar{C}(x,t)c_{qx}c_{qy}^2,\\
\delta g_q^{+(1)}(n)&=(Ak^n+Bk^{-n})\bar{C}(x,t)c_{qx}c_{qy},\\
\delta g_q^{-(1)}(n)&=\frac{\sqrt{\Lambda(n)}}{\Lambda^-}(Ak^n-Bk^{-n})\bar{C}(x,t)c_{qx}c_{qy}^2,
\end{aligned}
$$

with $A(n)=\{A_v^{(1)},A_b^{(1)}\}$,

$$
B(n)=\{B_v^{(1)},B_b^{(1)}\},\ n=0,1,\dots,H-1. \tag{72}
$$

The second nonequilibrium component $G_q^{\pm(2)}(n)$ describes the evolution of $U_x(y)\partial_x\bar{C}(x,t)$ along the vertical axis [we write only its relevant components, which will define the accommodation solution $\{\delta g_q^{\pm(2)}(n)\}$]:

$$
\begin{aligned}
G_q^{+(2)}(n)&=\Lambda(n)t_q^{(a)}\partial_y^2 U_x\partial_x\bar{C}c_{qx}^2c_{qy}^2,\\
G_q^{-(2)}(n)&=-\Lambda^+(n)t_q^{(a)}\partial_y U_x(n)\partial_x\bar{C}c_{qx}^2c_{qy},\\
\delta g_q^{+(2)}(n)&=(Ak^n+Bk^{-n})\partial_x\bar{C}c_{qx}^2c_{qy}^2,\\
\delta g_q^{-(2)}(n)&=\frac{\sqrt{\Lambda(n)}}{\Lambda^-}(Ak^n-Bk^{-n})\partial_x\bar{C}c_{qx}^2c_{qy},
\end{aligned}
$$

$$
\text{with } A(n)=\{A_v^{(2)},A_b^{(2)}\},\ B(n)=\{B_v^{(2)},B_b^{(2)}\},\quad k(n)=\{k_v(\Lambda_v),k_b(\Lambda_b)\},\ n=0,1,\dots,H-1. \tag{73}
$$

The two components $g_q^{\pm(1)}(n)$ and $g_q^{\pm(2)}(n)$ require us to define their four individual constants. Since the set $\{g_q^{\pm(2)},G_q^{\pm(2)}\}$ scales with c_{qx}^2, it vanishes from the difference of the closure relations assigned for two diagonal links with $c_{qx}=\pm1$, $c_{qy}^2=1$. The inverse situation happens with the set $\{g_q^{\pm(1)},G_q^{\pm(1)}\}$: it scales with c_{qx} and it vanishes from the sum of two diagonal-link closure relations. Hence, due to linearity, the whole system is decomposed into two subsystems where the two sets of four coefficients can be derived independently. Each subsystem is composed of the two interface conditions, the bounce-back closure relation and the symmetry condition. The component $\{g_q^{\pm(1)},G_q^{\pm(1)}\}$ from Eq. (72) obeys

$$
\left(\tfrac{1}{2}\delta g_q^{-(1)}-\Lambda_v^+\delta g_q^{+(1)}\right)\Big|_{n=n_v}+\left(\tfrac{1}{2}\delta g_q^{-(1)}+\Lambda_b^+\delta g_q^{+(1)}\right)\Big|_{n=n_b}=-\left(\tfrac{1}{2}G_q^{-(1)}-\Lambda_v^+G_q^{+(1)}\right)\Big|_{n=n_v}-\left(\tfrac{1}{2}G_q^{-(1)}+\Lambda_b^+G_q^{+(1)}\right)\Big|_{n=n_b}, \tag{74a}
$$

$$
\begin{aligned}
&\left(\tfrac{1}{2}\delta g_q^{+(1)}-\Lambda^-\delta g_q^{-(1)}\right)\Big|_{n=n_v}+\left(\tfrac{1}{2}\delta g_q^{+(1)}+\Lambda^-\delta g_q^{-(1)}\right)\Big|_{n=n_b}\\
&\quad=-\left(e_q^-+\tfrac{1}{2}G_q^{+(1)}-\Lambda^-G_q^{-(1)}\right)\Big|_{n=n_v}-\left(-e_q^-+\tfrac{1}{2}G_q^{+(1)}+\Lambda^-G_q^{-(1)}\right)\Big|_{n=n_b},
\end{aligned} \tag{74b}
$$

$$
\left(\tfrac{1}{2}\delta g_q^{+(1)}-\Lambda^-\delta g_q^{-(1)}\right)\Big|_{n=n_b}=-\left(e_q^-+\tfrac{1}{2}G_q^{+(1)}-\Lambda^-G_q^{-(1)}\right)\Big|_{n=n_b},\quad \text{with } e_q^-(n_b)=t_q^{(a)}\bar{C}(x)U_x(n_b)c_{qx}, \tag{74c}
$$

$$
\delta g_q^{+(1)}|_{n=n_i^+}=-\delta g_q^{+(1)}|_{n=n_i^-}. \tag{74d}
$$

We substitute Eq. (72) into (74) and consider their four respective differences for two diagonal links with $c_{qx}=\pm1$, $c_{qy}^2=1$. The left-hand side of the linear system has the same form as in Eqs. (66). The right-hand side of the second equation simplifies since, with Eq. (72), $-(e_q^-+\frac{1}{2}G_q^{+(1)})|_{n=n_v}+(e_q^--\frac{1}{2}G_q^{+(1)})|_{n=n_b}=0$ on the parabolic velocity profile due to constant curvature. The

system (72) is solved with respect to the four constants $\{A_v^{(1)},B_v^{(1)},A_b^{(1)},B_b^{(1)}\}$; the solution is lengthy but its symbolic contribution $\delta\mathcal{U}^{(1)}\mathcal{U}$ to the convective term is built straightforwardly with Eq. (68). Like the δ_a in Eq. (57), $\delta\mathcal{U}^{(1)}$ remains proportional to the diagonal velocity weight $t_d^{(a)}$.

In turn, the component $\{g_q^{\pm(2)},G_q^{\pm(2)}\}$ from Eq. (73) obeys

$$\left(\tfrac{1}{2}\delta g_q^{-(2)}-\Lambda_v^{+}\delta g_q^{+(2)}\right)\big|_{n=n_v}+\left(\tfrac{1}{2}\delta g_q^{-(2)}+\Lambda_b^{+}\delta g_q^{+(2)}\right)\big|_{n=n_b}=-\left(\tfrac{1}{2}G_q^{-(2)}-\Lambda_v^{+}G_q^{+(2)}\right)\big|_{n=n_v}-\left(\tfrac{1}{2}G_q^{-(2)}+\Lambda_b^{+}G_q^{+(2)}\right)\big|_{n=n_b}, \tag{75a}$$

$$\left(\tfrac{1}{2}\delta g_q^{+(2)}-\Lambda^{-}\delta g_q^{-(2)}\right)\big|_{n=n_v}+\left(\tfrac{1}{2}\delta g_q^{+(2)}+\Lambda^{-}\delta g_q^{-(2)}\right)\big|_{n=n_b}=-\left(\tfrac{1}{2}G_q^{+(2)}-\Lambda^{-}G_q^{-(2)}\right)\big|_{n=n_v}-\left(\tfrac{1}{2}G_q^{+(2)}+\Lambda^{-}G_q^{-(2)}\right)\big|_{n=n_b}, \tag{75b}$$

$$\left(\tfrac{1}{2}\delta g_q^{+(2)}-\Lambda^{-}\delta g_q^{-(2)}\right)\big|_{n=n_b}=-\left(\tfrac{1}{2}G_q^{+(2)}-\Lambda^{-}G_q^{-(2)}\right)\big|_{n=n_b}, \tag{75c}$$

$$\delta g_q^{+(2)}|_{n=n_i^{+}}=\delta g_q^{+(2)}|_{n=n_i^{-}}. \tag{75d}$$

In that system, we consider the four respective sums for two diagonal links with $c_{qx}=\pm1$, $c_{qy}^2=1$ and solve it with respect to the four coefficients $\{A_v^{(2)},B_v^{(2)},A_b^{(2)},B_b^{(2)}\}$. The component $\{\delta g_q^{+(2)}\}$ modifies the averaged convective term by the quantity $\delta\mathcal{U}^{(2)}\mathcal{U}\partial_x\bar{C}(x,t)=-\frac{1}{H}\sum_n\sum_{q=1}^{Q_m}\delta g_q^{+(2)}(n)$ and $\delta\mathcal{U}^{(2)}$ reads as

$$\delta\mathcal{U}^{(2)}(t_c^{(a)},\Lambda_v,\Lambda_b,H)=-\frac{12[2\Lambda_b+(H-2)\Lambda_v]\left(1-2t_c^{(a)}\right)}{H^3}. \tag{76}$$

The entire mean-velocity relative correction is given by the sum of the two components:

$$\delta_a\left(t_c^{(a)},\Lambda_v,\Lambda_b,H\right)=\delta\mathcal{U}^{(1)}+\delta\mathcal{U}^{(2)}=F^{(a)}(\Lambda_v,\Lambda_b,H)\left(1-2t_c^{(a)}\right),\ \delta_a\left(t_c^{(a)}=\frac{1}{2}\right)=0. \tag{77}$$

Figure 14 illustrates in the right diagram the exact agreement between the predicted solution (77) and numerical results for $\mathrm{err}_U^{(bb)}=\mathrm{err}_U-\mathrm{err}_U^{(\mathrm{sum})}$. The parameters of these simulations correspond to Fig. 15 from [69]. These results indicate that, for sufficiently small Λ_b, the $\mathrm{err}_U^{(bb)}$ may become *positive*, meaning that the apparent velocity amplitude may *exceed* the prescribed velocity amplitude. This is in contrast with the situation in plug flow, where $\delta_a(t_c^{(a)},\Lambda_v,\Lambda_b,H)$ is negative in Eq. (70). We consider equation $F^{(a)}(\Lambda_v,\Lambda_b,H)=0$. Its root reads as [with c_1 and c_2 from Eq. (70)]

$$\begin{aligned}\Lambda_b^{(\mathrm{sol})}(\Lambda_v)&=\frac{A^{(\mathrm{sol})}\sqrt{\Lambda_v}}{4B^{(\mathrm{sol})}},\ \lim\Lambda_b|_{\Lambda_v\to\infty}=\frac{(H-2)[3+2H(H-4)]}{4H(1+2H^2)},\ \text{with}\\ A^{(\mathrm{sol})}&=c_1[1+8\Lambda_v+4\sqrt{\Lambda_v}(H-2)]-c_2[1+8\Lambda_v-4\sqrt{\Lambda_v}(H-2)],\\ B^{(\mathrm{sol})}&=c_1\{-1+2H[1-2\sqrt{\Lambda_v}(1-\sqrt{\Lambda_v})]+\sqrt{\Lambda_v}[3-8\sqrt{\Lambda_v}(1-\sqrt{\Lambda_v})]\}\\ &\quad+c_2\{-1+2H[1+2\sqrt{\Lambda_v}(1+\sqrt{\Lambda_v})]-\sqrt{\Lambda_v}[3+8\sqrt{\Lambda_v}(1+\sqrt{\Lambda_v})]\}.\end{aligned} \tag{78}$$

This solution is illustrated in the two first diagrams in Fig. 16. It is shown that asymptotically, as H increases, $\Lambda_b^{(\mathrm{sol})}\in\approx[0.02,0.05]$ for $\Lambda_v\in[\frac{1}{12},\frac{1}{4}]$, but $\Lambda_b^{(\mathrm{sol})}$ rapidly reduces towards zero when $H<\approx10$. Numerical simulations confirm that err_U becomes equal to $\mathrm{err}_U^{(\mathrm{sum})}$ for any velocity weight thanks to the double-Λ scheme (78). Thereby, solution (78) allows to preserve the correct mean velocity in Poiseuille profile for any velocity weight. The striking point is that $\Lambda_b^{(\mathrm{sol})}(\Lambda_v,H)$ is independent of other model parameters and Pe. The dispersion and high-order moments by double-Λ approach in straight channel are discussed in Sec. V A.

C. Cylindrical capillary

In a capillary, the specific value Λ_b is set in all boundary nodes where the bounce back applies at least for one outgoing link, while Λ_v applies for all other nodes (see Fig. 13). The construction of the boundary layers combines the double-Λ interface analysis developed in straight channel with the uniform-Λ nonequilibrium solutions for cylindrical pipe from Sec. II C. As there, we adapt the channel solution for any one of the coordinate axes in circular cross section. In plug profile $U_x(y,z)=\mathcal{U}$, the nonequilibrium solution (68) with the coefficients (66) is adapted and the mean-velocity correction $\delta_a=\langle\delta U\rangle$ is estimated with Eq. (34). In Poiseuille profile $U_x(r)=2\mathcal{U}(1-\frac{r^2}{R^2})$, solution for $\delta_a(t_c^{(a)},\Lambda_v,\Lambda_b,R)$ is derived in the two-component form, similarly to Eq. (77). The two components are built solving Eqs. (74) and (75) for the coefficients. In that, we replace ∂_yU_x by ∂_rU_x and $\partial_y^2U_x$ by $\partial_r^2U_x$, with H replaced by $2R$ and $N_d=4$ (d2Q9) by $N_d=8$ (d3Q15). Solution $\delta_a(t_c^{(a)},\Lambda_v,\Lambda_b,R)$ is then derived similar to Eq. (57). As in the case of the uniform Λ, δ_a remains proportional to the diagonal velocity weight $t_d^{(a)}$.

Next, the two solutions $\delta_a(t_c^{(a)},\Lambda_v,\Lambda_b,R)$, derived in c field and p field, are equated to zero. It happens that $\Lambda_b(\Lambda_v,R)$

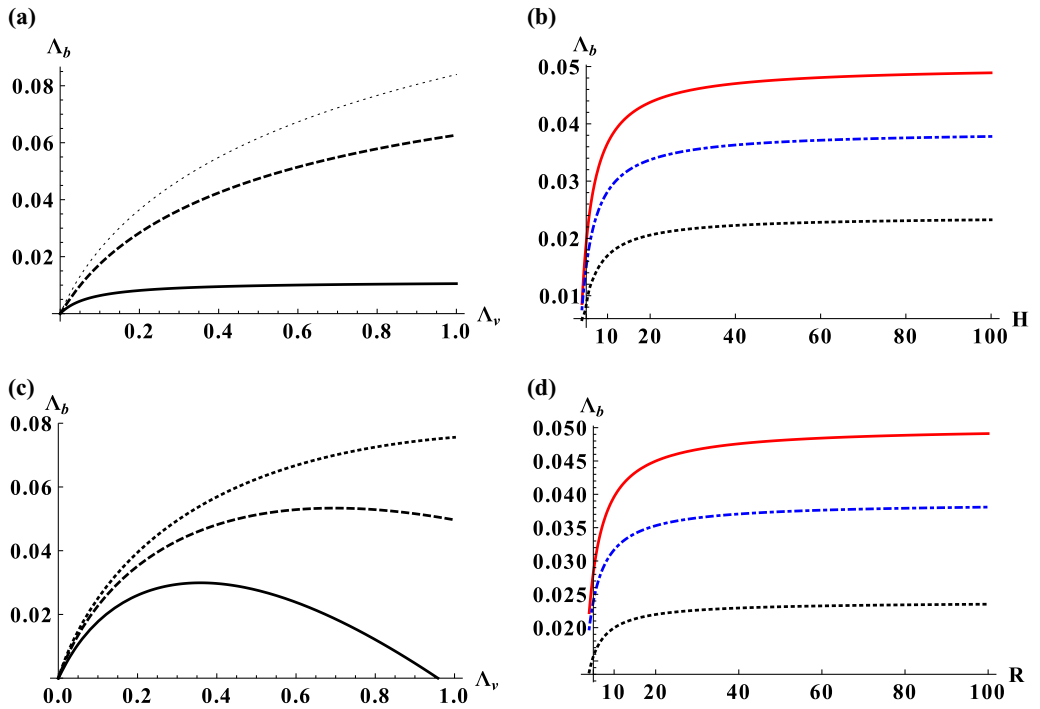

FIG. 16. The two first diagrams (a) and (b) plot solution (71) for $\Lambda_b^{(\mathrm{sol})}(\Lambda_v, H)$ in double-Λ scheme derived for parabolic profile in 2D channel. (a) $\Lambda_b(\Lambda_v)$ for $H = \{4,8,16\}$ (solid, dashed, dotted lines) and (b) $\Lambda_b(H)$ for $\Lambda_v = \{\frac{1}{12}, \frac{1}{6}, \frac{1}{4}\}$ [dotted line (black), dotted-dashed line (blue), solid line (red)]. The two last diagrams (c) and (d) plot solution $\Lambda_b(\Lambda_v, R)$ for parabolic flow in a capillary. (c) $\Lambda_b^{(\mathrm{sol})}(\Lambda_v)$ for $R = \{5,10,20\}$ (solid, dashed, dotted lines) and (d) $\Lambda_b^{(\mathrm{sol})}(R)$ for $\Lambda_v = \{\frac{1}{12}, \frac{1}{6}, \frac{1}{4}\}$ [dotted line (black), dotted-dashed line (blue), solid line (red)].

is negative in c field, alike in straight channel. Figure 15 illustrates this situation in the right diagram. However, the positive-valued branch $\Lambda_b^{(\mathrm{sol})}(\Lambda_v, R)$ exists in Poiseuille profile, at least in the most relevant interval $\Lambda_v \in]0, \approx 1]$. This is displayed in the third and fourth diagrams in Fig. 16 for $R \geqslant 5$. Typically, the available Λ_v interval enlarges as R increases. The second and the fourth diagrams in Fig. 16 show that the dependency $\Lambda_b^{(\mathrm{sol})}(\Lambda_v)$ versus R in cylindrical capillary, and the dependency $\Lambda_b^{(\mathrm{sol})}(\Lambda_v)$ versus H in straight channel have very similar form and amplitude. Since this dependency $\Lambda_b(\Lambda_v, R)$ is lengthy in cylindrical capillary, several specific combinations $\{\Lambda_v, \Lambda_b(\Lambda_v, R)\}$ are exemplified in Table III for bulk values $\Lambda_v = \{\frac{1}{12}, \frac{1}{6}, \frac{1}{4}, \frac{1}{2}\}$. Table IV examines their numerical results in a small pipe of $R = 5$ when $t_c^{(a)} = \frac{1}{3}$. It displays $\mathrm{err}_U^{(\mathrm{num})}$ and $\mathrm{err}_U^{(\mathrm{num})}/\mathrm{err}_U^{(\mathrm{sum})}$ obtained with the uniform-Λ and double-Λ BB schemes. With the double-Λ scheme, the $\mathrm{err}_U^{(\mathrm{num})}/\mathrm{err}_U^{(\mathrm{sum})}$ becomes approximately equal to 1 for four examined values Λ_v, meaning that the boundary-layer component $\mathrm{err}_U^{(bb)} = \mathrm{err}_U^{(\mathrm{num})} - \mathrm{err}_U^{(\mathrm{sum})}$ almost vanishes. It should be said that although $\mathcal{U}^{(\mathrm{num})} \equiv \mathcal{U}^{(\mathrm{sum})}$ on solution $\Lambda_b^{(\mathrm{sol})}(\Lambda_v, H)$ in a channel, $\Lambda_b^{(\mathrm{sol})}(\Lambda_v, R)$ does not account for the discretization effect exactly, and only the approximate solution $\mathcal{U}^{(\mathrm{num})} \approx \mathcal{U}^{(\mathrm{sum})}$ is expected. Figure 17 illustrates these results for $R = \{5,10,20\}$ by applying $\Lambda_b(\Lambda_v)$ from Table III. These results can be compared with Fig. 12 for uniform Λ. We observe that $\mathcal{U}^{(\mathrm{num})}(R)$ converges to $\mathcal{U}^{(\mathrm{sum})}(R)$ rapidly when the discretization properties improve (cf. $R = 5$ and 10). However, the convergence is not monotonous: $|\mathrm{err}_U^{(bb)}(R)|$ is larger for $R = 20$ than for $R = 10$, that is in accord with the $\mathrm{err}_U^{(\mathrm{sum})}$ from Table I. As expected, there still exists a very small (unpredicted) difference between $\mathcal{U}(R)$ and $\mathcal{U}^{(\mathrm{sum})}(R)$, with the maximum relative difference of about 0.25% for $R = 5$ and

TABLE III. This table provides distribution $\Lambda_b^{(\mathrm{sol})}(\Lambda_v, R)$ for double-Λ bounce-back scheme in cylindrical capillary. It vanishes the approximate of the relative mean-velocity correction $\delta_a(t_c^{(a)}, \Lambda_v, \Lambda_b, H)$.

Λ_v	$R = 5$	$R = 10$	$R = 20$
$\frac{1}{12}$	1.567×10^{-2}	1.997×10^{-2}	2.197×10^{-2}
$\frac{1}{6}$	2.393×10^{-2}	3.167×10^{-2}	3.53×10^{-2}
$\frac{1}{4}$	2.824×10^{-2}	3.963×10^{-2}	4.499×10^{-2}
$\frac{1}{2}$	2.766×10^{-2}	5.126×10^{-2}	6.249×10^{-2}

TABLE IV. This table reports the relative velocity correction $\mathrm{err}_U^{(\mathrm{num})}$ in d3Q15 BB with $t_c^{(a)} = \frac{1}{3}$, and compares it with the $\mathrm{err}_U^{(\mathrm{sum})} = -1.6\%$ in a small pipe of $R = 5$, for uniform-Λ scheme in the two first columns and the double-Λ scheme from Table III in the two last columns.

	$\Lambda_b = \Lambda_v$		$\Lambda_b = \Lambda_b^{(\mathrm{sol})}(\Lambda_v)$	
Λ_v	$\mathrm{err}_U(\%)$	$\mathrm{err}_U/\mathrm{err}_U^{(\mathrm{sum})}$	$\mathrm{err}_U(\%)$	$\mathrm{err}_U/\mathrm{err}_U^{(\mathrm{sum})}$
$\frac{1}{12}$	−2.37	1.48	−1.52	0.948
$\frac{1}{6}$	−3.06	1.91	−1.62	1.01
$\frac{1}{4}$	−3.72	2.32	−1.59	0.997
$\frac{1}{2}$	−5.49	3.43	−1.45	0.905

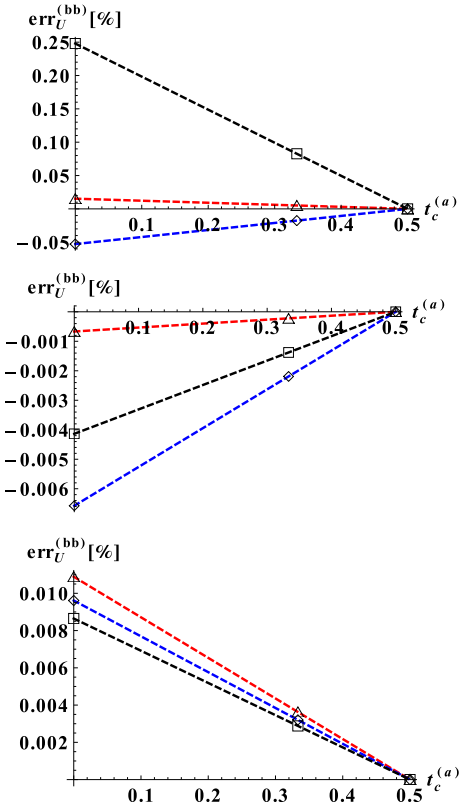

FIG. 17. This figure displays numerical results (lines with symbols) obtained with the d3Q15 double-Λ BB scheme in cylindrical capillary with the help of solution $\Lambda_b^{(\mathrm{sol})}(\Lambda_v, R)$ from Table III. The relative velocity error $\mathrm{err}_U^{(bb)} = \mathrm{err}_U - \mathrm{err}_U^{(\mathrm{sum})}$ in Poiseuille flow is displayed when $R = \{5,10,20\}$, from the top to the bottom. To be compared with Fig. 12 for uniform Λ. The numerical results are plotted for bulk values $\Lambda_v = \{\frac{1}{12}, \frac{1}{6}, \frac{1}{4}\}$ ["squares" (black), "lozenges" (blue), "triangles" (red)].

about $(7 \times 10^{-3})\%$ for $R = 10$ when $\Lambda \in [\frac{1}{12}, \frac{1}{4}]$. The third diagram in Fig. 10 confirms the velocity improvement on the distribution profiles: all of them are advected correctly with the double-Λ BB scheme and the profiles of $\Lambda_v = \frac{1}{12}$ and $\frac{1}{4}$ almost collapse for $t_c^{(a)} = \{\frac{1}{2}, \frac{1}{3}, 0\}$. The dispersion and high-order moments by double-Λ scheme in cylindrical capillary are discussed in Sec. V B.

V. DISPERSION, SKEWNESS, AND KURTOSIS WITH THE DOUBLE-Λ SCHEME

Our main objective is to verify the validity of the double-Λ scheme for reduction of the spurious effects in first four distribution moments. The bulk predictions [30] for the dimensionless coefficients of Taylor dispersion (k_T), skewness ($\mathrm{Sk}_\star$), and kurtosis ($\mathrm{Ku}_\star$) account for the relative (truncation and discretization) corrections to their physical values. In what follows, the predicted relative bulk corrections [30] to diffusion or dispersion coefficient D in Eq. (7), $\mathrm{Sk}_\star$ and $\mathrm{Ku}_\star$ in Eq. (9) are quantified via err_D, err(Sk), and err(Ku), respectively, and they are compared to numerical results. We address the simulations [30] and compare the specular-forward reflection results in straight channel with the bounce-back results. In turn, the bounce-back simulations are run with the uniform-Λ and double-Λ schemes in straight channel (Sec. V A) and cylindrical capillary (Sec. V B).

A. Straight channel

The uniform-Λ SNL scheme. A very good agreement is achieved [30] in a channel between the bulk predictions and numerical results with the help of the specular-forward boundary reflection (SNL), in full parameter space of the TRT model given by Eqs. (1) and (2). Recall that for any weights, this boundary rule is free from the bounce-back artifacts. Figures 18 and 19 illustrate this: they display the d2Q9 SNL results ("empty" symbols) for $\mathrm{Pe} \approx 9.5$ [$c_e = \frac{1}{3}$, $(\Lambda^-)^2 = \frac{1}{12}$] and $\mathrm{Pe} \approx 95$ [$c_e = \frac{1}{30}$, $(\Lambda^-)^2 = \frac{1}{12}$], respectively. In these figures, the two (limit) velocity-weight values $t_c^{(a)} = \frac{1}{2}$ and $t_c^{(a)} = 0$ are displayed together. The results are also displayed for two (limit) mass-weight values: (i) $t_c^{(m)} = \frac{1}{2}$ in the top row and (ii) $t_c^{(m)} = 0$ in the bottom row. In full agreement with the bulk predictions, (i) all three numerical coefficients are velocity weight independent at $\Lambda \approx \frac{1}{12}$; (ii) the k_T and $\mathrm{Sk}_\star$ are mass weight independent; and (iii) the $\mathrm{Ku}_\star$ depends on it noticeably at small $\mathrm{Pe} \approx 9.5$ (Fig. 18).

The uniform-Λ BB scheme. Figures 18 and 19 also display the d2Q9 BB results in the same configurations. The SNL and BB coincide only for $t_c^{(m)} = t_c^{(a)} = \frac{1}{2}$ in the top row diagrams. Because of the diffusion boundary layer, the BB results depend on the mass weight and, hence, they differ between the top and bottom rows. First, in the first top row diagrams in Figs. 18 and 19, the err_D deviates from the bulk estimate for "rotated" velocity weight $\{t_c^{(a)} = 0, t_c^{(m)} = \frac{1}{2}\}$ because of the (positive) boundary-layer numerical dispersion $\mathrm{err}_D^{(bb,U)}$. This component is predicted [69] similar to Eq. (58) with Eq. (62). When its analytical estimate is added to predicted bulk value, the bounce-back numerical results and predictions approach very closely.

Second, in the first diagram in the bottom row in Figs. 18 and 19, the additional (negative) diffusion boundary-layer correction $\mathrm{err}_D^{(bb)}(t_c^{(m)})$ due to "rotated" mass weight $\{t_c^{(m)} = 0, t_d^{(m)} = \frac{1}{4}\}$ should be added to the top-row estimate. This component is predicted by Eq. (27) with Eqs. (35a) and (36a). When $\mathrm{err}_D^{(bb)}$ is accounted for, the entire analytical estimate perfectly fits the numerical results for all weights. Note that the $\mathrm{err}_D^{(bb)}$ dominates both bulk and boundary-layer dispersion corrections for $\mathrm{Pe} \approx 9.5$ but, as it has been expected, its role becomes insignificant as Pe increases to $\mathrm{Pe} \approx 95$.

Third, $\mathrm{Sk}_\star^{(\mathrm{num})}$ (the second diagram) and $\mathrm{Ku}_\star^{(\mathrm{num})}$ (the third diagram) in Figs. 18 and 19 disagree with their respective bulk estimates and the SNL results in the presence of the diagonal weights. Recall that the asymptotically constant deviation in kurtosis, because of the diffusion boundary layer, was predicted and confirmed in pure-diffusion simulations in Sec. III B. We are not yet aware of the boundary-layer predictions for $\mathrm{Sk}_\star$ and $\mathrm{Ku}_\star$ in motion. We only note that their deviations are especially noticeable only for relatively small value $\mathrm{Pe} \approx 9.5$ in the limit case $t_c^{(m)} = 0$ (see two diagrams in the bottom row in Fig. 18). When $\mathrm{Pe} \approx 95$ in Fig. 19, the relative deviations reduce for $\mathrm{Sk}_\star$ and $\mathrm{Ku}_\star$ but they still remain larger for $t_c^{(a)} = 0$. These results confirm that although the principal deviation in $\mathrm{Sk}_\star$ and, especially,

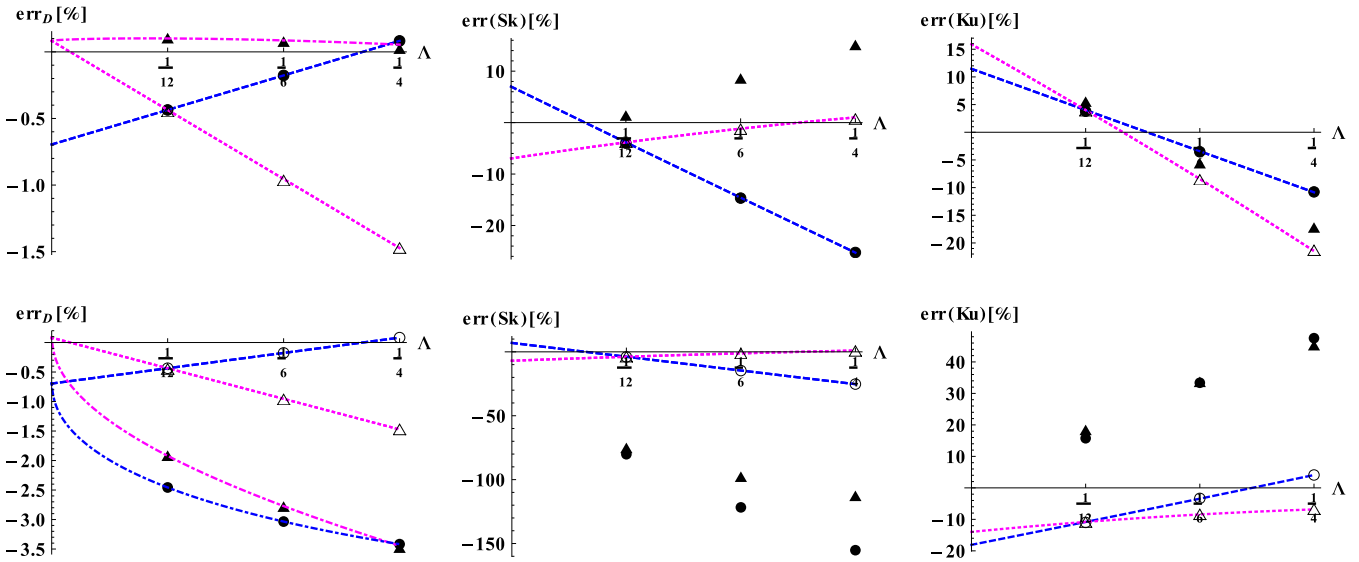

FIG. 18. The err_D, err(Sk), and err(Ku) (from the left to the right) at Pe ≈ 9.5 in straight Poiseuille profile. The results are plotted together for d2Q9 SNL ("empty" symbols) and d2Q9 BB ("filled" symbols) and compared to bulk predictions (lines) when velocity weight $t_c^{(a)} = \frac{1}{2}$ [dashed line (blue), "circles"] and $t_c^{(a)} = 0$ [dotted line (magenta), "triangles"]. Top row: mass weight $t_c^{(m)} = \frac{1}{2}$. Bottom row: $t_c^{(m)} = 0$. In the first column, the d2Q9 SNL agrees with the bulk prediction $\mathrm{err}_D^{(\mathrm{bulk})}(t_c^{(a)})$; the d2Q9 BB agrees with $\mathrm{err}_D^{(\mathrm{bulk})}(t_c^{(a)}) + \mathrm{err}_D^{(bb)}(t_c^{(m)}) + \mathrm{err}_D^{(bb,U)}(t_c^{(a)})$, with account of the boundary-layer diffusion and dispersion corrections.

$\mathrm{Ku}_\star$, is due to the diffusion-boundary layer, similar to the observation [30] in plug flow, the boundary-layer velocity and dispersion affect them at the intermediate Pe range. The last diagram in Fig. 9 shows that, despite the distinctness in high-order transport coefficients, there is not any visually observed difference between the profiles modeled with the d2Q5 BB and the "rotated" d2Q5 BB schemes because of the small-valued coefficients $\mathrm{Sk}_\star$ and $\mathrm{Ku}_\star$ at Pe ≈ 9.5.

The double-Λ *BB scheme.* Figures 20 and 21 address the same configurations as in Figs. 18 and 19, respectively, but with the double-Λ scheme (78). For consistency of the comparison, the SNL also applies double-Λ scheme (the SNL then agrees slightly less accurately with the theoretical predictions [30] than in Figs. 18 and 19 because the predictions [30] do not account for the nonuniformity in Λ).

Our focus is on the BB scheme. Recall, the root $\Lambda_b^{(\mathrm{sol})}(\Lambda_v)$ given by (78) suppresses the retardation of the mean velocity due to the diagonal velocity weight $t_d^{(a)}$ and $\mathcal{U}^{(\mathrm{num})}$ becomes equal to $\mathcal{U}^{(\mathrm{sum})}$ for any weights and model parameters. Therefore, the double-Λ BB scheme (78) is expected to vanish or reduce the boundary-layer dispersion component $\mathrm{err}_D^{(bb,U)}(t_c^{(a)})$ from Eq. (58).

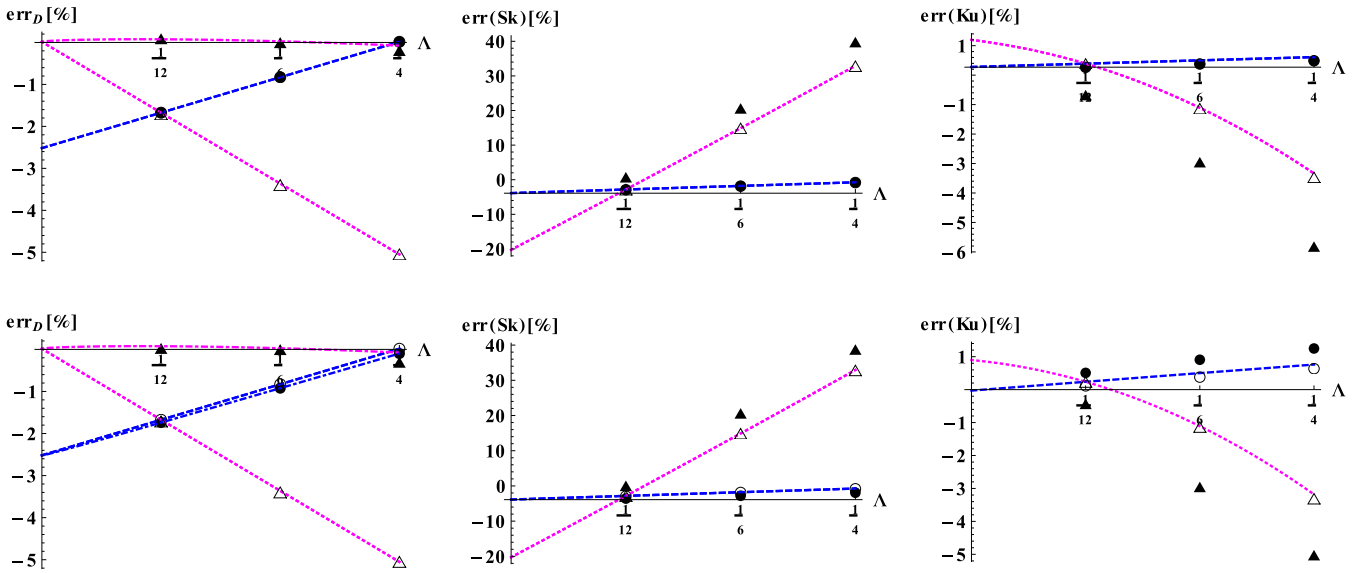

FIG. 19. Similarly as in Fig. 18 but for Pe ≈ 95.

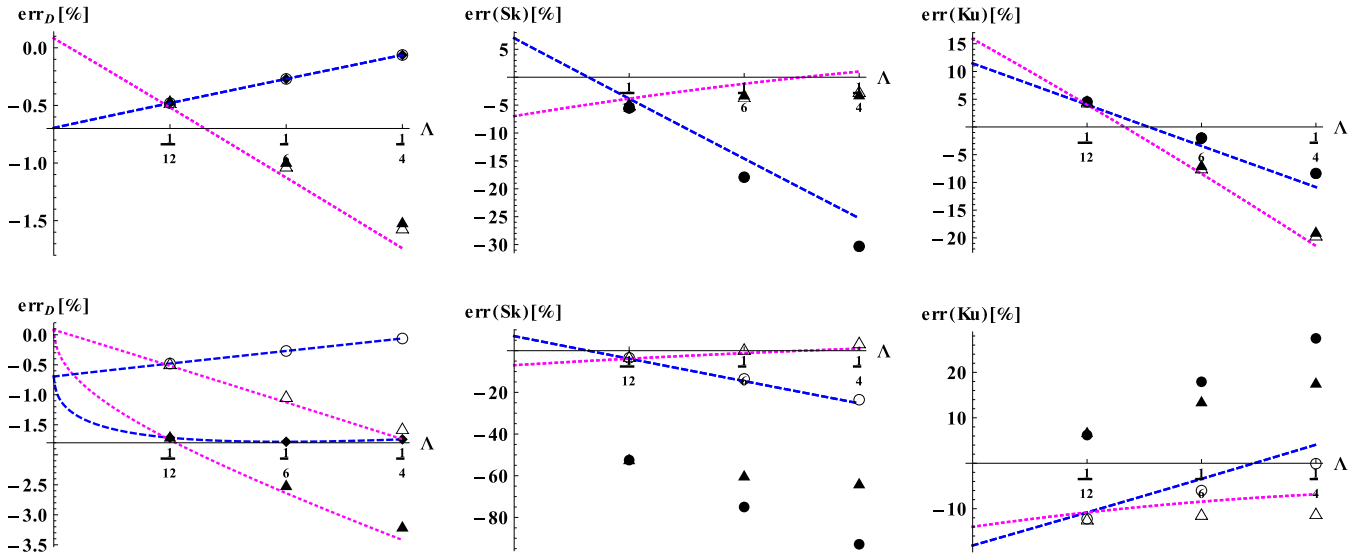

FIG. 20. Similarly as in Fig. 18, Pe ≈ 9.5, but the d2Q9 SNL and d2Q9 BB are both applied with the double-Λ scheme (78). Top row: $t_c^{(m)} = \frac{1}{2}$. Bottom row: $t_c^{(m)} = 0$. The d2Q9 BB results for err_D are compared to $\mathrm{err}_D^{(\mathrm{bulk})} + \mathrm{err}_D^{(bb)}(t_c^{(m)})$.

When $t_c^{(m)} = \frac{1}{2}$, there is no boundary-layer diffusion, hence, $\mathrm{err}_D^{(bb)}(t_c^{(m)}) = 0$. The two first (top row) diagrams in Figs. 20 and 21 confirm that the double-Λ BB scheme agrees with the SNL result and bulk prediction $\mathrm{err}_D^{(\mathrm{num})} \approx \mathrm{err}_D^{(\mathrm{bulk})}$. Notice that despite the correct advection velocity, $|\mathrm{err}_D|$ may become larger with the double-Λ scheme because of the canceling effect, e.g., when err_D sums the *negative* bulk value $\mathrm{err}_D^{(\mathrm{bulk})}$ and the *positive* boundary-layer value $\mathrm{err}_D^{(bb,U)}(t_c^{(a)})$ with the uniform-Λ scheme. The three diagrams in the top row in Figs. 20 and 21 show that the SNL and BB results become quasi-identical even in the limit case $t_c^{(a)} = 0$. This confirms that the double-Λ scheme efficiently suppresses velocity retardation due to velocity weight in the first four moments.

Figure 20 shows that when $t_c^{(m)} = 0$ (in the bottom row), the difference between the SNL and the BB results is well described by $\mathrm{err}_D^{(bb)}(t_c^{(m)}, \Lambda_b, H)$ [where Λ_b replaces Λ in Eq. (35a)]; consequently, its amplitude decreases with Λ_b. Recall that (i) there is no positive root $\Lambda_b(\Lambda_v)$ where $\mathrm{err}_D^{(bb)}$ vanishes in the pure-diffusion case, and (ii) the double-Λ dependency given by Eq. (78) is not called to vanish the boundary-layer diffusion-coefficient correction $\mathrm{err}_D^{(bb)}$ due to the diagonal mass weight. However, the relatively small value of Λ_b given by Eq. (78) is expected to reduce the diffusion retardation effect, in agreement wih the results in two first bottom-row diagrams in Figs. 20 and 21. However, we observe that the boundary-layer diffusion effect remains significant with $t_c^{(m)} = 0$ for skewness and kurtosis at Pe ≈ 9.5 (although the distance between the BB and SNL is reduced by factor 2 due to small Λ_b). As Pe increases to Pe ≈ 95, Fig. 21 confirms that the SNL and BB produce very similar results in the three transport coefficients for all weight combinations due to double-Λ distribution (78).

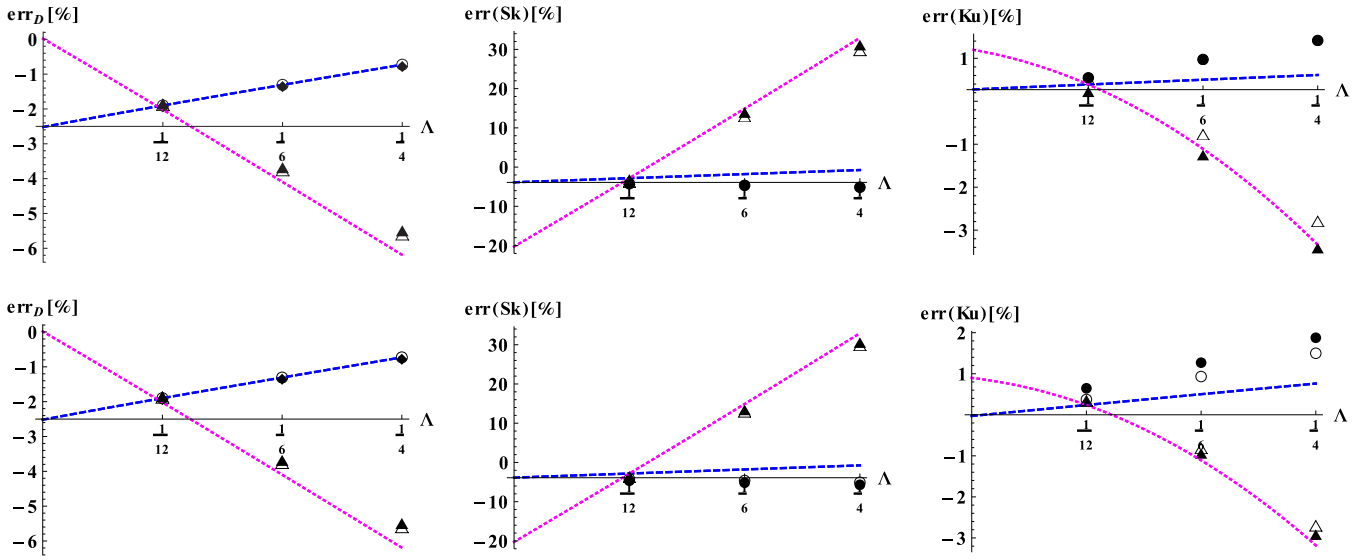

FIG. 21. Similarly as in Fig. 19, Pe ≈ 95, but the d2Q9 SNL and d2Q9 BB are both applied with the double-Λ distribution (78).

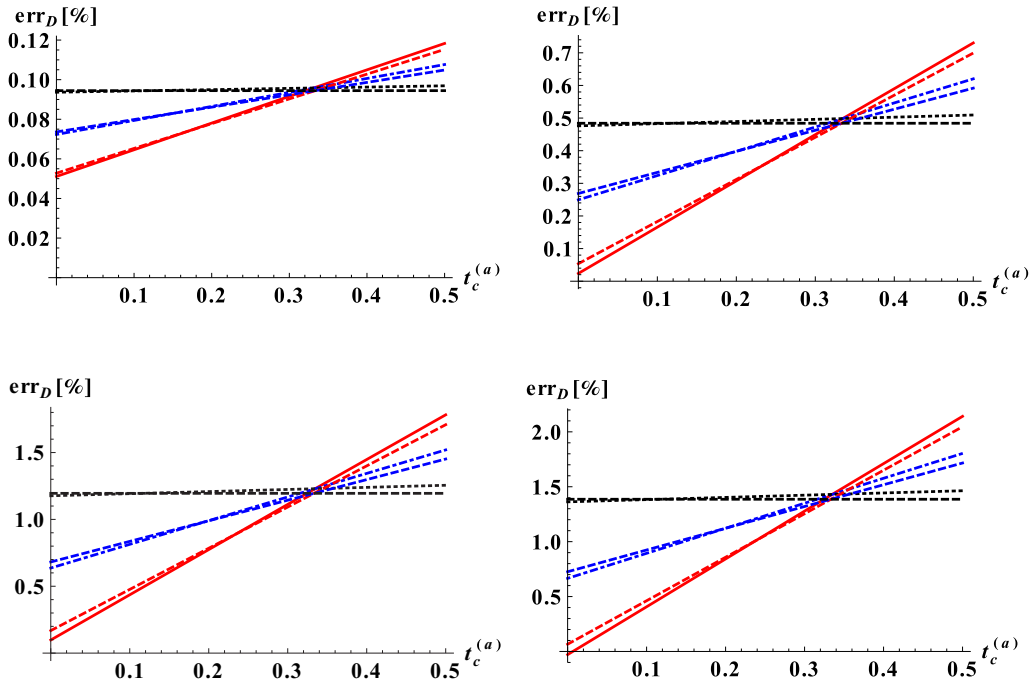

FIG. 22. The numerical estimate of the apparent bulk dispersion $\mathrm{err}_D^{(\mathrm{num})} - (\mathrm{err}_D^{(bb)} + \mathrm{err}_D^{(bb,U)})$ is compared to its bulk prediction $\mathrm{err}_D^{(\mathrm{bulk})}$ from [30] (dashed lines of the same color as the numerical data), in Poiseuille flow in cylindrical capillary of $R = 20$, with parameters of Expt. I–Expt. IV (Table II) from the left to the right and from the top to the bottom. The numerical simulations are run with the uniform $\Lambda = \{\frac{1}{12}, \frac{1}{6}, \frac{1}{4}\}$.

In summary, the double-Λ BB scheme proves its efficiency in parabolic profile for vanishing velocity retardation and reduction of the associated numerical dispersion $\mathrm{err}_D^{(bb,U)}$. Using the double-Λ scheme, the results of the bounce back and specular reflection almost coincide providing that the diffusion boundary-layer effect is small, that is, when Pe is sufficiently large or when $t_c^{(m)} \approx \frac{1}{2}$ at small Pe. In these cases, the truncation estimate [30] predicts well the numerical values for k_T, $\mathrm{Sk}_\star$, and $\mathrm{Ku}_\star$ with any velocity weight.

B. Cylindrical capillary

Like in a channel, the truncation and discretization bulk corrections to Taylor-dispersivity coefficient in a cylindrical capillary ($k_T = \frac{\mathrm{Pe}^2}{192}\mathrm{Pe} = \frac{2\mathcal{U}R}{D_0}$) and to reference values [29,30] for $\mathrm{Sk}_\star$ and $\mathrm{Ku}_\star$ are derived [30]. Numerical simulations [30] are performed with the d3Q15 BB scheme, mostly using $t_c^{(m)} = \frac{1}{3}$ for the fourth-order isotropy required by the truncation estimate, and adopting the parameter range from Table II. It has been shown [30] that the truncation estimate applies but less accurately when $t_c^{(m)} \neq \frac{1}{3}$ and, in particular, that it predicts well the d3Q7 dispersion result [80] for Newtonian fluid at $\mathrm{Pe} \approx 50$, where summation (discretization) component dominates the truncation counterpart. Like in a channel, the $D^{(\mathrm{num})}$ is extracted from the second moment with Eq. (8) and its relative correction $\mathrm{err}_D^{(\mathrm{num})} = D^{(\mathrm{num})}/D - 1$ is compared to bulk and boundary-layer predictions. The bulk prediction $\mathrm{err}_D^{(\mathrm{bulk})}$ is singled out [30] by accounting for the diffusion-layer correction $\mathrm{err}_D^{(bb)}$ from Eq. (27) and the boundary-layer dispersion correction $\mathrm{err}_D^{(bb,U)}$ from Eq. (58); the $\mathrm{err}_D^{(bb)}$ is extracted from the pure-diffusion simulation, the $\mathrm{err}_D^{(bb,U)}$ is computed with Eq. (62). Figure 22 compares the numerical results for $\mathrm{err}_D^{(\mathrm{num})} - (\mathrm{err}_D^{(bb)} + \mathrm{err}_D^{(bb,U)})$ to predicted solution $\mathrm{err}_D^{(\mathrm{bulk})}$ in four experiments from Table II, by applying the *uniform*-Λ BB scheme with $\Lambda \in [\frac{1}{12}, \frac{1}{4}]$. The agreement with the predictions is rather accurate in the whole interval $t_c^{(a)} \in [0, \frac{1}{2}]$. The larger discrepancy than in a channel is expected because the discretization effect is partly neglected in $\mathrm{err}_D^{(bb,U)}$. Figure 23 explicitly illustrates the effect of the boundary-layer dispersion within the uniform-Λ BB scheme. The computations are the same as in Fig. 22 but, with the *intentional neglect* of the $\mathrm{err}_D^{(bb,U)}$, the difference $\mathrm{err}_D^{(\mathrm{num})} - \mathrm{err}_D^{(bb)}$ principally disagrees with the $\mathrm{err}_D^{(\mathrm{bulk})}$.

We address now the double-Λ scheme in a capillary. It has been demonstrated in Fig. 17 that the specific solution $\Lambda_b^{(\mathrm{sol})}(\Lambda_v, R)$ from Table III effectively diminishes the boundary-layer mean-velocity correction due to the diagonal velocity weight. Figure 24 presents the comparison of the $\mathrm{err}_D^{(\mathrm{num})} - \mathrm{err}_D^{(bb)}(t_c^{(m)})$ and $\mathrm{err}_D^{(\mathrm{bulk})}$, like in Fig. 23, but when the double-Λ BB scheme from Table III is employed. Here, in contrast with the uniform-Λ results in Fig. 23, the agreement is satisfactory. The best accuracy is achieved with $\Lambda_v = \frac{1}{12}$ where $\mathrm{err}_D^{(\mathrm{num})}$ is $t_c^{(a)}$ independent. This result confirms that $\mathrm{err}_D^{(bb,U)}(t_c^{(a)})$ is efficiently removed and the observed velocity-weight dependency in $\mathrm{err}_D^{(\mathrm{num})} - \mathrm{err}_D^{(bb)}(t_c^{(m)})$ is due to truncation component $\mathrm{err}_D^{(\mathrm{tr})}(t_c^{(a)}, \Lambda)$ [recall [30], $\mathrm{err}_D^{(\mathrm{tr})}(t_c^{(a)}, \Lambda)$ is $t_c^{(a)}$ independent when $\Lambda = \frac{1}{12}$]. Like in a channel, a slightly larger discrepancy with the bulk prediction in comparison with the uniform-Λ scheme in Fig. 22 is, most likely, due to $\mathrm{err}_D^{(\mathrm{tr})}(t_c^{(a)}, \Lambda)$ because it does not account for the double-Λ distribution. Besides, one may suggest that although the double-Λ scheme accurately preserves the mean velocity in

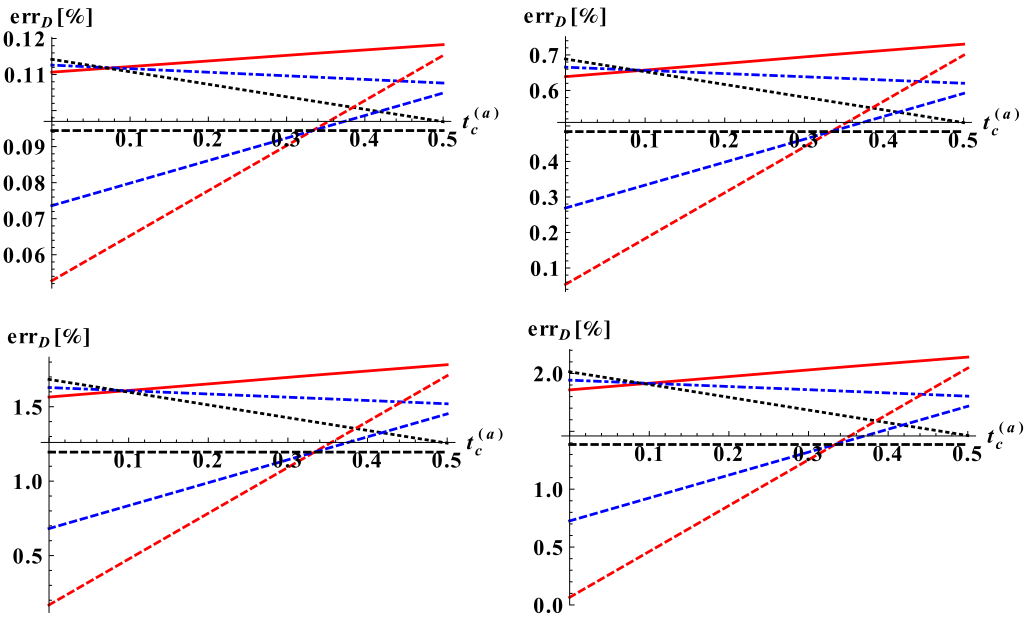

FIG. 23. The four diagrams are similar to Fig. 22 but $\mathrm{err}_D^{(bb,U)}$ is *intentionally* omitted and $\mathrm{err}_D^{(\mathrm{num})} - \mathrm{err}_D^{(bb)}$ is compared with the bulk estimate $\mathrm{err}_D^{(\mathrm{bulk})}$ (the dashed lines of the same color as $\mathrm{err}_D^{(\mathrm{bulk})}$).

a capillary (see Fig. 17), a very small accommodation profile still exists there. This premise could explain the increase of the discrepancy in Fig. 24 with Pe. However, this discrepancy is very small against the boundary-layer dispersion $\mathrm{err}_D^{(bb,U)}$ within the uniform-Λ scheme, as evidenced by the comparison of Figs. 23 and 24.

Figure 25 compares the numerical results for $||\mathrm{err}_D||$, $||\mathrm{err(Sk)}||$, and $||\mathrm{err(Ku)}||$ when $t_c^{(m)} = \frac{1}{3}$. These estimates are the differences of the relative numerical corrections to the bulk predictions obtained with the $t_c^{(a)} = \frac{1}{3}$ and $\frac{1}{2}$. Note that the consideration of the difference for two velocity weights allows us to get rid of the diffusion-layer effects in three transport

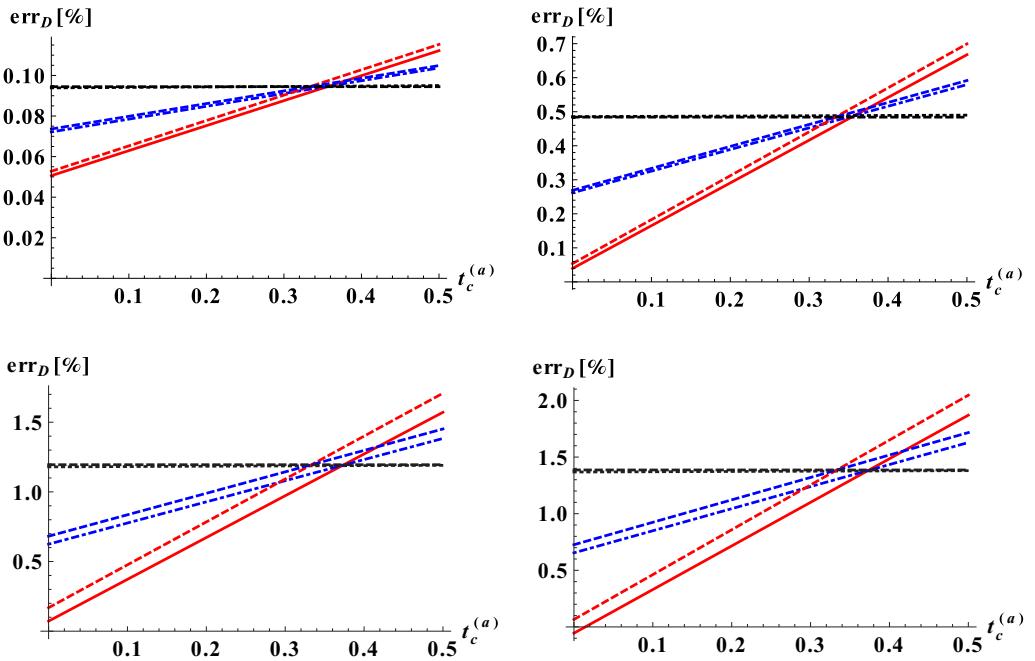

FIG. 24. This figure illustrates the depreciation of the boundary-layer dispersion component $\mathrm{err}_D^{(bb,U)}$ with the double-Λ BB scheme from Table III. The computations are run with $\Lambda_v = \{\frac{1}{12}, \frac{1}{6}, \frac{1}{4}\}$ [dotted line (black), dotted-dashed line (blue), solid line (red)]. Numerical results for $\mathrm{err}_D^{(\mathrm{num})} - \mathrm{err}_D^{(bb)}$ are plotted together with the bulk prediction $\mathrm{err}_D^{(\mathrm{bulk})}$ (dashed lines of the same color). To be compared with Fig. 23 where the uniform-Λ d3Q15 BB scheme is employed.

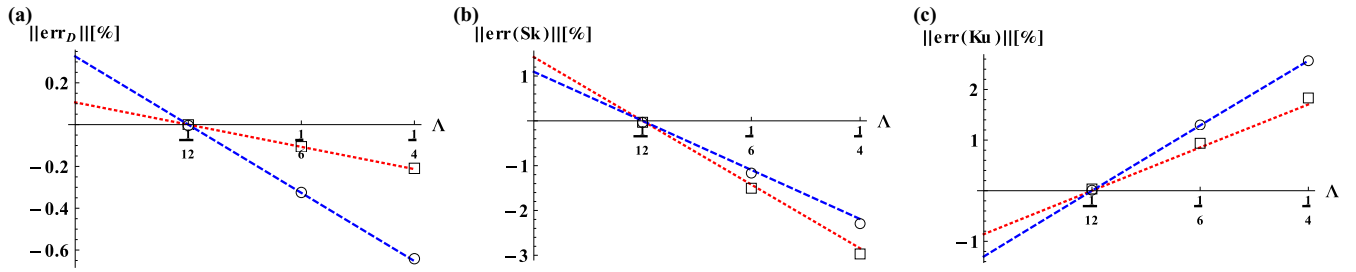

FIG. 25. Cylindrical pipe of $R = 20$, Expt. II [dotted line (red), "squares"] and Expt. IV [dotted-dashed line (blue), "circles"] from Table II. This figure displays the difference in the results obtained with $t_c^{(a)} = \frac{1}{3}$ and $t_c^{(a)} = \frac{1}{2}$ versus bulk value $\Lambda = \Lambda_v$. The numerical data (symbols) and truncation estimate [30] (lines) are displayed together for (a) $||\mathrm{err}_D||$, (b) ||err(Sk)|| and (c) ||err(Ku)||. The double-Λ scheme is applied; it attenuates the boundary-layer advection effects due to $t_c^{(a)} = \frac{1}{3}$ and enables the truncation estimate.

coefficients due to $t_c^{(m)} = \frac{1}{3}$. The double-Λ BB scheme is applied in order to attenuate the boundary-layer velocity and dispersion effects with $t_c^{(a)} = \frac{1}{3}$. The results are displayed together for Pe ≈ 9.5 and Pe ≈ 95.

We observe that, in agreement with the prediction [30], the bulk corrections in three transport coefficients become velocity weight independent when $\Lambda_v = \frac{1}{12}$, where $||\mathrm{err}_D||$, ||err(Sk)||, and ||err(Ku)|| pass through zero in Fig. 25. The three diagrams in Fig. 25 display a very good agreement between the numerical results and bulk predictions [30] in the whole interval $\Lambda \in [\frac{1}{12}, \frac{1}{4}]$. Here, $||\mathrm{err}_D|| = \mathrm{err}_D(t_c^{(a)}) - \mathrm{err}_D(t_c^{(a)} = \frac{1}{2}) = \frac{-3(1-2t_c^{(a)})(\Lambda_v - \frac{1}{12})}{1+k_T^{(c)}} k_T^{(1,c)}$, $k_T^{(1,c)} = \frac{\langle U'(r)U'(r)\rangle}{D_0^2}$ with $U'(r) = U_x(r) - \langle U_x(r)\rangle$, then $k_T^{(1,c)} = \frac{\mathrm{Pe}^2}{12R^2}$ for parabolic profile in a capillary. This functional dependency $||\mathrm{err}_D||$ is expected to be valid for Newtonian or non-Newtonian flow in any-shape open-tabular conduits, and it can be used for validation of the numerical code.

In summary, when the diagonal velocity weight is $t_d^{(a)} \neq 0$, the (analytically constructed) double-Λ scheme from Table III effectively attenuates the boundary-layer effect in velocity, dispersion, and high-order moments. We expect that the boundary-layer behavior with respect to the mass and velocity weights is similar within the grid-aligned conduits of the arbitrary cross section. Our preliminary results show that the deviation of the apparent molecular diffusion coefficient $D^{(\mathrm{num})}$ from its prescribed value D_0 still decays in proportion to the diagonal value $t_d^{(m)}$ for arbitrarily and asymmetrically placed two-dimensional obstructions in a cylindrical tube. Similarly, the deviation of $\mathcal{U}^{(\mathrm{num})}$ from $\mathcal{U}^{(\mathrm{sum})}$ linearly scales there with the $t_d^{(a)}$. Hence, it can be expected that the disparity of the measured moments with the weights can be reduced with the help of the double-Λ BB scheme. We elaborate the iterative algorithm to locate the root $\Lambda_b^{(\mathrm{sol})}(\Lambda_v)$ in Sec. VI B, and examine it in more complicated cases when the tangential constraint is not aligned with the coordinate axis, in the two-dimensional diffusion spreading and advective flow around the circular and rectangular impermeable obstacles, with and without side (bounding) walls.

VI. EFFECTIVE DIFFUSIVITY AND VELOCITY AROUND SOLID OBSTACLES

The purpose of this section is to preliminarily examine (i) whether exists the disparity with the mass and velocity weights in effective diffusion coefficient and apparent velocity, respectively, when the bounce-back rule is applied on the solid obstacles; if so, (ii) whether this dependency remains linear, as in transport through grid-aligned ducts; (iii) whether it reduces or vanishes with the suitable choice of the boundary value $\Lambda_b(\Lambda_v)$, and (iv) how such dependency can be established. The bounce-back simulations with the uniform and double-Λ schemes are examined for (Sec. VI A) the variation of the relative diffusion coefficient with the mass weight in three periodic porous arrangements, and (Sec. VI B) the variation of the effective velocity, dispersion, and skewness with the velocity weight in Stokes flow around a circular obstacle where the numerically constructed $\Lambda_b(\Lambda_v)$ solution will efficiently annihilate velocity-weight dependency in the first moment. The results and the perspectives of these preliminary investigations are summarized.

A. Relative diffusivity

We will consider three classical examples of two-dimensional isotropic periodic arrangements depicted in Fig. 26. Their impermeable solid inclusions are composed from (i) single centered square block, (ii) single centered circle, and (iii) face-centered (staggered) array of squares, respectively. The porosity θ of the periodic cell is set equal to ratio of void cells to entire number of cells. The mean (phase) concentration distribution $\bar{C}(x)$ in Eq. (7) is averaged over the porous part of x cross section. In the pure-diffusion spread around solid obstacles, the effective diffusion coefficient $D = D_{\mathrm{eff}}$ in Eq. (7) is known to become smaller than the molecular diffusion coefficient D_0 [13]; it is estimated with the help of the experimental, semianalytical, and numerical approaches (see review [19]). Using the LBM, the effective diffusivity of the heterogeneous media composed from the overlapping, permeable, and impermeable rectangular inclusions is numerically examined with the help of the d2Q5 BGK scheme in early work [14]. More recently, the D_{eff} was addressed [19,83] with the d2Q5 BGK and d2Q4 MRT schemes, respectively. The impermeable inclusion is commonly modeled [14,19,83] via the bounce-back rule. The relative diffusivity D_r is derived [19,83] with the help of the Fick's law, as a ratio of the apparent mass flux across the media to the prescribed gradient. We will apply the reference data provided by work [19] for $D_r = D_e/D_0$, $D_e = \theta D_{\mathrm{eff}}$.

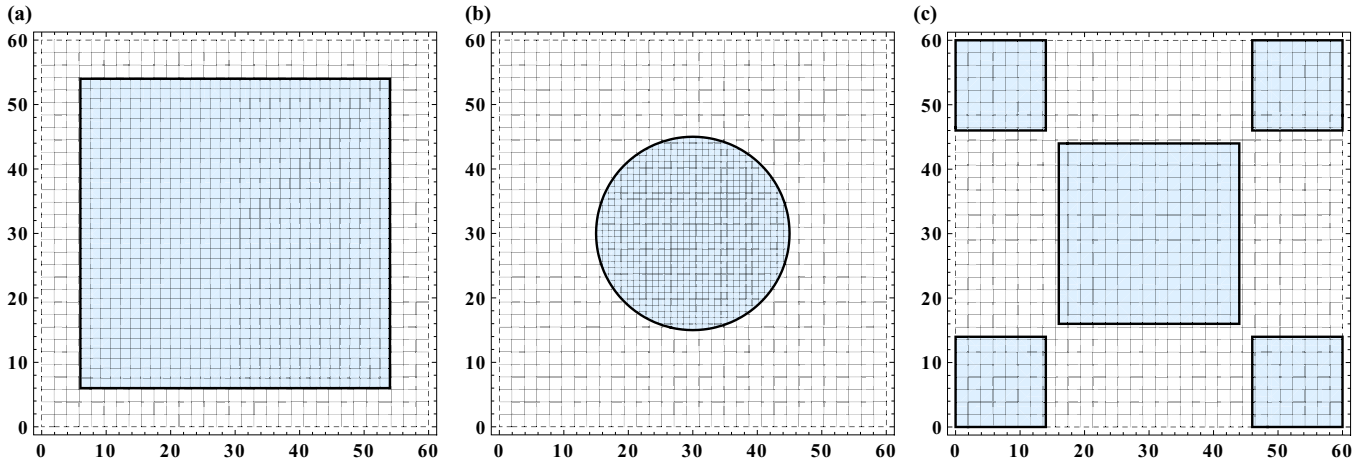

FIG. 26. Three regular arrangements in unit cell $X \times Y = 60^2$ are examined: (a) centered square cylinders of porosity $\theta = 0.36$ (obstacle length is $\frac{4}{5}$ of the cell width); (b) centered circular cylinders of porosity $\theta = 0.8365$ (the diameter halves the cell width); (c) staggered square cylinders of porosity $\theta = 0.56$ (the neighbor corners are distanced by $2\sqrt{2}$ l.u.)

Let us first comment the results [19] in light of the previous discussion. The concentration gradient across the sample is induced [19] with the help of the (anti-bounce-back) Dirichlet ABB rule (10). As has been mentioned (see Remark II in Sec. II B 1), the d2Q4 isotropic diffusion MRT model [19,51] is the particular TRT d2Q5 scheme given by Eqs. (1) and (2) with $c_e = t_c^{(a)} = t_c^{(m)} = \frac{1}{2}$ and $\boldsymbol{U} = 0$, using diffusion rate $s_D = s^-$ and free rate $s_2 = s^+$. The two rates [19] are related as $s_2 = 2 - s_D$ on the base of the ABB solution [51] for parabolic profile. This choice corresponds to the fixed value $\Lambda = \frac{1}{4}$ [cf. Eq. (5)], and it is a particular case of Λ solution (14) for $c_e = \frac{1}{2}$. As has been proved [32] for the TRT model in combination with the ABB and BB rules, the dimensionless steady-state solutions of the scheme are set by physical nondimensional parameters and Λ. It means that the TRT simulations with these two reflections provide D_0-independent coefficient D_r if Λ remains fixed for any D_0. Since $\Lambda = (\frac{1}{s_D} - \frac{1}{2})^2 = (\Lambda^-)^2$ with the BGK operator, it varies together with D_0. This explains the MRT and BGK results [19]. However, the combination $s_2 = 2 - s_D$ [19,51] is not the only suitable choice because D_r is D_0 independent $\forall\, \Lambda > 0$. In principle, $\Lambda = \frac{1}{6}$ [20,30,31] is the most accurate pure-diffusion bulk choice, rather than $\Lambda = \frac{1}{4}$. However, it is possible that the TRT with $\Lambda = \frac{1}{4}$ is in best agreement with the finite-difference coordinate method [13] (FDM) because of the similarity in the bulk discretization and zero-flux condition in these two schemes [cf. Eq. (19)].

We underline that the obtained values D_r depend on Λ. That means that the BGK scheme with $\tau = \frac{1}{2} + \Lambda^-$ produces the same value D_r as the TRT with $\Lambda = (\Lambda^-)^2$, $\forall\, \Lambda^-$; the BGK results coincide with the TRT($\Lambda = \frac{1}{4}$) when $\Lambda^- = \frac{1}{2}$ ($s_D = s_2 = 1$). Indeed, the BGK results are found deficient [19] for large diffusion coefficients because the large values of Λ are inaccurate both in bulk and boundary. In return, the BGK results [19] for dependency D_e/D_0 versus s_D, presented in their Figs. 16 and 22, can serve to examine dependency $D_r(\Lambda)$. This tells us that the similar accuracy as with $\Lambda = \frac{1}{4}$ is reached for $\Lambda \lessapprox 0.7$ ($s_D \approx \frac{3}{4}$ in BGK). In principle, the dependency and resolution performance might be addressed for $D_r(\Lambda)$ similar to permeability measurements, e.g., in regular and random arrays of spheres of the same porosity [34]. The results [34] show that the dependency of the permeability on Λ reduces with the space resolution, but the monotonic behavior towards Λ-independent (common) solution has approximately only first-order rate.

In this study, our concern is not so about $D_r(\Lambda)$ as about D_r variation with the mass-weight stencil $\{t_c^{(m)}, t_d^{(m)}\}$ because of the bounce-back rule. Recall that in the pure-diffusion spread through a straight channel, cylindrical capillary or differently obstructed cylindrical conduits, $D_{\text{eff}} \equiv D_0$ only when $t_c^{(m)} = \frac{1}{2}$, that is, with the d2Q5 and d3Q7 BB schemes. Otherwise, the d2Q9 and d3Q15 BB schemes diminish D_{eff} proportionally to the diagonal mass-weight value $t_d^{(m)}$. The relative error of this deviation, $\text{err}_D^{(bb)}$, is quantified by Eq. (35) exactly in a channel and approximately in a capillary. Further, there is no positive $\Lambda_b(\Lambda_v)$ root in double-Λ scheme where $\text{err}_D^{(bb)} = 0$, but very small boundary values Λ_b may reduce $|\text{err}_D^{(bb)}|$ noticeably.

We perform pure-diffusion simulations ($\boldsymbol{U} = 0$) with the d2Q9 BB scheme. The pulse is initialized with $C(x_0, y, t = 0) = 1$ through open cross section $x = x_0$. Unlike in previous works [14,19,83], the D_{eff} is derived from the second moment with Eq. (8). The simulations are run through a series of the identical porous cells $X \times Y = 60^2$ in three porous arrangements of impermeable inclusions (Fig. 26). The numerical system is periodic in all directions. Such computations are more expensive than those in a single porous cell, but their results are insensitive either to accuracy of the ABB rule or to the effective Fick's flux. In these simulations, $c_e = \frac{1}{3}$ (where the d2Q5 is different from d2Q4) and $\Lambda = \{\frac{1}{6}, \frac{1}{4}\}$; it has been first verified that D_r is Λ^- independent at fixed Λ (we use $\Lambda^- = 1$; its larger values may further accelerate the convergence to steady state).

We first consider a square array depicted in the first diagram in Fig. 26. As suggested, the d2Q5 BB TRT scheme with $\Lambda = \frac{1}{4}$ produces very similar solutions with the FDM scheme [13] in the same cell $X \times Y = 60^2$: e.g., $D_r(\theta = \frac{1}{4}) = 0.575894$ against $D_r = 0.576$ with the FDM [13], and $D_r(\theta = 0.36) = 0.211$ against $D_r(\text{FDM}) = 0.212$. Figure 27 displays

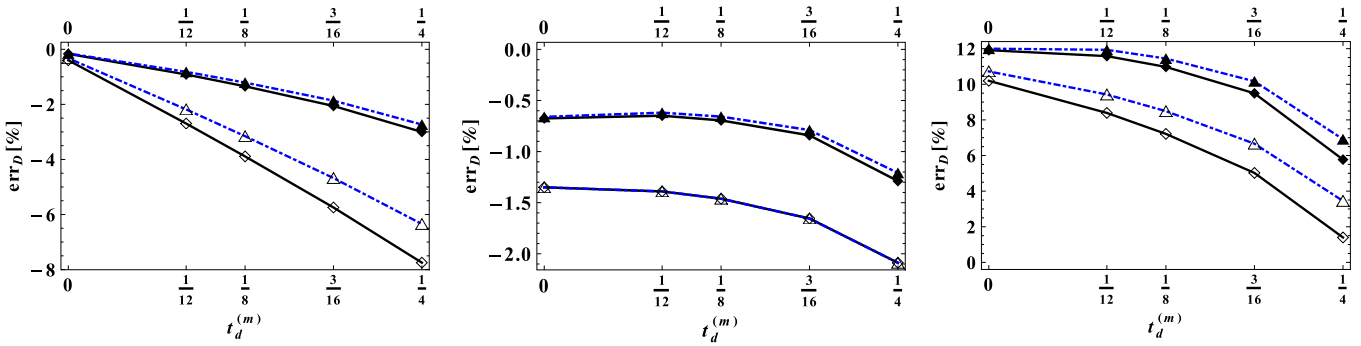

FIG. 27. This figure displays the relative error err_D of the relative dispersivity D_r to its reference value in three regular porous arrangements from Fig. 26. The results are presented versus the diagonal mass weight $t_d^{(m)} \in [0, \frac{1}{4}]$. The computations are performed with the uniform-Λ scheme ("empty symbols") and the double-Λ scheme $\Lambda_b = 10^{-4}$ ("filled symbols"), when $\Lambda_v = \frac{1}{4}$ (black, "squares") and $\Lambda_v = \frac{1}{6}$ (blue, "triangles").

the relative difference err_D with the reference solution [13] for $D_r(\theta = 0.36)$ when the diagonal mass weight $t_d^{(m)}$ varies from 0 (d2Q5) to $\frac{1}{4}$ ("rotated" d2Q5). The four configurations are addressed: two runs with the uniform values $\Lambda = \frac{1}{6}$ and $\frac{1}{4}$, and two runs with the double-Λ scheme, when $\Lambda_v = \{\frac{1}{4}, \frac{1}{6}\}$ and $\Lambda_b = 10^{-4}$ (this choice of small value is arbitrary). The results with the uniform Λ show almost a linear error decrease with the $t_d^{(m)}$. Also, similar to Eq. (35), $|\mathrm{err}_D|$ increases with Λ. The results of the double-Λ scheme are presented in the same (first) diagram in Fig. 26. They show that the two solutions with $\Lambda = \frac{1}{6}$ and $\frac{1}{4}$ approach very closely one another; the dependency $\mathrm{err}_D(t_d^{(m)})$ becomes less linear and the disparity between $t_d^{(m)} = 0$ and $\frac{1}{4}$ reduces by a factor 4 against uniform Λ. On the whole, these results confirm that on the the diagonal stencil the bounce back delays diffusion over rectangular grid-aligned block, similar to axis-aligned wall. The amplitude of this deficiency is controlled by Λ_b: its very small value reduces D_r dependency on the mass weight.

Figure 27 displays in the second diagram the results of the similar simulations in the regular arrangement of circular cylinders depicted in the second diagram in Fig. 26. The reference data [19], based on the Monte Carlo simulation [23], are $D_r = 0.67\theta$ ($\theta = 0.80365$ with our mesh). We first note that the d2Q9 BB produces very similar solutions for $\Lambda = \frac{1}{4}$ and $\frac{1}{6}$ because of the relatively large porosity value. Like in all previous examples, the difference between $t_d^{(m)} = \frac{1}{4}$ and 0 is negative and $|\mathrm{err}_D|$ increases with $t_d^{(m)}$. However, the dependency $\mathrm{err}_D(t_d^{(m)})$ is much more nonlinear than in the square arrangement in the first diagram, although porosity there is much smaller. This result indicates that there is a complex interplay of the tangential boundary-layer directions. So to say, the coordinate and diagonal weights may swap their roles around staircase circle. We also note that the d2Q5 has a larger discrepancy with the reference data than in the previous example of square array because the BB rule does not fit the circular shape exactly either for $\Lambda = \frac{1}{6}$ or $\frac{1}{4}$. In this example, the double-Λ scheme with $\Lambda_b = 10^{-4}$ decreases error amplitude $|\mathrm{err}_D(t_d^{(m)})|$ for all weight values, but this situation is not general because very small Λ is not necessarily accurate for shaped form [34]. On the other hand, the difference between $t_d^{(m)} = \frac{1}{4}$ to 0 is nearly the same, either with the uniform or double-Λ schemes. This confirms that the principal deviation from the reference value in this example is because of the discretization mismatch of the circular shape, rather than because of the boundary-layer tangential effect.

In the third example we consider the staggered array of the nonoverlapping square blocks depicted in the third diagram in Fig. 26. Its percolation limit is $\theta = 0.5$, when corners of neighbor blocks touch each other. Curiously, whereas the d2Q5 BB converges in this limit configuration to expected solution $D_{\mathrm{eff}} \equiv 0$, the system meets difficulties to reach steady state on the full mass-weight stencil, when the diagonal discrete velocities are not bounced back in "common" corners and the solute may travel through the whole system. Figure 27 displays in the third diagram the results for slightly larger porosity $\theta = 0.56$, when the distance between two arrays of the blocks is two nodes. The reference value $D_r \approx 0.26\theta$ is taken from the graph in Fig. 12 [19] (this graph fits the known reference data, but the results [19], computed in a larger cell $X \times Y = 200^2$, overestimate it at small θ). Our results in 60^2 box overestimate it by about 10% when $\Lambda \in [\frac{1}{6}, \frac{1}{4}]$. Further, we observe that the dependency $\mathrm{err}_D(t_d^{(m)})$ becomes much more nonlinear with the uniform Λ against the (more porous) centered-square array in the first diagram in Fig. 27 (where there are 12 nodes distance between two neighbor arrays of rectangles). The double-Λ scheme with $\Lambda_b = 10^{-4}$ noticeably diminishes the difference between the two Λ values and between $t_c^{(m)} = \frac{1}{4}$ and 0 (by factor 2). However, this reduction is twice less than in centered-square array in the first diagram in Fig. 27. In this third example, err_D is positive for all weights, that is, the effective diffusivity is larger than the reference one, and the small value $\Lambda_b = 10^{-4}$ further increases this effect. Similarly, we observe in two rectangular arrays in the first and third diagrams that $\Lambda = \frac{1}{6}$ produces larger effective diffusivity than $\Lambda = \frac{1}{4}$. Similar conclusion might be derived from the BGK results [19], where larger Λ diminish D_r. Such behavior is in line with the usual bounce-back no-slip result in straight channel and porous structures, where small values of Λ usually decrease porous space and diminish permeability [34,35], that is, increase the diffusivity of momentum.

In summary, the computations of the relative diffusivity D_r in three simple porous structures confirm the presence

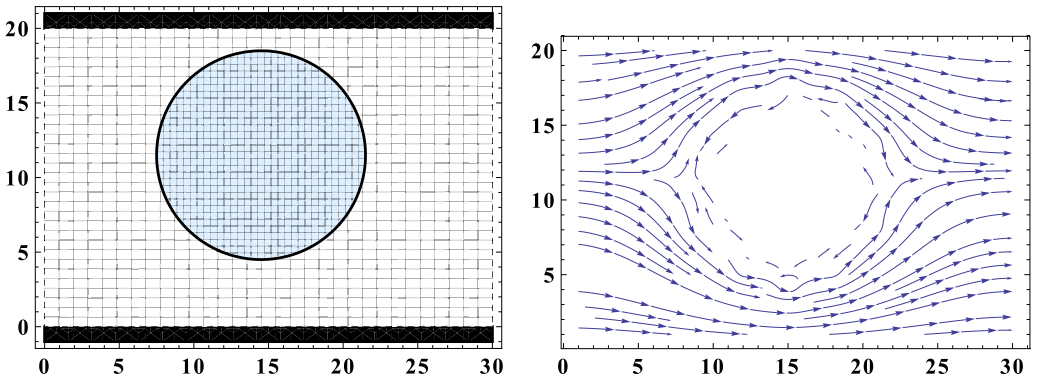

FIG. 28. The diagram in the right illustrates streamlines of the velocity field computed in streamwise-periodic porous cell $[X \times H = 30 \times 20]$ sketched left. The cell is bounded by the horizontal walls; the circular obstacle of $R = 7$ is placed at $(x, y) = (14.5, 11.5)$.

of the retardation BB effect. It is manifested by decrease of D_r from the coordinate stencil $t_c^{(m)} = \frac{1}{2}$ to the diagonal stencil $t_d^{(m)} = \frac{1}{4}$. With the uniform-Λ scheme, the dependency $D_r(t_d^{(m)})$ varies from linear in the centered-square array to (i) less linear in small-porosity staggered square array, and (ii) towards highly nonlinear and smooth in dilute array of circular cylinders. The double-Λ scheme with a sufficiently small value Λ_b is able to reduce the disparity of the results with the mass stencil. However, its efficiency diminishes as the nonlinearity $D_r(t_d^{(m)})$ increases. Based on these preliminary observations, it can be suggested that the largest benefit from the double-Λ distribution in pure diffusion should be expected in open-tubular conduits, in the presence of the external impermeable boundary and rectangular inclusions. In steady-state simulations around shaped obstacles, when exact mass conservation is not so needed, the accurate high-order flux schemes should be called to improve for mass weight and Λ disparity of the results.

B. Advection velocity

We consider the two-dimensional steady-state Stokes flow around a circular obstacle of radius $R = 7$. Its center is asymmetrically placed at $(x, y) = (14.5, 11.5)$ inside a single cell $[X \times Y] = [30 \times 20]$. The system is periodic in x direction and mean flow is along the x axis. The circle is staircase approximated and the discretized system has porosity $\theta = 0.751(6)$. The two configurations are examined: (i) the cell is bounded by two horizontal solid walls, and (ii) the cell is periodic along the y axis. The two systems are sketched in Figs. 28 and 29, together with streamlines of the prescribed velocity field. The velocity field is solved with the TRT BB Stokes-flow scheme [37,49], where we use $\Lambda = \frac{3}{16}$ (the quality of the velocity field and its dependency on Λ is out of scope of this study). The motion is governed by the constant body force directed along the x axis. Let $\boldsymbol{u}(x, y)$ be steady-state macroscopic velocity field. The Darcy-velocity value $\boldsymbol{u}^D(x_i)$ in cross section $x = x_i$ is calculated as section-averaged value; $\boldsymbol{u}^D(x_i)$ is constant through each section of the porous sample thanks to half-force addition to microscopic momentum [35]. Due to linearity of the Stokes equation, the advection-velocity distribution $\boldsymbol{U}(x, y)$ in ADE equilibrium (2) scales $\boldsymbol{u}(x, y)$ with some constant. In our simulations, $U_x^D = 5 \times 10^{-3}$ and it corresponds to mean seepage velocity $\mathcal{U}^{(\mathrm{sum})} = \mathcal{U}^D/\theta = 6.6519 \times 10^{-3}$.

The ADE system is built from a sufficiently large number of the identical cells. The apparent mean velocity $\mathcal{U}^{(\mathrm{num})}$ is extracted from the first raw moment of the (porous-phase) averaged concentration $\bar{C}(x)$. We examine the relative difference $\mathrm{err}_U = \mathcal{U}^{(\mathrm{num})}/\mathcal{U}^{(\mathrm{sum})} - 1$ versus the diagonal velocity-weight value $t_d^{(a)} \in [0, \frac{1}{4}]$; the difference with the coordinate weight $||\mathrm{err}_U(t_d^{(a)})|| = \mathrm{err}_U(t_d^{(a)}) - \mathrm{err}_U(t_d^{(a)} = 0)$ is reported for all simulations. The d2Q9 BB scheme (1) and (2) is applied with $\Lambda^- = \sqrt{\frac{1}{12}}$ (in combination with $\Lambda = \frac{1}{12}$ this scheme suppresses the third-order truncation advection correction [20,31]), and $c_e = \frac{1}{3}$, then $\mathrm{Pe} = \frac{\mathcal{U}L}{c_e\Lambda^-}(L = 20) \approx 1.4$. Recall that Pe, mass weight, or U_α^2 weight family $\{t_q^{(u)}\}$ do

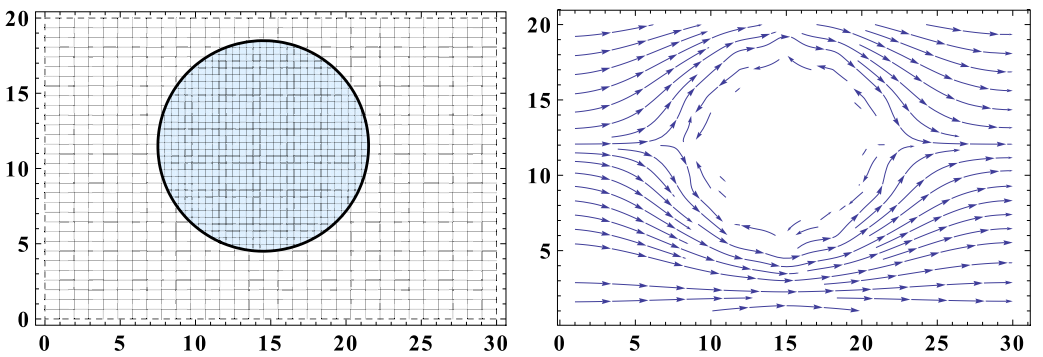

FIG. 29. Similar as in Fig. 28 but the cell is periodic at all ends.

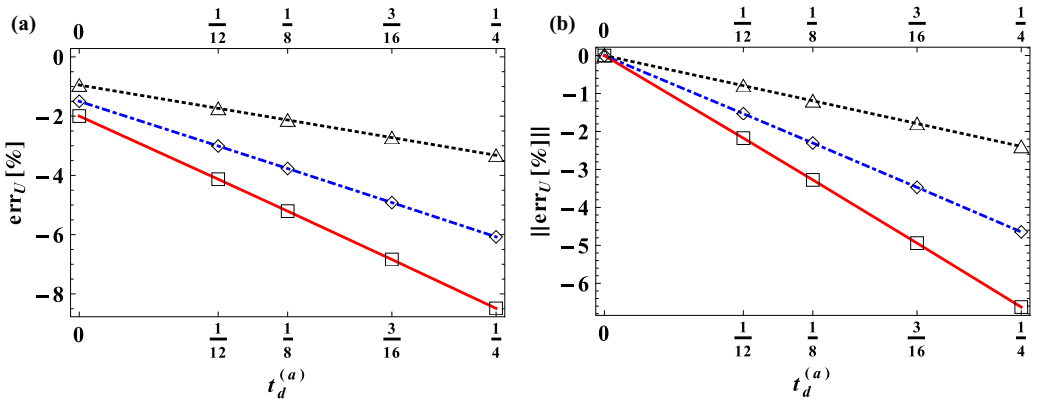

FIG. 30. This figure displays numerical results of the uniform-Λ d2Q9 BB scheme in porous system depicted in Fig. 28, for (a) $\mathrm{err}_U = \mathcal{U}^{(\mathrm{num})}/\mathcal{U} - 1$ and (b) $||\mathrm{err}_U|| = \mathrm{err}_U(t_d^{(a)}) - \mathrm{err}_U(t_d^{(a)} = 0)$. The results are plotted versus the diagonal velocity-weight value $t_d^{(a)} \in [0, \frac{1}{4}]$ when $\Lambda = \{\frac{1}{12}, \frac{1}{6}, \frac{1}{4}\}$ [dotted line (black) triangles, dotted-dashed line (blue) lozenges, solid line (red) squares].

not impact the apparent mean velocity in straight channel and duct flows. Here, we set them on the coordinate stencil for all computations $t_c^{(m)} = t_c^{(u)} = \frac{1}{2}$.

Figure 30 displays numerical results for err_U and $||\mathrm{err}_U||$ which are obtained in bounded configuration displayed in Fig. 28. These simulations are performed with the uniform-Λ distribution $\Lambda = \{\frac{1}{12}, \frac{1}{6}, \frac{1}{4}\}$. The results are displayed versus $t_d^{(a)} = \frac{1}{4} - \frac{1}{2}t_c^{(a)} = \{0, \frac{1}{12}, \frac{1}{8}, \frac{3}{16}, \frac{1}{4}\}$. First, we observe that the d2Q5 scheme $t_d^{(a)} = 0$ results in nonzero (negative) value err_U. Unlike in straight channel and duct flows, $\mathcal{U}^{(\mathrm{num})}$ is different from $\mathcal{U}^{(\mathrm{sum})}$ on the coordinate stencil. Second, $\mathrm{err}_U(t_d^{(a)})$ depends on Λ for all weights, including the d2Q5 scheme. Third, $\mathcal{U}^{(\mathrm{num})}$ diminishes when $t_d^{(a)}$ increases, and this dependency is quasi-linear, in straight channel and duct flows alike. Finally, we observe that the amplitude of the disparity $||\mathrm{err}_U(t_d^{(a)})||$ decreases almost linearly with Λ [recall that in open flow the decrease is $\approx \sqrt{\Lambda}$ in Eq. (51)].

Figure 31 presents results of the similar simulations with the double-Λ scheme. In bulk, Λ_v is fixed to $\frac{1}{6}$. We look for root $\Lambda_b(\Lambda_v)$ where $||\mathrm{err}_U(\Lambda_b, t_d^{(a)})|| \approx 0$. As the initial guess, we apply Poiseuille-flow solution (78): $\Lambda_b^{(1)} = \Lambda_b^{(\mathrm{sol})}(\Lambda_v = \frac{1}{6}, H = 20) = 0.033\,726$. Since $||\mathrm{err}_U(\Lambda_b^{(1)}, t_d^{(a)})||$ is still negative, a small value of $\Lambda_b^{(2)} = 10^{-4}$ is employed at the second iteration; with $||\mathrm{err}_U(\Lambda_b^{(2)})|| > 0$, it brackets the root. The root $\Lambda_b^{(3)}$ solves linear equation $||\mathrm{err}_U(\Lambda_b, t_d^{(m)})|| = 0$ in the interval $\Lambda_b \in [\Lambda_b^{(1)}, \Lambda_b^{(2)}]$. The second diagram in Fig. 31 illustrates that $\Lambda_b^{(3)}$ provides a good enough approximate $||\mathrm{err}_U(\Lambda_b, t_d^{(a)}, \Lambda_v = \frac{1}{6})|| \approx 0$ for all weights $t_d^{(m)} \in [0, \frac{1}{4}]$. In addition, the $\Lambda_b^{(3)}$ reduces the relative disparity between the coordinate and rotated velocity weight in effective dispersion coefficient D in Eq. (7) and the skewness coefficient $\mathrm{Sk}_\star$ in Eq. (9), from -0.7% and -2.4% to 0.028% and 0.88%, accordingly.

Figure 32 displays results of the similar simulations as in Fig. 30 but in fully periodic system depicted in Fig. 29. We observe that, like in the wall-bounded system, the difference $||\mathrm{err}_U(t_d^{(a)})||$ between $t_d^{(a)} = \frac{1}{4}$ and 0 varies quasi-linearly with $t_d^{(a)}$. As could be expected, the d2Q5 has nearly the same value err_U as in the presence of the side walls. However, $||\mathrm{err}_U(t_d^{(a)})||$ has much smaller amplitude than in bounded system, e.g., it reduces by factor 5 for $\Lambda = \{\frac{1}{6}, \frac{1}{4}\}$. Furthermore,

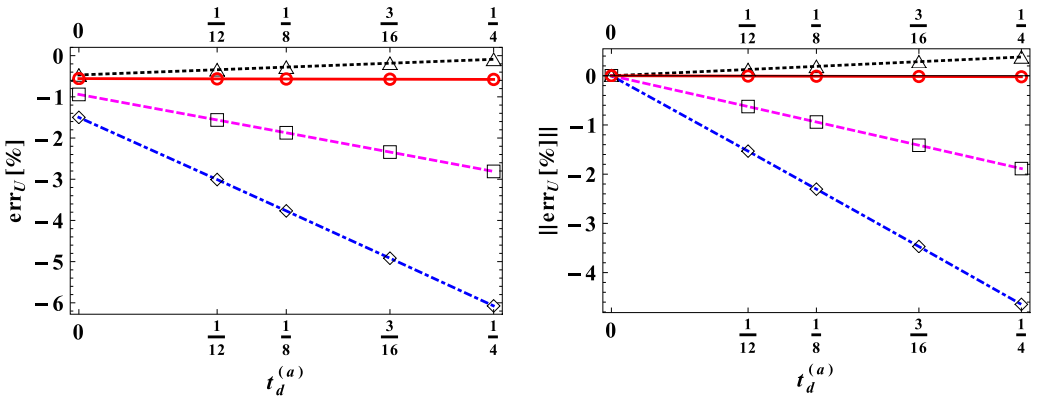

FIG. 31. This figure examines err_U (left) and $||\mathrm{err}_U||$ (right) in simulations with the double-Λ d2Q9 BB scheme in porous system bounded by the two horizontal walls. The bulk value $\Lambda_v = \frac{1}{6}$ is fixed for all results; the uniform-Λ solution is recalled from Fig. 30 [dotted-dashed line (blue) lozenges]. The Λ_b takes three values: $\Lambda_b^{(i)} \approx \{0.033726, 10^{-4}, 0.011(6)\}$, $i = 1,2,3$ [dashed line (magenta) squares, dotted line (black) triangles, solid line (red) circles]; $\Lambda_b^{(3)}$ solves the linear approximate $||\mathrm{err}_U(\Lambda_b)|| = 0$ when $\Lambda_b \in [\Lambda_b^{(2)}, \Lambda_b^{(1)}]$.

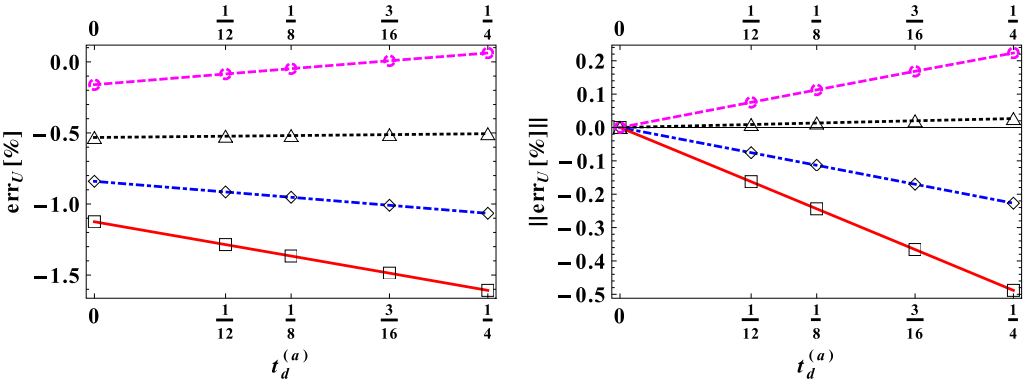

FIG. 32. This figure displays numerical results $\mathrm{err}_U(t_d^{(a)})$ (left) and $||\mathrm{err}_U(t_d^{(a)})||$ (right) for simulations in fully periodic flow depicted in Fig. 29. The results are plotted for uniform distribution $\Lambda = \{10^{-4}, \frac{1}{12}, \frac{1}{6}, \frac{1}{4}\}$ [dashed line (magenta) circles, dotted line (black) triangles, dotted-dashed line (blue) lozenges, solid line (red) squares]. To be compared with the similar simulations in bounded porous channel in Fig. 30.

$\Lambda = \frac{1}{12}$ reverses the previous behavior because $||\mathrm{err}_U(t_d^{(a)})||$ becomes positive. That is, there is a change from retardation to acceleration. To underline this new situation, absent in duct flow solution (51), Fig. 32 is complemented with the results for $\Lambda = 10^{-4}$: they display further linear increase of $\mathcal{U}^{(\mathrm{num})}$ with $t_d^{(a)}$. These results indicate that the most decisive boundary-layer retardation effect is exited by the side wall, while the superposition of the distinguished accommodation effects alter Λ dependency in $||\mathrm{err}_U||$ and may even change the sign of the effect.

Figure 33 applies the double-Λ scheme in combination with the bulk value $\Lambda_v = \frac{1}{4}$ in a fully periodic system. The initial guess interval $[\Lambda_v, \Lambda_b^{(1)}]$ is built from $\Lambda_b = \Lambda_v = \frac{1}{4}$ and Poiseuille-flow solution (71): $\Lambda_b^{(1)} = \Lambda_b^{(\mathrm{sol})}(\Lambda_v = \frac{1}{4}, H = 20) \approx 0.043\,65$. This interval brackets the root $\Lambda_b^{(2)} \approx 0.05$. Figure 33 illustrates that $\Lambda_b^{(2)}$ produces $||\mathrm{err}_U(\Lambda_b^{(2)}, t_d^{(a)})|| \approx 0$ in the whole interval $t_d^{(a)} \in [0, \frac{1}{4}]$.

In summary, the coordinate velocity weight $t_c^{(a)} = \frac{1}{2}$ does not necessarily preserve the prescribed mean seepage velocity $\mathcal{U}^{(\mathrm{sum})}$ in flow around obstacle, but the difference $||\mathrm{err}_U(t_d^{(a)})||$ between the diagonal and coordinate velocity stencil remains quasi-linear. The straight side walls obviously accentuate the retardation effect of the bounce back. In their absence, the sign of this effect can be altered due to more complex accommodation behavior around the shaped obstacle. The double-Λ bounce-back scheme proposes a simple remedy for velocity-weight dependency: the required $\Lambda_b(\Lambda_v)$ root annihilates this dependency in first moment and it can be built with a few bisection iterations in given structure. Consequently, the double-Λ scheme also reduces the velocity-weight disparity in numerical values for dispersion, skewness, and kurtosis. Worthwhile to mention that, unlike in a duct flow, some small dependency over other parameters, such as the velocity amplitude, Λ^- and mass weight, has been detected for $\mathcal{U}^{(\mathrm{num})}/\mathcal{U}^{(\mathrm{sum})}$ in porous structures. Further work is required to quantify this observation. In practice, in given parameter space of the problem, one might look for $\Lambda_b(\Lambda_v)$ where $||\mathrm{err}_U(t_d^{(a)})|| \approx 0$. Moreover, if suitable, one may try to enforce the correct advection velocity locating condition $\mathrm{err}_U(\Lambda_v, \Lambda_b, t_d^{(a)}) \approx 0$ in two-dimensional parameter space $\{\Lambda_v, \Lambda_b\}$, by keeping the bulk value Λ_v in its "optimal" accuracy and stability interval.

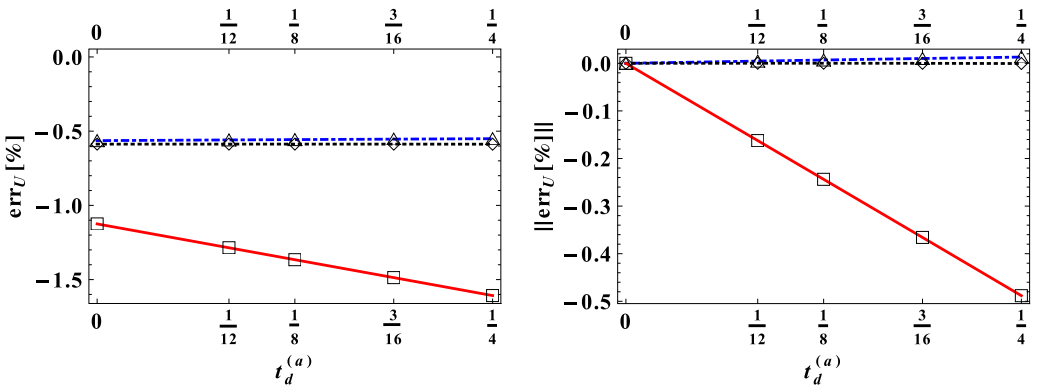

FIG. 33. This figure examines err_U (left) and $||\mathrm{err}_U||$ (right) in simulations with the double-Λ scheme in fully periodic porous system. The bulk value $\Lambda_v = \frac{1}{4}$ is fixed for all results; the uniform-Λ solution is recalled from Fig. 32 [solid line (red), squares]. The Λ_b takes two values: $\Lambda_b^{(1)} \approx 0.04365$ from Eq. (78) [dashed-dotted line (blue), triangles] and $\Lambda_b^{(2)} \approx 0.05$ [dotted line (black), lozenges]; $\Lambda_b^{(2)}$ solves linear approximate $||\mathrm{err}_U(\Lambda_b)|| = 0$ when $\Lambda_b \in [\Lambda_v, \Lambda_b^{(1)}]$.

VII. CONCLUDING REMARKS

This work examines the bounce-back reflection (BB rule) as an impermeability condition for staircase midgrid walls. The principal deficiency of the BB rule in these geometries is the unphysical restriction of the tangential advection-diffusion flux on the solid surface. The focus is put on the quantification of this deficiency for first four moments of the modeled averaged distributions in grid-aligned channel and cylindrical capillary. The analysis and simulations are operated with the d2Q9 and d3Q15 TRT-ADE schemes in full equilibrium and relaxation parameter space. We first discover that the coordinate d3Q7 subclass of the d3Q15 scheme inherits in cylindrical capillary the properties of the d2Q5 scheme in straight channel [69]: it preserves the prescribed arithmetical-mean grid value for streamwise-invariant mean advection velocity (first moment) and isotropic molecular-diffusion coefficient (second moment). Based on the preliminary computations, we suggest that the d3Q7 BB scheme retains these properties in coordinate-aligned ducts of any cross section. This is explained by the fact that in those geometries the bounce-back spurious tangential effect is induced by the diagonal equilibrium weight stencil. We underline that the mass- and velocity-weight families can be prescribed independently. Our interest for their full range is because of (i) the advanced stability of the specific mass- and, especially, velocity-weight stencil [20,21,47]; (ii) the ability for cross entries in diffusion, dispersion, and anti-numerical-diffusion tensors [21,45]; and (iii) the "exchange" between the coordinate and diagonal stencils in rotated geometry. Although there exist the alternative anisotropic approaches, either via the linkwise relaxation rates [22,27] or the extended minimal stencil MRT collision [28,50], all of them operate with disparate Λ combinations, and this property may degrade the bulk stability and accuracy [45]. Although the anisotropic schemes have been analyzed in the presence of impermeable boundaries [22,28,48,65], our work indicates that a further analysis with respect to the distribution moments is required.

We show that in the presence of the diagonal equilibrium weight stencil, the nonequilibrium solution component develops an accommodation correction which links the bulk (Chapman-Enskog) solution to closure relation of the bounce-back rule in duct geometries. The two primary first-order effects of this correction are quantified exactly in a channel and, because of the discretization effect, only approximately in a capillary. The first primary effect is a diminution of the molecular diffusion coefficient proportionally to the diagonal mass weight $t_d^{(m)}$. The relative diffusion-coefficient correction is independent of the velocity field; in motion, it sums with the dispersion in the second moment. Further, the analysis of the diffusion boundary layer is extended to the fourth order; it allows us to quantify and explain the resolution-invariant correction in the kurtosis (fourth moment) observed in the pure-diffusion case. The second primary effect is a diminution of the prescribed mean advection velocity proportionally to the diagonal-velocity weight $t_d^{(a)}$. The relative advection correction is analytically constructed in plug and parabolic profiles; roughly, it scales with the ratio of the boundary velocity value to its mean. The relative advection correction is independent of the velocity amplitude and it is much more significant in a plug flow. The boundary-layer advection correction is easy to observe by the first-moment measurement. Next, we estimate the longitudinal Taylor-type boundary-layer dispersion: it is created by the superposed advective and boundary-layer velocity profiles. The diffusion and advective bounce-back effects make the skewness and kurtosis mass and velocity weight dependent, on top of their truncation weight dependency [30]. In Poiseuille profile, the relative truncation and boundary-layer dispersion effects are nearly Pe independent as Pe increases.

In this work, we propose the double-Λ TRT approach which allows for the independent control over the bulk and boundary effects. We underline that the double-Λ scheme does not solve the bounce-back problem of the midgrid and Λ-dependent location of the arbitrarily shaped solid surface. The purpose of the double-Λ strategy is to remove the primary boundary-layer effects, and thus to reduce their side effects, within rectangular and staircase walls. In that, Λ_v remains freely selectable for the purpose of the advanced accuracy or stability. The specific solution $\Lambda_b^{(\mathrm{sol})}(\Lambda_v)$ given by Eq. (78) preserves prescribed mean velocity in straight Poiseuille flow with the BB rule. We demonstrate that for any velocity weight (but the coordinate mass weight), the double-Λ scheme (78) produces the quasi-identical solutions with the specular reflection for all four moments. A similar but distinct dependency $\Lambda_b^{(\mathrm{sol})}(\Lambda_v)$ is constructed for Poiseuille profile in a capillary, where it (almost) cancels the boundary-layer dispersion and reduces the spurious velocity-weight dependency in skewness and kurtosis. It is also observed that the mean-velocity correction varies linearly with the diagonal-velocity weight in flow around a solid cylinder; this effect is accentuated by the presence of the straight impermeable side walls. Since there is no analytical solution for $\Lambda_b^{(\mathrm{sol})}(\Lambda_v)$ in an arbitrary geometry, we propose an iterative numerical procedure to calculate Λ_b, which vanishes the velocity-weight dependency on the measured first moment. It has been demonstrated that with a suitable (sufficiently small) initial guess, the required root is located in a few bisection iterations. These calculations can be performed once, prior to the main computations in a given geometry. According to the computations, the small valued Λ_b does not significantly impair stability because the velocity near the wall is small.

The advective solution $\Lambda_b^{(\mathrm{sol})}(\Lambda_v)$ does not vanish the diffusion bounce-back effect because of the diagonal mass weight. Indeed, either in a straight channel or cylindrical capillary, there is no positive $\Lambda_b^{(\mathrm{sol})}(\Lambda_v)$ root which exactly preserves the molecular-diffusion coefficient. On the positive side, this diffusion effect decreases either for high Pe or for low Λ_b. Indeed, the noticeable disparity with the mass weight in the effective diffusivity is only observable in the presence of straight bounding walls and grid-aligned rectangular obstacles. Around the curved obstacle, as it was observed in a dilute periodic array of circular cylinders, the boundary layers are oriented differently and their complex interplay makes mass-weight dependency indecisive.

So far, the analysis of the LBM solutions has been principally restricted to relatively smooth nonequilibrium solutions, well described by the Chapman-Enskog or asymptotic expansions. The approach developed in this study to accommodate

the nonequilibrium component goes beyond these limitations. In the presence of discontinuous relaxation rates, or any other discontinuity in the scheme, the two exact generic conditions [22,41,82] relate the equilibrium and nonequilibrium components across the interface intersected by the link. The exactness of the constructed dependency $\Lambda_b^{(\mathrm{sol})}(\Lambda_v)$ in a channel confirms the linkwise recurrence form [32] for the nonequilibrium accommodation layers and the validity of the interface closure condition [41] in their presence. One can suspect that the Knudsen-type nonequilibrium layers arise at any interface or boundary mismatch manifesting itself in the form of resolution-invariant or only first-order convergence rate in simple geometries. For example, this kind of behavior has been very recently observed [52] in the presence of the discontinuous Dirichlet and Neumann conditions on the external, regular, or curved boundary, modeled with the curved Dirichlet boundary rules [48,62] and Neumann boundary rules [62]. The low-order convergence has been also encountered with the bounce-back Poiseuille flow in inclined channels [85] and regular or random arrays of spheres [34], the nonuniform boundary and bulk anisotropic weights [48], the heterogeneous anisotropic mass weight on the grid-aligned interface [22], and the coupling of nonuniformly refined grids [44], due to tangential mismatch in the two last cases. Curiously, the anomalous currents were suppressed with the help of free-rate solution equivalent to $\Lambda = 0$ in early two-phase MRT schemes [40]. Similarly, the oscillations in interface coupling of the discontinuous Darcy profiles reduce in the limit $\Lambda \to 0$ [82,86]. We suggest that the idea of the appropriated nonuniform Λ distribution might find large applicability for its universal control over the leading-order nonequilibrium accommodation.

ACKNOWLEDGMENTS

The author is grateful to G. Silva and A. Vikhansky for critical reading of the manuscript, and thanks ANR for funding the project LaboCothep through Grant No. ANR-12-MONU0011.

APPENDIX: DETAILS FOR BOUNDARY-LAYER ANALYSIS

1. Auxiliary averaged functions

We consider Eqs. (24) and (25). In them, $\langle P(n)\rangle = 0$ and $\langle \mathcal{M}(n)\rangle = 0$ due to the symmetry. We express the averaged values $\langle M(n)\rangle$ and $\langle \mathcal{P}(n)\rangle$. In straight channel, the auxiliary functions $\psi^{(s)}(\Lambda,H)$ and $\Psi^{(s)}(\Lambda,H)$ for $\langle M(n)\rangle$, then $\phi^{(s)}(\Lambda,H)$ and $\Phi^{(s)}(\Lambda,H)$ for $\langle \mathcal{P}(n)\rangle$ are employed [69], with

$$
\begin{aligned}
&M(n) = \frac{k^n + k^{(N-n)}}{k^N - 1}, \mathcal{P}(n) = \frac{k^N - 1}{k^N + 1} M(n), k^N = \frac{2\sqrt{\Lambda} - 1}{2\sqrt{\Lambda} + 1},\ n = 0,1,2,\ldots,N = H - 1\\
&\psi^{(s)}(\Lambda,H) = -\frac{\langle M(n)\rangle H}{2\sqrt{\Lambda} - M(N)} = 1, \langle M(n)\rangle = \frac{\sum_{n=0}^{N=H-1} M(n)}{H} = \frac{1}{H}\left(1 - 2\sqrt{\Lambda} + \frac{2}{k^N - 1}\right),\\
&\phi^{(s)}(\Lambda,H) = \frac{\langle \mathcal{P}(n)\rangle H}{1 - 2\sqrt{\Lambda}\mathcal{M}(N)} = 1, \langle \mathcal{P}(n)\rangle = \frac{\sum_{n=0}^{N=H-1} \mathcal{P}(n)}{H} = \frac{1}{H}\left(1 - 2\sqrt{\Lambda} + \frac{4\sqrt{\Lambda}}{k^N - 1}\right),\\
&\Psi^{(s)}(\Lambda,H) = -\frac{\langle M(n)\rangle H}{1 - 2\sqrt{\Lambda}M(N)} = \left(\frac{2}{1 + k^{N+1}} - 1\right), \Psi^{(s)}(H)|_{\Lambda=\frac{1}{4}} = \Psi^{(s)}(\Lambda)|_{H\to\infty} = 1,\\
&\Phi^{(s)}(\Lambda,H) = \frac{\langle \mathcal{P}(n)\rangle H}{2\sqrt{\Lambda} - \mathcal{M}(N)} = \Psi^{(s)}(\Lambda,H),\ H > 1.
\end{aligned}
\tag{A1}
$$

Similarly, in circular cross section of radius $R > 1$, we express the $\langle M(n)\rangle$ via the auxiliary functions $\psi^{(c)}(\Lambda,R)$ and $\Psi^{(c)}(\Lambda,R)$, while $\langle \mathcal{P}(n)\rangle$ employs $\phi^{(c)}(\Lambda,R)$ and $\Phi^{(c)}(\Lambda,R)$:

$$
\begin{aligned}
&M(n) = \frac{k^n + k^{(N-n)}}{k^N - 1}, \mathcal{P}(n) = \frac{k^N - 1}{k^N + 1} M(n), k^N = \frac{2\sqrt{\Lambda} - 1}{2\sqrt{\Lambda} + 1},\ n = 0,1,2,\ldots,N = 2R - 1\\
&\psi^{(c)}(\Lambda,R) = -\frac{\langle M(n)\rangle l}{2\sqrt{\Lambda} - M(N)}, \psi^{(c)}(R)|_{\Lambda=\frac{1}{4}} = \psi^{(c)}(\Lambda)|_{R\to\infty} = 1,\\
&\langle M(n)\rangle = \frac{2\pi \sum_{n=0}^{N=R-1} M(n) r(n)}{\pi R^2} = \frac{-2k\left(k^{2R-1} + 1\right) + (k-1)(2R-1)(k^{2R} - 1) + 2(k+1)k^R}{(k-1)^2 R^2 \left(k^{2R-1} - 1\right)},\\
&\Psi^{(c)}(\Lambda,R) = -\frac{\langle M(n)\rangle l}{1 - 2\sqrt{\Lambda}M(N)}, \Psi^{(c)}(R)|_{\Lambda=\frac{1}{4}} = \Psi^{(c)}(\Lambda)|_{R\to\infty} = 1, \text{ with } l = \frac{2R^2}{2R - 1}
\end{aligned}
\tag{A2}
$$

and, respectively,

$$\Phi^{(c)}(\Lambda,R)=\frac{\langle\mathcal{P}(n)\rangle l}{2\sqrt{\Lambda}-\mathcal{M}(N)}=\Psi^{(c)}(\Lambda,R),\ \langle\mathcal{P}(n)\rangle=\frac{(k^{2R-1}-1)}{(k^{2R-1}+1)}\langle M(n)\rangle,$$
$$\phi^{(c)}(\Lambda,R)=\frac{\langle\mathcal{P}(n)\rangle l}{1-2\sqrt{\Lambda}\mathcal{M}(N)},\ \phi^{(c)}(R)|_{\Lambda=\frac{1}{4}}=\phi^{(c)}(\Lambda)|_{R\to\infty}=1,\ \text{with } l=\frac{2R^2}{2R-1}. \tag{A3}$$

2. Fourth-order-accurate concentration profile

The bounce back creates y-dependent correction $C'(x,y,t)$ to averaged concentration $\bar{C}(x,t)$ in pure-diffusion simulations in straight channel. It follows that the apparent fourth-order-accurate equation (39) originates from the averaging of the two-dimensional pure-diffusion equation (6) in the form

$$\langle T(x,t)\rangle=c_e\Lambda^-\left(\left\langle\bar{\Delta}_x^2C\right\rangle+\left\langle\bar{\Delta}_y^2C\right\rangle+2t_d^{(m)}\left\langle\bar{\Delta}_x^2\bar{\Delta}_y^2C'\right\rangle\right)-\left(\Lambda-\frac{1}{4}\right)\left\langle\sum_{q=1}^{Q_m}\bar{\Delta}_q^2g_q^+\right\rangle, \tag{A4}$$

where, with making use of the apparent second-order equation (32),

$$\langle T(x,t)\rangle=\partial_t\bar{C}+\Lambda^-\bar{\Delta}_t^2\bar{C},\ \Lambda^-\bar{\Delta}_t^2\bar{C}=\Lambda^-\partial_t[\partial_t\bar{C}]=\Lambda^-[\Lambda^-c_e(1+\delta_m)]^2\partial_x^4\bar{C}, \tag{A5}$$

$$\left\langle\bar{\Delta}_x^2C\right\rangle=\partial_x^2\bar{C}+\tfrac{1}{12}\partial_x^4\bar{C}+O(\epsilon^6),\left\langle\bar{\Delta}_y^2C\right\rangle=\left\langle\partial_y^2C'\right\rangle+\tfrac{1}{12}\left\langle\partial_y^4C'\right\rangle+O(\epsilon^6), \tag{A6}$$

$$\left\langle\bar{\Delta}_x^2\bar{\Delta}_y^2C'\right\rangle=\partial_x^2\left\langle\partial_y^2C'\right\rangle+O(\epsilon^6). \tag{A7}$$

In particular, the first component $-\Lambda^{-3}c_e^2(1+\delta_m)^2$ in A_3^{bb} from Eq. (44) is due to Eq. (A5). The second component $\frac{1}{12}c_e\Lambda^-(1+\delta_m)$ is due to the first relation in Eq. (A6). The profile $C'(x,y,t)$, $y\in[-H/2,H/2]$, is looked in the fourth-order polynomial form specified by Eqs. (40) and (41):

$$C'(x,y,t)=a_0(x,t)y^4+a_2(x,t)y^2+a_3(x,t),\ \text{with } a_2(x,t)=\tfrac{1}{2}\left[s\partial_x^2\bar{C}(x,t)+\tfrac{1}{12}(s+p)\partial_x^4\bar{C}(x,t)\right]. \tag{A8}$$

Although the parabolic approximate $C'(x,y,t)=\frac{1}{2}s\partial_x^2\bar{C}(x,t)y^2+a_3(x,t)$ was sufficient to derive kurtosis in Sec. III B when $\Lambda=\frac{1}{4}$, let us provide fourth-order polynomial solution in Eq. (A8). It reads as

$$\Lambda=\frac{1}{4}:\ s=\delta_m,\ p=\frac{\delta_m^2}{2}(H^2+6H+3),\ a_0=\frac{\delta_m^2}{24}\partial_x^4\bar{C},\ \text{with } \delta_m=-\frac{4t_d^{(m)}}{H}. \tag{A9}$$

The remaining coefficient $a_3(x,t)$ is set with normalization condition $\langle C'(x,y,t)\rangle=0$. Employing the arithmetical averaging, this solution yields Eqs. (A6)–(A7) with

$$\begin{aligned}\left\langle\partial_y^2C'\right\rangle&=2a_2+a_0H^2-a_0=\delta_m\partial_x^2\bar{C}(x,t)+\tfrac{1}{12}\left(\delta_m+p+\tfrac{1}{2}{\delta_m}^2H^2-\tfrac{1}{2}\delta_m^2\right)\partial_x^4\bar{C}(x,t)\\&=\delta_m\partial_x^2\bar{C}(x,t)+\tfrac{1}{12}[\delta_m+\delta_m^2(H^2+3H+1)]\partial_x^4\bar{C}(x,t),\left\langle\partial_y^4C'\right\rangle=\delta_m^2\partial_x^4\bar{C}(x,t),\\\left\langle\bar{\Delta}_y^2C'\right\rangle&=\left\langle\partial_y^2C'\right\rangle+\tfrac{1}{12}\left\langle\partial_y^4C'\right\rangle=\delta_m\partial_x^2\bar{C}(x,t)+\tfrac{1}{12}(H^2+3H+2)\delta_m^2\partial_x^4\bar{C}(x,t),\\2t_d^{(m)}\left\langle\bar{\Delta}_x^2\bar{\Delta}_y^2C\right\rangle&=2t_d^{(m)}\delta_m\partial_x^4\bar{C}(x,t)=-\tfrac{1}{12}\times\left(6H\delta_m^2\right)\partial_x^4\bar{C}(x,t).\end{aligned} \tag{A10}$$

By substituting the two last relations into Eq. (A4) for $\Lambda=\frac{1}{4}$, it takes the form of Eq. (39) with Eq. (44). When $\Lambda=\frac{1}{4}$, we confirm all these relations quasi-exactly with the help of the fourth-order polynomial fit of the numerical profiles $C'(y)$ at fixed x and t. This example illustrates that the high-order finite-difference analysis can be exactly developed for $\Lambda=\frac{1}{4}$.

[1] H. W. Stockman, R. J. Glass, C. Cooper, and H. Rajaram, Accuracy and computational efficiency in 3D dispersion via lattice-Boltzmann: Models for dispersion in rough fractures and double-diffusive fingering, Int. J. Mod. Phys. C **09**, 1545 (1998).

[2] Q. Kang, D. Zhang, S. Chen, and X. He, Lattice Boltzmann simulation of chemical dissolution in porous media, Phys. Rev. E **65**, 036318 (2002).

[3] V. Pot, H. Hammou, N. Elyeznasmi, and I. Ginzburg, Role of soil heterogeneities onto pesticide fate: a pore-scale study with Lattice Boltzmann, in *Proceedings of the 1st International Conference and Exploratory Workshop on Soil Architecture and Physicochemical Functions "Cesar"* (Reseach Centre Foulum, Tjele, 2010).

[4] H. Hammou, I. Ginzburg, and M. Boulerhcha, Two-relaxation-times Lattice Boltzmann schemes for solute transport in unsaturated water flow, with a focus on stability, Adv. Water Resour. **34**, 779 (2011).

[5] C. Hubert, B. Schafei, and A. Parmegiani, A new pore-scale model for linear and non-linear heterogeneous dissolution and precipitation, Geochim. Cosmochim. Acta **124**, 109 (2014).

[6] L. Chen, Q. Kang, B. A. Robinson, Y.-I. He, and W.-Q. Tao, Pore-scale modeling of multiphase reactive transport with phase transitions and dissolution-precipitation process in closed systems, Phys. Rev. E **87**, 043306 (2013).

[7] J. Yang, J. Crawshaw, and E. S. Boek, Quantitative determination of molecular propagator distributions for solute transport in homogeneous and heterogeneous porous media using lattice Boltzmann simulations, Water Resour. Res. **49**, 8531 (2013).

[8] A. Genty and V. Pot, Numerical calculation of effective diffusion in unsaturated porous media by the TRT lattice Boltzmann method, Transp. Porous Media **105**, 391 (2014).

[9] M. K. Misztal, A. Hernandez-Garcia, R. Matin, D. Müter, D. Jha, H. O. Sørensen, and J. Mathiesen, Simulating anomalous dispersion in porous media using the unstructured lattice Boltzmann method, Front. Phys. **3**, 50 (2015).

[10] L. E. Vogel, D. Makowski, P. Garnier, L. Vieublé-Gonod, Y. Coquet, X. Raynaud, N. Nunan, C. Chenu, R. Falconer, and V. Pot, Modeling the effect of soil meso- and macropores topology on the biodegradation of a soluble carbon substrate, Adv. Water Resour. **83**, 123 (2015).

[11] M. C. Sukop and K. J. Cunningham, Lattice Boltzmann methods applied to large-scale three-dimensional virtual cores constructed from digital optical borehole images of the karst carbonate Biscayne aquifer in southeastern Florida, Water Resour. Res. **50**, 8807 (2014).

[12] X. Zhang, J. W. Crawford, R. J. Flavel, and I. M. Young, A multi-scale Lattice Boltzmann model for simulating solute transport in 3D x-ray-tomography images of aggregated porous materials, J. Hydrol. **541**, 1020 (2016).

[13] Jin-Hwan Kim, J. Alberto Oschoa, and S. Whitaker, Diffusion in anisotropic porous media, Transp. Porous Media **2**, 327 (1987).

[14] J. Alvarez-Ramírez, S. Nieves-Mendoza, and J. González-Trejo, Calculation of the effective diffusivity of heterogeneous media using the lattice-Boltzmann method, Phys. Rev. E **53**, 2298 (1996).

[15] A. Calì, S. Succi, A. Cancelliere, R. Benzi, and M. Gramignani, Diffusion and hydrodynamic dispersion with the lattice Boltzmann method, Phys. Rev. A **45**, 5771 (1992).

[16] S. Ponce-Dawson, S. Chen, and G. D. Dooleen, Lattice Boltzmann computations for reaction-diffusion equation, J. Chem. Phys. **98**, 1514 (1993).

[17] R. M. H. Merks, A. G. Hoekstra, and P. M. A. Slot, The moment propagation method for advection-diffusion in the lattice Boltzmann method: Validation and Péclet number limits, J. Comput. Phys. **183**, 563 (2002).

[18] D. Wolf-Gladrow, *Lattice-Gas Cellular Automata and Lattice Boltzmann Models: An Introduction* (Springer, Berlin, 2000).

[19] Z. Chai, C. Huang, B. Shi, and Z. Guo, A comparative study on the lattice Boltzmann models for predicting effective diffusivity of porous media, Int. J. Heat Mass Transfer **98**, 687 (2016).

[20] I. Ginzburg, Truncation errors, exact and heuristic stability analysis of two-relaxation-times lattice Boltzmann schemes for anisotropic advection-diffusion equation, Commun. Comput. Phys. **11**, 1439 (2012).

[21] I. Ginzburg, D. d'Humières, and A. Kuzmin, Optimal stability of advection-diffusion Lattice Boltzmann models with two relaxation times for positive/negative equilibrium, J. Stat. Phys. **139**, 1090 (2010).

[22] I. Ginzburg and D. d'Humières, Lattice Boltzmann and analytical modeling of flow processes in anisotropic and heterogeneous stratified aquifers, Adv. Water Resour. **30**, 2202 (2007).

[23] S. Trinh, P. Arce, and B. R. Locke, Effective diffusivities of point-like molecules in isotropic porous media by Monte Carlo simulation, Transp. Porous Media **38**, 241 (2000).

[24] G. I. Taylor, Dispersion of soluble matter in solvent flowing slowly through a tube, Proc. R. Soc. London, Ser. A **219**, 186 (1953).

[25] R. Aris, On the dispersion of a solute in a fluid flowing through a tube, Proc. R. Soc. London **235**, 67 (1956).

[26] H. Brenner, Dispersion resulting from flow through spatially periodic porous media, Philos. Trans. R. Soc., A **297**, 81 (1980).

[27] I. Ginzburg, Equilibrium-type and link-type lattice Boltzmann models for generic advection and anisotropic-dispersion equation, Adv. Water Resour. **28**, 1171 (2005).

[28] H. Yoshida and M. Nagaoka, Multiple-relaxation-time lattice Boltzmann model for the convection and anisotropic diffusion equation, J. Comput. Phys. **229**, 7774 (2010).

[29] A. Vikhansky and I. Ginzburg, Taylor dispersion in heterogeneous porous media: Extended method of moments, theory, and modeling with two-relaxation-times lattice Boltzmann scheme, Phys. Fluids **26**, 022104 (2014).

[30] I. Ginzburg, Prediction of the moments in advection-diffusion lattice Boltzmann method. I. Truncation dispersion, skewness, and kurtosis, Phys. Rev. E **95**, 013304 (2017).

[31] I. Ginzburg and L. Roux, Truncation effect on Taylor-Aris dispersion in lattice Boltzmann schemes: Accuracy towards stability, J. Comput. Phys. **299**, 974 (2015).

[32] D. d'Humières and I. Ginzburg, Viscosity independent numerical errors for lattice Boltzmann models: From recurrence equations to "magic" collision numbers, Comput. Math. Appl. **58**, 823 (2009).

[33] I. Ginzburg, Consistent lattice Boltzmann schemes for the Brinkman model of porous flow and infinite Chapman-Enskog expansion, Phys. Rev. E **77**, 066704 (2008).

[34] S. Khirevich, I. Ginzburg, and U. Tallarek, Coarse- and fine-grid numerical behavior of MRT/TRT lattice-Boltzmann schemes in regular and random sphere packings, J. Comput. Phys. **281**, 708 (2014).

[35] I. Ginzburg and D. d'Humières, Multi-reflection boundary conditions for lattice Boltzmann models, Phys. Rev. E **68**, 066614 (2003).

[36] C. Pan, L.-S. Luo, and C. T. Miller, An evaluation of lattice Boltzmann schemes for porous media simulation, Comput. Fluids **35**, 898 (2006).

[37] L. Talon, D. Bauer, N. Gland, S. Youssef, H. Auradou, and I. Ginzburg, Assessment of the two relaxation time lattice-Boltzmann scheme to simulate Stokes flow in porous media, Water Resour. Res. **48**, W04526 (2012).

[38] S. Bogner, S. Mohanty, and U. Rüde, Drag correlation for dilute and moderately dense fluid-particle systems using the lattice Boltzmann method, Int. J. Multiphase Flow **68**, 71 (2015).

[39] C. Demuth, S. Mishra, M. A. Mendes, S. Ray, and D. Trimis, Application and accuracy issues of lattice Boltzmann method for solving elliptic PDEs commonly encountered in heat transfer and fluid flow problems, Int. J. Thermal Sci. **100**, 185 (2016).

[40] I. Ginzbourg and P. M. Adler, Surface tension models with different viscosities, Transp. Porous Media **20**, 37 (1995).

[41] I. Ginzburg, Lattice Boltzmann modeling with discontinuous collision components: Hydrodynamic and advection-diffusion equations, J. Stat. Phys. **126**, 157 (2007).
[42] X. Meng and Z. Guo, Multiple-relaxation-time lattice Boltzmann model for incompressible miscible flow with large viscosity ratio and high Péclet number, Phys. Rev. E **92**, 043305 (2015).
[43] L. Talon and D. Bauer, On the determination of a generalized Darcy equation for yield stress fluid in porous media using a lattice Boltzmann TRT scheme, Eur. Phys. J. E: Soft Matter Biol. Phys. **36**, 139 (2013).
[44] I. Ginzburg, Variably saturated flow described with the anisotropic lattice Boltzmann methods, J. Comput. Fluids **35**, 831 (2006).
[45] I. Ginzburg, Multiple anisotropic collisions for advection-diffusion lattice Boltzmann schemes, Adv. Water Resour. **51**, 381 (2013).
[46] I. Ginzburg, Comment on "An improved gray lattice Boltzmann model for simulating fluid flow in multi-scale porous media": Intrinsic links between LBE Brinkman schemes, Adv. Water Resour. **88**, 241 (2016).
[47] A. Kuzmin, I. Ginzburg, and A. A. Mohamad, A role of the kinetic parameter on the stability of two-relaxation-times advection-diffusion lattice Boltzmann scheme, Comput. Math. Appl. **61**, 3417 (2011).
[48] I. Ginzburg, Generic boundary conditions for lattice Boltzmann models and their application to advection and anisotropic-dispersion equations, Adv. Water Resour. **28**, 1196 (2005).
[49] I. Ginzburg, F. Verhaeghe, and D. d'Humières, Two-relaxation-time lattice Boltzmann scheme: About parametrization, velocity, pressure and mixed boundary conditions, Commun. Comput. Phys. **3**(2), 427 (2008).
[50] I. Rasin, S. Saucci, and W. Miller, A multi-relaxation lattice kinetic method for passive scalar diffusion, J. Comput. Phys. **206**, 453 (2005).
[51] S. Cui, N. Hong, B. Shi, and Z. Chai, Discrete effect on the halfway bounce-back boundary condition of multiple-relaxation-time lattice Boltzmann model for convection-diffusion equations, Phys. Rev. E **93**, 043311 (2016).
[52] L. Li, N. AuYeung, R. Mei, and J. F. Klausner, Effects of tangential-type boundary condition discontinuities on the accuracy of the lattice Boltzmann method for heat and mass transfer, Phys. Rev. E **94**, 023307 (2016).
[53] I. Ginzburg, F. Verhaeghe, and D. d'Humières, Study of simple hydrodynamic solutions with the two-relaxation-times lattice Boltzmann scheme, Commun. Comput. Phys. **3**(3), 519 (2008).
[54] S. Bogner, R. Ammer, and U. Rüde, Boundary conditions for free interfaces with the lattice Boltzmann method, J. Comput. Phys. **297**, 1 (2015).
[55] Rupert W. Nash, Hywel B. Carver, Miguel O. Bernabeu, James Hetherington, Derek Groen, Timm Krüger, and Peter V. Coveney, Choice of boundary condition for lattice-Boltzmann simulation of moderate-Reynolds-number flow in complex domains, Phys. Rev. E **89**, 023303 (2014).
[56] M. Bouzidi, M. Firdaouss, and P. Lallemand, Momentum transfer of a Boltzmann-lattice fluid with boundaries, Phys. Fluids **13**, 3452 (2001).
[57] I. Ginzbourg and P. M. Adler, Boundary flow condition analysis for the three-dimensional lattice Boltzmann model, J. Phys. II (France) **4**, 191 (1994).
[58] T. Zhang, B. Shi, Z. Guo, Z. Chai, and J. Lu, General bounce-back scheme for concentration boundary condition in the lattice-Boltzmann method, Phys. Rev. E **85**, 016701 (2012).
[59] C.-H. Liu, K.-H. Lin, H.-C. Mai, and C.-A. Lin, Thermal boundary conditions for thermal lattice Boltzmann simulations, Comput. Math. Appl. **59**, 2178 (2010).
[60] Q. Chen, X. Zhang, and J. Zhang, Improved treatments for general boundary conditions in the lattice Boltzmann method for convection-diffusion and heat transfer processes, Phys. Rev. E **88**, 033304 (2013).
[61] J. Huang, Z. Hu, and W.-A. Yong, Second-order curved boundary treatments of the lattice Boltzmann method for convection-diffusion equations, J. Comput. Phys. **310**, 26 (2016).
[62] L. Li, R. Mei, and J. F. Klausner, Boundary conditions for thermal lattice Boltzmann equation method, J. Comput. Phys. **237**, 366 (2013).
[63] T. Gebäck and A. Heintz, A lattice Boltzmann method for the advection-diffusion equation with Neumann boundary conditions, Commun. Comput. Phys. **15**, 487 (2013).
[64] G. Drazer and J. Koplik, Tracer dispersion in two dimensional rough fractures, Phys. Rev. E **63**, 056104 (2001).
[65] X. Zhang, J. W. Crawford, A. G. Bengough, and I. M. Young, On boundary conditions in the lattice Boltzmann model for advection and anisotropic dispersion equation, Adv. Water Resour. **25**, 601 (2002).
[66] M. Markl and C. Körner, Free surface Neumann boundary condition for the advection-diffusion lattice Boltzmann method, J. Comput. Phys. **301**, 230 (2015).
[67] E. Attar and C. Körner, Lattice Boltzmann model for thermal free surface flows with liquid-solid phase transition, Int. J. Heat Fluid Flow **32**, 156 (2011).
[68] J. Huang and W.-A. Yong, Boundary conditions of the lattice Boltzmann method for convection-diffusion equations, J. Comput. Phys. **300**, 70 (2015).
[69] I. Ginzburg, L. Roux, and G. Silva, Local boundary reflections in lattice Boltzmann schemes: Spurious boundary layers and their impact on the velocity, diffusion and dispersion, C. R. Mec. **343**, 518 (2015).
[70] C. Cercignani, *The Boltzmann Equation and Its Applications* (Springer, Berlin, 1988), pp. 252–260.
[71] R. Cornubert, D. d'Humières, and D. Levermore, A Knudsen layer theory, Physica D (Amsterdam) **47**, 241 (1991).
[72] D. R. Noble, Lattice Boltzmann study of the interstitial hydrodynamics and dispersion in steady state inertial flows in large randomly packed beds, Ph.D. thesis, University of Illinois Urbana-Champaign, 1996.
[73] R. G. M. Van der Sman and M. H. Ernst, Convection-diffusion lattice Boltzmann scheme for irregular lattices, J. Comput. Phys. **160**, 766 (2000).
[74] R. G. M. Van der Sman, Galilean invariant lattice Boltzmann scheme for natural convection on square and rectangular lattices, Phys. Rev. E **74**, 026705 (2006).
[75] P. Lallemand and L.-Shi Luo, Theory of the lattice Boltzmann method: Acoustic and thermal properties in two and three dimensions, Phys. Rev. E **68**, 036706 (2003).
[76] D. J. Holdych, D. R. Noble, J. G. Georgiadis, and R. O. Buckius, Truncation error analysis of lattice Boltzmann methods, J. Comput. Phys. **193**, 595 (2004).
[77] D. David, F. Kuznik, K. Johannes, and L. Merlier, Numerical analysis of truncation error, consistency, and axis boundary

condition for axis-symmetric flow simulations via the radius weighted lattice Boltzmann model, Comput. Fluids **116**, 46 (2015).

[78] F. Dubois, Equivalent partial differential equations of a lattice Boltzmann scheme, Comput. Math. Appl. **55**, 1441 (2008).

[79] T. Inamuro, A lattice kinetic scheme for incompressible viscous flows with heat transfer, Philos. Trans. R. Soc., A **360**, 470 (2002).

[80] G. Batôt, L. Talon, Y. Peysson, M. Fleury, and D. Bauer, Analytical and numerical investigation of the advective and dispersive transport in Herschel-Bulkley fluids by means of a lattice-Boltzmann two-relaxation-time scheme, Chem. Eng. Sci. **141**, 271 (2016).

[81] R. Huang and H. Wu, A modified multiple-relaxation-time lattice Boltzmann model for convection-diffusion equation, J. Comput. Phys. **274**, 50 (2014).

[82] I. Ginzburg, G. Silva, and L. Talon, Analysis and improvement of Brinkman lattice Boltzmann schemes: Bulk, boundary, interface. Similarity and distinctness with finite-elements in heterogeneous porous media, Phys. Rev. E **91**, 023307 (2015).

[83] N. Jeong, D. Choi, and C. Lin, Estimation of thermal and mass diffusivity in a porous medium of complex structure using a lattice Boltzmann method, Int. J. Heat Mass Transfer **51**, 3913 (2008).

[84] X. He, Q. Zou, L.-S. Luo, and M. Dembo, Analytic solutions and analysis on non-slip boundary condition for the lattice Boltzmann BGK model, J. Stat. Phys. **87**, 115 (1997).

[85] I. Ginzbourg and D. d'Humières, Local second-order boundary method for lattice Boltzmann models, J. Stat. Phys. **84**, 927 (1996).

[86] G. Silva and I. Ginzburg, The permeability and quality of velocity field in a square array of solid and permeable cylindrical obstacles with the TRT-LBM and FEM Brinkman-schemes, C. R. Mec. **343**, 545 (2015).